COMPUTATIONALLY MODELING THE AEROELASTIC PHYSICS OF FLAPPING-WING FLIGHT

by

Ryan Keith Schwab

A dissertation submitted in partial fulfillment
of the requirements for the degree

of

Doctor of Philosophy

in

Engineering

MONTANA STATE UNIVERSITY
Bozeman, Montana

May 2023

DEDICATION

I would like to dedicate this dissertation to all of my family and friends, whose support was instrumental in its completion, and to my Uncle Jim, whose guidance and encouragement toward graduate research ignited my own passion for scientific knowledge and inquiry. To my two best university friends, Lincoln and Jaclyn, I offer my enduring gratitude. It has been my great fortune to share adventures, both in academics and in the mountains, with you both.

TABLE OF CONTENTS

TABLE OF CONTENTS – CONTINUED

TABLE OF CONTENTS – CONTINUED

LIST OF TABLES

LIST OF FIGURES

LIST OF FIGURES – CONTINUED

Figure Page

LIST OF FIGURES – CONTINUED

LIST OF FIGURES – CONTINUED

LIST OF FIGURES – CONTINUED

Figure Page

LIST OF FIGURES – CONTINUED

Figure Page

LIST OF FIGURES – CONTINUED

Figure Page

ABSTRACT

Flying insects use flapping wings to achieve flight at minuscule sizes. These flapping wings deform elastically under both inertial and aerodynamic loading. While conventional aircraft are often designed to reduce flexibility in their wings, insects harness the benefits of wing flexibility through elastic potential energy storage and enhancement of flapping wing-specific aerodynamic phenomena. Aircraft at insect size scales could have an inexhaustible number of uses ranging from monitoring of congested piping networks in oil refineries, to extraterrestrial land surveyance in thin atmospheres. If these micro air vehicles are to be realized, however, they will need to harness the aerodynamic benefits of flapping wings in order to overcome unfavorable ratios of lift to drag forces and inefficiencies of DC motors at such small sizes.

Study of flapping wing aeroelastics is complicated due to the large-amplitude rotations of the wings, unsteady dynamics of the fluid regime, and small size and weight scales of the wings. While some experimental work focuses on techniques like measuring kinematics through motion tracking with high-speed videography, and partial flow field measurements through particle image velocimetry, it is difficult to conduct experiments that paint a full picture of the fluid-structure interaction of these wings. Instead, this research focuses on high-fidelity computational modeling through bilaterally coupled computational fluid dynamics and finite element analysis software to understand the fluid-structure interaction of flapping wings. In this work, a reduced order modeling technique capable of calculating the bulk aeroelastic physics of flapping wings at computational efficiencies suitable for parameter optimization studies was also validated. Finally, the influence of tapered wing thickness on aeroelastics and energetic efficiency was studied. While wing tapering reduced mean thrust, it had a greater reduction on the energetic requirement to produce flapping kinematics and was therefore more energetically efficient.

1

INTRODUCTION

Flying insects evoke a particular interest in the engineering and biological communities due to their ability to perform complex flight tasks with very simple neural systems [Huston and Jayaraman, 2011]. Insects are able to fly up to 35 mph, rapidly change flight direction, fly sideways, and hover which is the most energetically expensive form of flight [Norberg, 1996; Hu et al., 2009]. Some insects like the dragonfly are even able to intercept flying prey mid-flight [Hu et al., 2009]. This flight ability is even more impressive when considering their neural system is simple enough that such flight behavior can be directly controlled through implanted neural stimulation [Sato et al., 2009].

To achieve these impressive flying abilities, insects utilize an array of sensory organs and mechanoreceptors to adjust wing flapping kinematics, angular position of their bodies, and orientation of their gaze among other benefits. Blowflies for example process visual information into a velocity field which is directly applied to a gaze stabilization system, keeping the flies head and gaze on heading regardless of wind gusts or other influences to flight path and body orientation [Huston and Krapp, 2008; Hengstenberg, 1991]. Many two-winged insects utilize halteres, small club-like sensory organs believed to have evolved from hindwings of ancestral insects [Yarger and Fox, 2016], to sense and automatically react to their body's angular velocity [Dickerson et al., 2021]. Other insects like the hawkmoth *Manduca sexta* have an array of campaniform sensilla, small strain sensing mechanoreceptors, located across the surface of their wings in order to adjust their flapping kinematics and body orientation for improved flight control based on wing deformation [Aiello et al., 2021; Pratt et al., 2017; Dickerson et al., 2014]. The hawkmoth's use of wing strain information is a sure indicator that wing deformation is an important aspect of flapping flight.

Wing deformation in flapping flight is influenced by both inertial and aerodynamic loads [Wootton, 1981; Nakata and Liu, 2012b; Combes and Daniel, 2003b]. These deformations affect the fluid flow over the wing, which in turn affects the deformations, resulting in strong bilateral coupling between the fluid and structure domain. This fluid structure interaction (FSI) is an important aspect of insect flight as the interplay of wing flexibility and aerodynamics often improves both aerodynamic and energetic efficiency. The storage of elastic potential energy in a deformed wing is recycled in insect flight to reduce the overall energetic requirement to maintain flight [Reid et al., 2019]. This allows for insects to drive larger flapping amplitudes at higher frequencies much more efficiently. Additionally, wing flexibility allows for passive pitching of the wing which lowers induced drag and has been shows to strengthen the leading edge vortex (LEV) which is a major contributor in lift production for flapping wings [Heathcote et al., 2008; Lee et al., 2018]. In clap-and-fling flapping kinematics, wing flexibility has been shown to reduce drag force by as much as 50% and increases lift when compared to rigid wing cases [Miller and Peskin, 2009].

Insects harness lift producing aerodynamic phenomena that are unique to flapping wings. An area of strong vorticity forms just above the leading edge of the wing during flapping flight. This leading edge vortex (LEV) is a dominant producer of lift for flapping winged insects, and can form on many wings with a sharp leading edge and is often induced when the angle of attack is high or is rapidly changing [Videler et al., 2004]. Because the LEV is often formed in instances of high angle of attack or rapid changes in angle of attack, it commonly produces stall-like behavior, known as shedding or "bursting", from the wing surface producing a dynamic stall [Mai et al., 2008]. This LEV burst can result in increased aerodynamic forces temporarily, but will shortly after result in a sharp drop in lift producing force as the wing remains in stall. Flapping winged insects however, benefit from the LEV by achieving stroke reversal prior to bursting and the LEV reforms on the other side of the wing (now the new "top" surface).

Wing flexibility has a significant impact on the strength and shedding of the LEV, and as a result impacts the average lift produced by the wing. In a computational study by Nakata and Liu [Nakata and Liu, 2012a], the effect of wing flexibility on the LEV was studied by comparing a modeled hawkmoth wing to a rigid wing of equivalent geometry and kinematics. They found that the addition of flexibility allowed the LEV to remain attached to the wing (and thereby produce lift) for a longer portion of the flapping cycle, and that the LEV was stronger and covered a slightly larger area of the wing.

Additionally, at stroke reversal the wing pitches to reorient for rotation back in the opposite direction. This pitching is often timed slightly before maximum stroke angle, resulting in a Magnus effect that induces lift during stroke reversal [Dickinson et al., 1999]. Some insects allow their wings to collide or nearly collide at stroke maxima, known as clap-and-fling flapping [Lighthill, 1973]. This wing clapping creates large wakes that assist in lift production on stroke reversal, a process known as wake capture.

These flapping wing aerodynamics allow insects to fly at sizes that would be impossible with conventional aircraft designs. At these sizes, Reynolds numbers ($R_e = \frac{\rho V L}{\mu}$, the ratio of inertial to viscous forces) are very low. In order to compensate for this imbalance of forces, a conventional propeller would have to spin at much higher speeds. The combination of high rotation speeds and small sizes creates a new problem however, in that DC motors, which are often used to drive propellers in small to medium sized aircraft, would be unable to dissipate heat efficiently and would not be sustainable for flight. It is clear then that use of flapping wing aerodynamics holds more promise for the realization of aircraft at centimeter and millimeter size scales.

Micro Air Vehicles (MAVs) are becoming an increasingly popular concept as they have a wide array of possible applications. MAVs can be used to monitor congested areas such as mapping a cave system or leak detection around piping networks in a refinery. Additionally, the ongoing instability in native bee populations [VanEngelsdorp and Meixner, 2010] has

motivated the idea of using MAVs as artificial pollinators. Current MAVs like quadcopters have reached fairly small sizes nearly tenable for these applications, but the low R_e issue becomes a major problem at the millimeter and centimeter size scale. Instead, flapping wing micro air vehicles (FWMAVs) hold promise for sustained flight with small sizes and low R_e. FWMAVs therefore hold the potential to be significantly smaller than their propeller-based counterparts. This would benefit their application as pollinators navigating through agricultural fields, as early forest fire detectors flying low below the treetops, and in other areas where small size and low mass would be of particular benefit.

Low-mass aircraft that can operate at low R_e also have an interesting application in extraterrestrial land surveyance. On planets like Mars with extremely thin atmospheres, the low air density lowers the R_e of aircraft that would otherwise be able to achieve flight on Earth. FWMAVs would have an advantage here both in harnessing flapping wing aerodynamic phenomena, and in their inherent lightweight nature making them easier to carry in extraplanetary travel. If such aircraft are to be realized however, a deeper understanding of flapping wing FSI will be needed in order to produce efficient, lift-generating wings.

Through the use of piezoelectric, electromagnetic, electrostatic, and dielectric elastomer actuators, large advances in FWMAV technology have been achieved over the past decade [Xiao et al., 2021]. These actuators have made possible orders of magnitude reduction in size from FWMAVs like the Nano Hummingbird, with a 16.5 cm wingspan and 19 g mass [Keennon et al., 2012], to the RoboBee X-Wing with an impressive 3.5 cm wingspan and mass of 0.259 g [Breuer, 2019]. Such technological advances show the potential for extremely small-scale robotic flight, however, sustained flight times in these cases are limited by available energy storage systems and fatigue life cycles of actuators. To improve the lifespan of these small flyers, greater power efficiency is needed and can be achieved through the development of more energetically efficient wings.

Study of flapping wings through physical experimentation can be limited due to the nature of large and fast flapping kinematics. Driving the multiple rotational degrees of freedom at speeds comparable to insect wing kinematics is an extremely challenging problem, and isolating the wing's reaction forces from the inertial forces produced by experimental setup adds significant complexity to the problem.

Computational simulation of these flapping kinematics is possible though, and computational modeling of both fluid flows and structural deformations are well-established practices [Schwab et al., 2019; Wang et al., 2016]. Computational expense of these high fidelity modeling techniques has already driven the production of some simplified models to better understand the physics behind flapping winged flight. While simplified models come with assumptions of what forces might be insignificant and negligible, they hold potential to capture some of the relevant physics extremely quickly, making them useful in parametric studies [Roccia et al., 2017; Fitzgerald et al., 2011; Sane and Dickinson, 2002; Whitney and Wood, 2010; Jankauski et al., 2017].

The research presented in this dissertation uses both high fidelity and reduced order modeling techniques to study the aeroelastic physics governing flapping wings. This study is aimed to inform further development of FWMAVs by focusing on optimizing the aerodynamics and energetic requirements of the wings. This research shows practical use of reduced order modeling to narrow the scope of a parameter space used in FWMAV wing design. With this narrowed parameter space in mind, high fidelity modeling can be used to further pinpoint optimal parameters for wing design and to show the aeroelastic benefits gained from such parameter selection. The remainder of this dissertation is organized as follows:

1. *Detailed Methods.* Significant details about the high fidelity model used to study flapping wings are supplied. This model uses bilaterally coupled computational fluid dynamics in Star-CCM+ and finite element analysis in Abaqus. This section is intended

to assist in the future use of this high fidelity modeling technique.

2. *Devolopment of a reduced order aerodynamic model.* A reduced order model base on blade element theory (BET) is introduced with multiple degree of freedom (MDOF) flapping kinematics. The wing is geometrically similar to the wing of a hawkmoth but treated as rigid. Normal force on the wing is compared to normal force as calculated from a Reynolds-averaged Navier–Stokes computational fluid dynamics (RANS CFD) solver.

3. *Fluid structure interaction and experimental validation.* The BET based reduced order model is two-way coupled with a structural solver based on modal truncation to produce a deformable blade element theory (DBET) model. The DBET model is validated for single degree of freedom (SDOF) flapping in and out of vacuum based on strain measurements gathered from flapping a paper, rectangular wing.

4. *High fidelity fluid structure interaction and experimental validation.* The RANS CFD solver is two-way coupled with a finite element analysis (FEA) structural solver. This high fidelity model and the DBET model are validated for SDOF flapping experimentally by tracking wingtip displacement of a paper, rectangular wing, flapping under high speed videography motion tracking.

5. *HiFi, DBET, and unsteady vortex lattice method with parameter study.* Another coupled reduced order model based on 2D unsteady vortex lattice method (UVLM) and modal truncation is introduced. The model is used in a "quasi-3D" scheme, where the three-dimensional wing is modeled as "stacked" 2D UVLM models. This UVLM model, as well as the DBET and high fidelity models, are used to study their efficacy for MDOF flapping of a rectangular wing, assuming the high fidelity model's results as an accurate source to validate against. The two reduced order models are then used

in a parameter sweep study to compare their computational expense and efficacy for parameter optimization studies, and to validate across a broad range of 2 structural parameters.

6. *Effect of wing tapering on flapping wing energetic efficiency* To study the influence of heterogeneous stiffness on aeroelastic efficiency, several cases of tapered wing thickness (which is proportional to stiffness cubed) were modeled using the high fidelity solver. Outcomes from the modeled wings revealed that while some lift producing force was lost when the wings were tapered, required power to drive the flapping kinematics was more significantly reduced. This gain in energetic efficiency warrants the use of wing tapering under the correct flapping kinematics and wing size for larger payload capacity of a flapping wing micro air vehicle.

8

METHODS

In this chapter, the particular setup and approach for the high-fidelity model is discussed. First, an explanation of the Finite Element Analysis (FEA) structural solver is presented. This includes details the of elements types used, mesh convergence decisions, and rotating boundary conditions and constraints applied to produce bio-similar flapping kinematics. Next, the Computational Fluid Dynamics (CFD) model used for the fluid solver is explained. Here, considerations of RANS closure methods, a rotating Chimera mesh and RBF morpher, and meshing and time-step convergence decisions are presented. Finally, the two-way coupled time-marching scheme is explained along with a workflow outlining how both fluid and inertial forces are conserved.

Structural Model

Finite Element Analysis is a widely used resource for modeling solid structures. This modeling technique discretizes a solid into multiple elements and resolves structural force responses on the corners or "nodes" of these elements (see Figure 2.1). Three-dimensional FEA models are often discretized using three-dimensional tetrahedral or hexahedral elements, where each element has discretized nodes in all three spatial dimensions. One limitation of this discretization type is that these elements must hold an aspect ratio near one [Logan, 2007], which can be a problem for very thin walls like the geometry that makes up an insect wing. The rectangular wing that was used in the model associated with Figures 2.2 and 2.3 has a thickness that was more than 4 orders of magnitude smaller than its span length or chord length [Schwab et al., 2020]. For a converged FEA mesh, at least 5 tetrahedral elements were needed through the wing's thickness to calculate an accurate response to an applied load, and this resulted in a requirement of several million elements to keep the aspect ratio of the elements roughly cube shaped. This many elements created

an untenable computational expense even before coupling to a fluids solver.

Instead of three-dimensional elements, this model uses shell type elements. Shell elements allow the wing to be discretized across its chord and span, but the prescribed thickness does not need to be rendered and is instead assumed to have linear stiffness and insignificant compressive or tensile deformation. This reduced the total required element count to the hundreds at maximum which is significantly more computationally manageable. This discretization method allows for each element to be encompassed by significantly fewer nodes where deformations are calculated, adding to the overall computational efficiency of the model. One potential limitation of this element type however lies in the two-way coupling where the wing must also be modeled without a thickness in the fluid model. This means that the fluid solver is unable to model complicated wing surface topography or the aerodynamic effects of wing thickness in this two-way coupled scheme. The extremity of computational expense justifies this decision, however it does slightly limit the scope of possible parameters to study.

In chapter 7, thickness tapering of the wing is introduced. While this tapering is not reflected in the fluid solver because of the planar nature of the shell elements used, the distribution is included in the structural solver. In FEA, this distribution is applied in the section assignment step by defining the shell thickness as a nodal distribution which follows the analytical function to define the thickness of nodes at their spatial coordinate.

The FEA model and mesh were validated experimentally for a rectangular paper wing through the use of our PolyTec Scanning Vibrometer. The wing's natural frequencies are a good metric to use when considering the wing's structural properties as they relate the geometry, mass, and stiffness across different mode shapes (bending, twisting, etc.). By clamping the wing at its root and using the vibrometer to measure the significant natural frequencies occurring as an impulse response, experimental data was collected to validate against. In FEA, encastre (i.e. walled) boundary conditions were applied to the

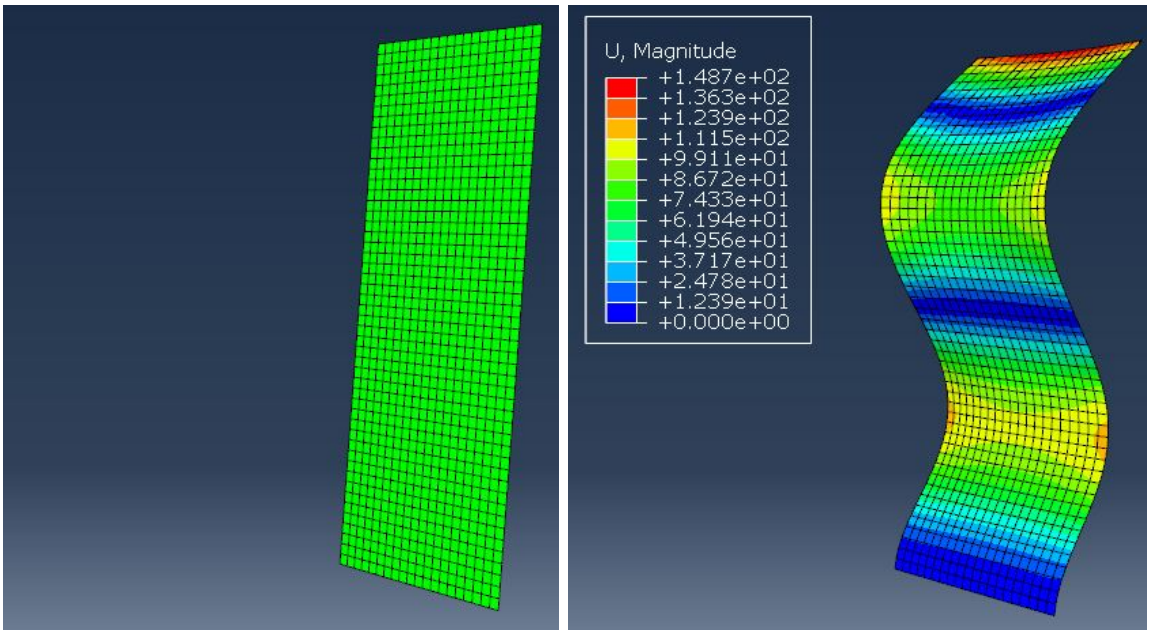

Figure 2.1: FEA meshing of a homogeneous, rectangular wing in the undeformed state (left) and a dramatized deformed state (right). The mesh is seen in black lines across the green wing (undeformed), where each element is roughly square, and surrounded by 4 nodes, denoted as the intersection of the mesh lines.

wing's root to act as the clamp used in the vibrometer experiment. A frequency-type linear perturbation step with mass-normalized eigenvectors was used under these boundary conditions to calculate the first four natural frequencies of the modeled wing. The mesh refinement was deemed acceptable when agreement was found between the modeled wing's natural frequencies and those gathered in the vibrometer experiment.

Fluid Model

Computational Fluid Dynamics is a method of studying fluid dynamics by modeling the Navier-Stokes equations [Anderson, 1995]. To reduce the necessary computational resources, the Reynolds Averaged Navier-Stokes (RANS) equations are considered. These equations

include conservation of mass:

$$\frac{\partial \langle u_i \rangle}{\partial x_i} = 0$$

where $\langle u_i \rangle$ is the mean fluid velocity, conservation of momentum:

$$\rho_f \frac{\partial \langle u_i \rangle}{\partial t} + \rho_f \frac{\partial}{\partial x_i} \left(\langle u_i \rangle \langle u_j \rangle \right) = -\frac{\partial P}{\partial x_i} + \mu \nabla^2 \langle u_i \rangle - \frac{\partial \tau_{ij}}{\partial x_j}$$

where ρ_f is the fluid velocity, P is pressure, μ is dynamic viscosity, and τ_{ij} is the Reynolds stress tensor defined as:

$$\tau_{ij} = \rho_f \langle u_i' u_j' \rangle$$

Here, u_i' is the perturbed part of the fluid velocity contributing to the effect of turbulence on the mean flow. The perturbed velocity components of the Reynolds stress tensor do not allow these equations to be solved analytically, so computational resources must be used to resolve these equations across a discretized domain. In order to resolve small scale turbulence phenomena, this discretization would have to be impractically fine, therefore additional equations known as closure models are needed to resolve average velocities in elements on a coarser discretization [Durbin, 2017]. The Spallart-Allmaras (SA) model was used for this study because, as a one-equation model, it offers acceptable computational efficiency and its efficacy in flapping wing aerodynamics is already established [Schwab et al., 2019; Fairuz et al., 2013].

CFD resolves these equations by discretizing the fluid domain into volume elements, and calculating relative pressures and velocities between these elements. Many CFD studies involve a single discretization (or "mesh") of the fluid domain, however moving boundaries like a flapping wing complicate the meshing process because increased discretization around the moving boundary being studied is often needed, and the mesh must somehow follow that boundary's movement. Additionally, FSI complicates the mesh even further due to the

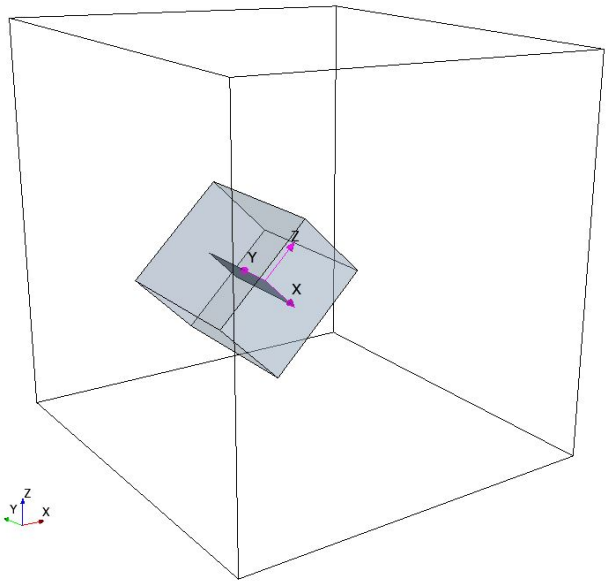

Figure 2.2: *CFD Meshing Regions.* Background mesh (outlined) and Chimera mesh (grey) regions of the fluid domain in Star-CCM+. The rectangular wing is seen in dark grey within the Chimera mesh. The background mesh must be large enough to accommodate the flapping kinematics, while the Chimera mesh must accommodate the out-of-plane deformation of the wing.

deformations acting as additional movement of the boundary that is not prescribed by the researcher. To accommodate these problems, a Chimera meshing approach is used which adds a second localized mesh to be resolved inside of the static, larger mesh of the entire fluid domain (see Figure 2.2). This localized mesh, known as a Chimera mesh, can move with a prescribed motion to follow the prescribed flapping kinematics of the flapping wing. At each modeled time step, this Chimera mesh region is cut out of the domain mesh and fluid values at the interface are interpolated to maintain conservation of mass and momentum.

To accommodate for the wing's deformation — which can be thought of as an unprescribed, moving boundary condition within the Chimera mesh -– the Chimera mesh uses a radial basis function (RBF) morpher, which allows the quadrilateral shape of this region and elements within it to bend and stretch to follow the deformation of the wing (see Figure 2.3).

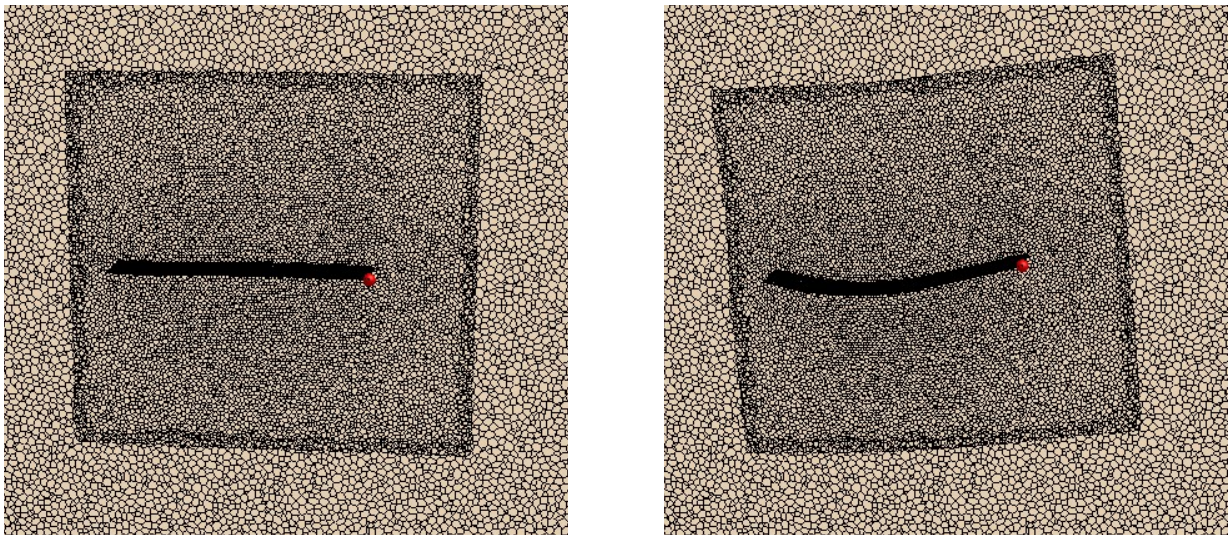

Figure 2.3: Cross-sectional images of the mesh at the initial condition (left) and at a deformed state (right). Notice the deformed Chimera mesh (shown generally rectangular with finer mesh discretization) is curved slightly as it follows the deformation of the wing (thick black line with red marker at the tip).

In addition to the geometric considerations of the fluid mesh regions, the elements themselves must be considered. An automated polyhedral meshing algorithm was used along with user defined prism layer meshing near the wing surface. Meshing parameters like element volume average, element growth factor, number of prism layers, and prism layer thickness were determined via a meshing convergence test as well as ensuring an agreement of element size between the Chimera and background meshes. While this test was performed solely on the CFD, choosing a slightly finer discretization than necessary was assumed to accommodate the additional motion of wing deformation, maintaining the model's accuracy.

A similar convergence test was used to validate the chosen timestep. The maximum timestep in CFD would not take into account the additional motion of deformation, however with relatively small deformations compared to the rigid body kinematics, this influence was assumed minimal. At each timestep, the accuracy of the modeled flow field increases with increased iterations of resolving the Navier Stokes equations, so an additional convergence

test was performed to choose the number of iterations necessary per timestep.

Two-Way Coupling

Some multi-physics software resolves models for fluids, structures, thermodynamics, electromagnetism and more, and while this type of software facilitates a wide range of problems, it often lacks the efficiency and advanced modeling techniques found in specifically designed CFD software and FEA software [Fairuz et al., 2013]. Here, two rigorous modeling software are used – Abaqus/CAE 2019 (v12.41.51) from Dassault Systemes, and Star-CCM+ (v2020.2.1) from Siemens. They are coupled through the SIMULIA Co-simulation Engine (CSE) package from from Dassault Systemes which harnesses a shared interface between the two models upon which to pass information at every timestep.

Centrifugal, Euler, and Coriolis forces play a vital role in flapping wing deformation [Jankauski and Shen, 2014], and it is therefore vital that the wing's prescribed motion (or rigid body motion) be driven through FEA to capture these inertial based forces. The general two-way coupled workflow then is lead from Abaqus FEA, in which the time-step starts by applying rotational velocities to the wing and resulting inertial forces are calculated for each node in the FEA mesh. Abaqus then estimates the deformation caused by these forces on each node, applies the deformation to the meshed wing. These deformations, associate with the defined surface of the wing, are sent as updated node locations to Star-CCM+.

Star-CCM+ is then responsible for calculating the effect that the wing movement has on the fluid flow field domain. The Chimera mesh is shifted based on the prescribed rigid body motion of the wing, and then the new node locations from Abaqus are used to apply the wing deformation and accordingly skew the Chimera mesh via the RBF morpher. In this way, both the velocities from rigid body motion and from wing deformation are imposed on the wing. Star-CCM+ can then assume the change in location of the wing has resulted from a constant velocity over the time-step, and treats the surrounding fluid as though being

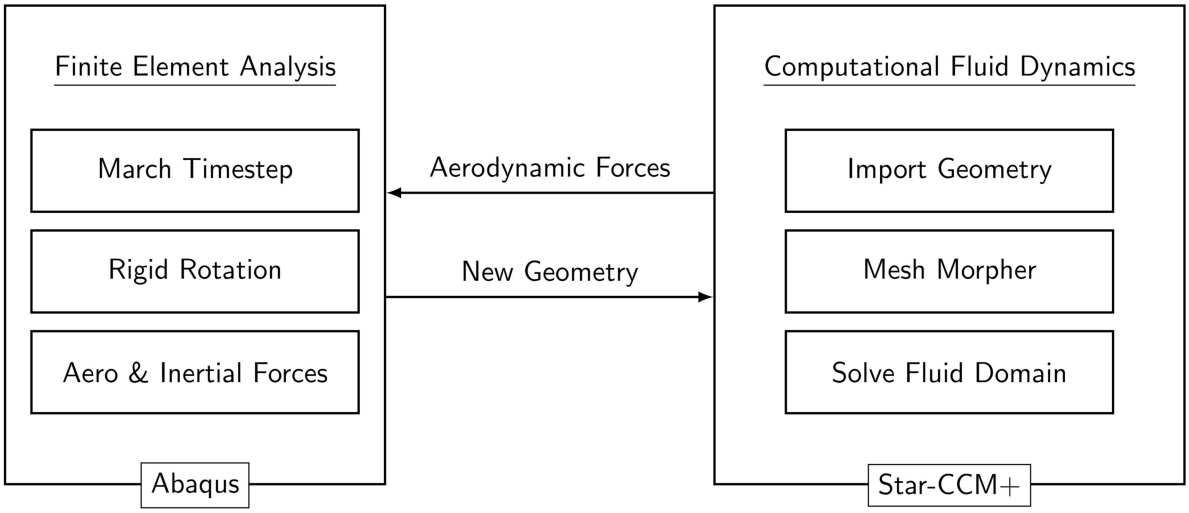

Figure 2.4: Two-way coupled workflow between Abaqus FEA and Star-CCM+.Note that Abaqus starts the workflow without any applied aerodynamic forces from Star-CCM+ for the first timestep. This is justified by the assumed small aerodynamic load at the beginning of the flapping sequence.

affected by a moving boundary condition. Finally, Star-CCM+ calculates the pressure field across the top and bottom surfaces of the wing and multiplies pressure calculations with element areas to find the distributed aerodynamic force. These forces are sent to individual nodes in Abaqus to be treated as a load to combine with the inertial forces calculated from the rotation rate, and the process repeats. A simplified visual of this workflow can be seen in Figure 2.4.

16

A NOVEL FLUID-STRUCTURE INTERACTION FRAMEWORK FOR FLAPPING, FLEXIBLE WINGS

Contribution of Authors and Co-Authors

Manuscript in following chapter

Author: [Ryan Schwab]

Contributions: [Development of computational fluid dynamics model]

Author: [Erick Johnson]

Contributions: [Assistance in development of computational fluid dynamics model]

Author: [Mark Jankauski]

Contributions: [Development of reduced order model based on blade element theory]

Manuscript Information

[R. Schwab, E. Johnson, M. Jankauski]

[Journal of Vibrations and Acoustics]

Status of Manuscript:
____ Prepared for submission to a peer-reviewed journal
____ Officially submitted to a peer-reviewed journal
____ Accepted by a peer-reviewed journal
_X_ Published in a peer-reviewed journal

[ASME]
[December 2019]
[Volume 141, Issue 6]
[DOI: 10.1115/1.4044268]

A Novel Fluid–Structure Interaction Framework for Flapping, Flexible Wings

Ryan Schwab
Mechanical and Industrial Engineering,
Montana State University,
Bozeman, MT 59717
e-mail: rschwab03@gmail.com

Erick Johnson
Assistant Professor
Mechanical and Industrial Engineering,
Montana State University,
Bozeman, MT 59717
e-mail: erick.johnson@montana.edu

Mark Jankauski[1]
Assistant Professor
Mechanical and Industrial Engineering,
Montana State University,
Bozeman, MT 59717
e-mail: mark.jankauski@montana.edu

Fluid–structure interaction (FSI) plays a significant role in the deformation of flapping insect wings. However, many current FSI models are high-order and rely on direct computational methods, thereby limiting parametric studies as well as insights into the physics governing wing dynamics. We develop a novel flapping wing FSI framework that accommodates general wing geometry and fluid loading. We use this framework to study the unilaterally coupled FSI of an idealized hawkmoth forewing considering two fluid models: Reynolds-averaged Navier–Stokes computational fluid dynamics (RANS CFD) and blade element theory (BET). We first compare aerodynamic modal forces estimated by the low-order BET model to those calculated via high fidelity RANS CFD. We find that for realistic flapping kinematics, BET estimates modal forces five orders of magnitude faster than CFD within reasonable accuracy. Over the range flapping kinematics considered, BET and CFD estimated modal forces vary maximally by 350% in magnitude and approximately $\pi/2$ radians in phase. The large reduction in computational time offered by BET facilitates high-dimensional parametric design of flapping-wing-based technologies. Next, we compare the contributions of aerodynamic and inertial forces to wing deformation. Under the unilateral coupling assumption, aerodynamic and inertial-elastic forces are on the same order of magnitude—however, inertial-elastic forces primarily excite the wing's bending mode whereas aerodynamic forces primarily excite the wing's torsional mode. This suggests that, via conscientious sensor placement and orientation, biological wings may be able to sense independently inertial and aerodynamic forces.
[DOI: 10.1115/1.4044268]

Keywords: aeroelasticity, dynamics, flow-induced vibration, flapping wing mechanics, fluid–structure interaction

1 Introduction

Micro air vehicles (MAVs) have become a pervasive technology over the past decade. They are considered for countless applications ranging from package delivery to storm tracking and forecasting. Many applications require MAVs to be very small so that they are able to negotiate dense, congested environments. For example, a MAV designed to identify leaks at gas refineries must be tiny enough to negotiate complex piping networks. Unfortunately, fixed-wing or rotor-based aircraft suffers inefficiencies at small scale that preclude their flight. Viscous forces tend to dominate lift-generating aerodynamic forces, and conventional rotary motors cannot effectively dissipate heat [1,2]. As a result, robotic designers generally rely on flapping wings as an alternative mechanism to produce lift and thrust at small scale. Flapping wing micro air vehicles (FWMAVs) are relatively new robotic platforms that have realized flight at centimeter lengths and milligram weights [3]. Many of these platforms are designed using flapping wing insects as inspiration. However, several issues preclude widespread realization of these insect-inspired FWMAVs for useful tasks. These issues include inefficient energetics, heavy sensors, and material fatigue. A better understanding of insect flight, in particular, the flapping wing, can inform engineering design to overcome many of these technological challenges.

As an insect wing flaps, it bends and twists under both aerodynamic and inertial-elastic forces [4]. The interplay of aero and structural dynamics is called fluid–structure interaction (FSI). The wing's deformation is speculated to serve several important functions, including energy management [5–7] and angular rate sensing [8]. Flexible wings offer higher lift-to-drag ratios relative to their rigid counterparts [9], suggesting wing deformation benefits *aerodynamic* power economy; flexibility is hypothesized to reduce *inertial* power requirements, as well. Unlike rigid wings, compliant wings store strain energy while flapping [10]. Much of this stored energy can be recruited to accelerate or decelerate the wing over a wingbeat, and this energy recycling mechanism improves inertial power economy [7]. Thus, wing compliance and deformation are central to the energy efficiency of small-scale biological flight. However, wing flexibility also provides a necessary sensing modality. Many insect wings are permeated with camaniform sensilla, a mechanoreceptor which responds to stress and strain [11]. The low-latency mechanical feedback encoded by these receptors allows the insect to react quickly to environmental perturbations [8], such as wind gusts or collisions with plants. Given the multifaceted characteristics of insect wings, they are an ideal structure to emulate in bio-inspired technologies. Nevertheless, the fluid and structural dynamics of flapping, flexible insect wings are not well understood.

Much research in the area of insect flight focuses on experimental studies. In a seminal study, Combes and Daniel artificially flapped a hawkmoth *Manduca sexta* in both air and helium (≈15% the density of air) with single degree-of-freedom (SDOF) rotation [4]. The objective of this study was to identify if inertial-elastic or aerodynamic forces were primarily responsible for wing deformation. They used high-speed videography to track several points over the wing surface while flapping and compared the deflection of these points both in air and in helium. Interestingly, they observed that wing deformation was similar in both cases; the natural conclusion was that the wing's dynamic response was primarily a function of inertial-elastic forcing. Norris later conducted a similar study with two notable differences: the wing was actuated in coarse vacuum rather than helium, and the full-field displacement was

[1]Corresponding author.

Contributed by the Technical Committee on Vibration and Sound of ASME for publication in the Journal of Vibration and Acoustics. Manuscript received December 6, 2018; final manuscript received July 15, 2019; published online July 31, 2019. Assoc. Editor: Maurizio Porfiri.

measured (at limited time steps) rather than displacement at individual points [12]. Contradictory to the findings of Combes and Daniel, Norris asserted that the contribution of fluid loading to the wing cannot safely be neglected. The conflicting results of these two studies suggest that the relative contribution of aerodynamic and inertial-elastic forces to wing deformation remains unknown.

To provide deeper insight into structural deformation and flapping wing FSI, many researchers rely on numerical simulation and modeling. Most flapping wing FSI models utilize coupled finite element analysis (FEA) and computational fluid dynamics (CFD) [13–16]. While such approaches accurately describe wing deformation and the surrounding flow field, the time required to generate a single solution is extensive. Both fluid and structural solvers suffer computational inefficiencies and these inefficiencies are compounded when the two physical regimes are considered together. For example, large wing rotations give rise to centrifugal and gyroscopic effects which cause the FEA stiffness matrix to be time-varying [17]. The stiffness matrix must be updated at each interval of analysis, and the result is an enormous number of degrees-of-freedom (DOFs) on the order of number of finite elements × number of time steps. Each physical DOF must be solved independently and the lengthy solution time makes direct FEA simulation in an impractical analysis method for dynamic systems subject to large rotation. CFD solvers, which typically rely on Reynolds-averaged Navier–Stokes (RANS) methods in the context of flapping flight, must resolve the flow field over an entire control volume to estimate the pressures on a wing. The extensive number of equations that must be solved and conditions that must be satisfied render CFD a computationally demanding mechanism. Therefore, given their computational demands, direct FSI models which leverage coupled CFD and FEA are not well suited for parameter studies.

To circumvent these computational issues, several methods were developed to study flapping wing flight more efficiently. The most common aerodynamic model is based upon blade element theory (BET), a quasi-steady approach that discretizes the wing into airfoils [18–20]. BET has been used to identify power-minimizing flapping kinematics [21], to explore the influence of inertial torques on insect steering [22], and to estimate passive pitch rotation in robotic vehicles [23]. However, while BET produces aerodynamic force estimates extraordinarily quickly, it is conventionally applied to rigid wings and is not widely used to study flapping wing FSI. Notable exceptions include works by Wang et al. [24] and Stanford et al. [25]. Wang developed a BET-based FSI model of twistable wings and showed that torsional flexibility improves power efficiency. However, their model was unable to account for spanwise bending. Stanford's FSI model was able to capture bending, but the discretization was limited to coarse chord-wise elements and could not account for the complex deformation modes observed in insect flight. Consequently, it is unknown if FSI models rooted in BET can adequately describe the realistic deformation of insect wings. We recognize that BET-FSI models and other reduced-order approaches have been used to describe other rotating systems influenced by aerodynamics, such as wind turbines and rotor blades [26–29]. However, the small length scale, high-frequency actuation, and multidimensional rotational kinematics of flapping insect wings render this a unique and challenging problem that has not been adequately addressed in a reduced-order fashion.

Given the motivation, there are two objectives of this paper: (1) evaluate the accuracy of a reduced-order flapping wing FSI model based upon BET and (2) identify the relative contribution of inertial-elastic and aerodynamic forces to wing deformation at a moth scale. To achieve these objectives, we develop a novel FSI model with the following characteristics. First, the model is general enough to accommodate arbitrary wing geometry and any fluid modeling scheme, including BET and CFD. Second, the model permits either unilateral or bilateral fluid–structure coupling. The general model derived here is the primary research contribution of this work. For the remainder of the paper, we stress that the primary interest is the physics governing structural deformation rather than the effect structural deformation has on the surrounding flow structure.

In this work, we consider only unilateral coupling, where the fluid affects the structure but the deforming structure does not affect the fluid. For unilateral coupling, aerodynamic forces are determined assuming wing rigidity and are subsequently applied to determine structural deformation. The assumption is most appropriate when wing deflections are small. To the best of our knowledge, there are no existing studies that compare the accuracy of unilaterally and bilaterally coupled FSI models of flapping wings. Thus, while this assumption may not be appropriate for the broad range of biological or artificial fliers, it is a suitable starting place to begin understanding the complex FSI of flapping wings. The unilateral approach enables us to study large parameter spaces more quickly than the bilateral approach, since the bilateral approach necessitates remeshing of the CFD grid at each interval of analysis. This assumption also helps us to identify under what parameters wing deformation becomes large enough to consider a bilaterally coupled analysis. For these reasons, we focus on unilateral FSI coupling for this work and will address bilateral FSI coupling in the future research. However, we acknowledge that some dynamic phenomena, for example, fluid damping, will not be present in the proposed unilateral approach.

The remainder of the paper is organized as follows. First, the aeroelastic framework is derived using the Lagrangian approach. Generalized aerodynamic loading is accounted for via the principle of virtual work. We then detail the BET and RANS CFD fluid models used in this research. The resulting aeroelastic framework is applied to study the FSI of a simulated hawkmoth wing. Then, we assess the accuracy of BET for hovering flight flapping kinematics and evaluating the sensitivity of BET as kinematics deviate from the hovering case. We next compare the relative contributions of aerodynamic and inertial-elastic forces to wing deformation. Lastly, we discuss our findings and how they are relevant to the design and optimization of FWMAVs as well as the study of biological flight.

2 Theory

We first develop a reference frame fixed to the rigid body motion of a flapping wing. We then derive the aeroelastic framework governing the wing modal response, where the structural response is determined via the Lagrangian formulation and nonconservative aerodynamic modal forces are accounted for through the principle of virtual work. We conclude by discussing the two aerodynamic loading models utilized in this work, specifically BET and RANS CFD.

2.1 Aeroelastic Modeling. The structural framework detailed in this section was originally developed by Jankauski and Shen [17]. However, the initial formulation assumed inertial-elastic forces were solely responsible for wing deformation—aerodynamic forces were neglected. While this assumption may be justified within the context, there are scenarios in which aerodynamic forces contribute nontrivially to deformation. Thus, the primary purpose of this work is to identify how aerodynamics affect the structural dynamics of flapping, flexible wings during hovering flight. The aeroelastic framework required to explore this subject is derived as follows.

Consider a wing of arbitrary geometry placed into an XYZ inertial coordinate frame (Fig. 1). The XYZ is rotated about the X axis with amplitude α, where α denotes roll. The subsequent $x''y''z''$ is rotated about the y'' axis with amplitude β, where β denotes pitch. The $x'y'z'$ frame undergoes a final rotation about the z' axis with an amplitude γ, where γ denotes yaw. The origin of the terminal xyz frame is a fixed point. The terminal frame is bound to the rigid body motion of the wing and has an angular velocity

$$\vec{\Omega} = \underbrace{(\dot{\alpha}\cos\beta\cos\gamma + \dot{\beta}\sin\gamma)}_{\Omega_x}\vec{e}_x + \underbrace{(\dot{\beta}\cos\gamma - \dot{\alpha}\cos\beta\sin\gamma)}_{\Omega_y}\vec{e}_y + \underbrace{(\dot{\gamma} + \dot{\alpha}\sin\beta)}_{\Omega_z}\vec{e}_z \tag{1}$$

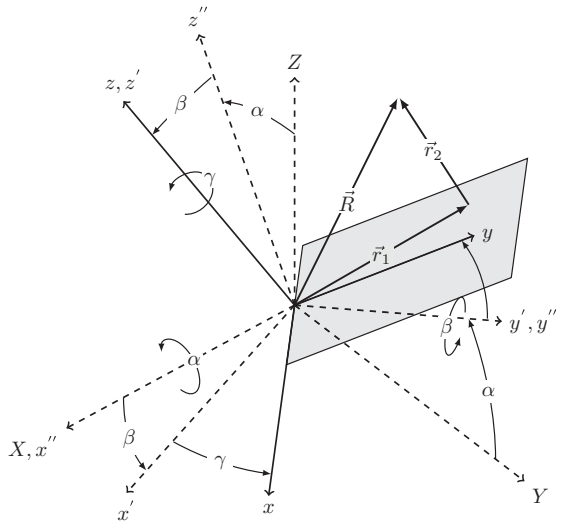

Fig. 1 Rotating reference frame attached to the rigid body motion of the wing

where $\vec{e}_x - \vec{e}_y - \vec{e}_z$ are unit vectors along the rotated frames x–y–z axes and Ω_x, Ω_y, and Ω_z are the components of the angular velocity vector. Next, a position vector $\vec{R}$ is drawn from the fixed reference frame origin to a differential mass dm. For convenience, the position vector $\vec{R}$ is represented as $\vec{R} = \vec{r}_1 + \vec{r}_2$, where

$$\vec{r}_1 = x\vec{e}_x + y\vec{e}_y \tag{2}$$

$$\vec{r}_2 = W(\vec{r}_1, t)\vec{e}_z \tag{3}$$

Above, $\vec{r}_1$ represents the planar coordinates of dm with respect to the undeformed wing and $\vec{r}_2$ represents a infinitesimal out-of-plane elastic deformation contingent on both space and time. In-plane motion is neglected. The velocity of dm is

$$\dot{\vec{R}} = \vec{\Omega} \times \vec{R} + \dot{\vec{r}}_2 \tag{4}$$

We determine the kinetic and potential energy of dm and integrate them over the wing's mass and volumetric domains, respectively, such that the total kinetic energy T and potential energy U are

$$T = \frac{1}{2}\int_m \dot{\vec{R}} \cdot \dot{\vec{R}}\, dm \tag{5}$$

$$U = \frac{1}{2}\int_V \hat{S}(W, W)dV \tag{6}$$

where $\hat{S}$ is a symmetric, quadratic strain energy density function. Next, we discretize the elastic deformation into an infinite series of space-dependent mode shapes $\phi_k(\vec{r}_1)$ multiplied by time-dependent modal responses $q_k(t)$ such that

$$W(\vec{r}_1, t) = \sum_{k=1}^{\infty} \phi_k(\vec{r}_1)q_k(t) \tag{7}$$

Vibration mode shapes are normalized with respect to the wing mass to satisfy the following orthonormal conditions:

$$\int_m \phi_k \phi_r dm = \delta_{kr} \tag{8}$$

$$\int_V \hat{S}(\phi_k, \phi_r)dV = \omega_k^2 \delta_{kr} \tag{9}$$

where ω_k is the wing's kth natural frequency and δ_{kr} is the Kronecker delta. We define two vector quantities $\vec{a}_k$ and $\vec{b}_k$. $\vec{a}_k$ is a weighted vector directed from the fixed origin of the rotating frame to the inertial force center of the kth vibration mode, and $\vec{b}_k$ is a $\pi/2$ counter-clockwise rotation of $\vec{a}_k$. These vectors are

$$\vec{a}_k = \int_m \phi_k(x\vec{e}_x + y\vec{e}_y)dm \tag{10}$$

$$\vec{b}_k = \int_m \phi_k(-y\vec{e}_x + x\vec{e}_y)dm \tag{11}$$

Using these definitions, we write the canonical definitions of kinetic and potential energy (Eqs. (5) and (6)) as

$$\begin{aligned} T = &\frac{1}{2}\vec{\Omega}^T \mathbf{I}_0 \vec{\Omega} + \frac{1}{2}(\Omega_x^2 + \Omega_y^2)\sum_{k=1}^{\infty} q_k^2 \\ &+ \frac{1}{2}\sum_{k=1}^{\infty} \dot{q}_k^2 - \Omega_z \vec{\Omega} \cdot \sum_{k=1}^{\infty} \vec{a}_k q_k - \vec{\Omega} \cdot \sum_{k=1}^{\infty} \vec{b}_k \dot{q}_k \end{aligned} \tag{12}$$

$$U = \frac{1}{2}\sum_{k=1}^{\infty} \omega_k^2 q_k^2 \tag{13}$$

where $\mathbf{I}_0$ is the inertial tensor of the wing with respect to the reference frame origin. For a flat wing of negligible thickness, $\mathbf{I}_0$ is

$$\mathbf{I}_0 = \int_m \begin{bmatrix} y^2 & -xy & 0 \\ -xy & x^2 & 0 \\ 0 & 0 & x^2 + y^2 \end{bmatrix}, \quad dm = \begin{bmatrix} I_{xx} & I_{xy} & 0 \\ I_{xy} & I_{yy} & 0 \\ 0 & 0 & I_{zz} \end{bmatrix}$$

where I_{xx}, I_{yy}, and I_{zz} are the moments of inertia about the x, y, and z axes, respectively, and I_{xy} is the x–y product of inertia. Prior to formulating the Lagrangian and determining the equation of motion governing q_k, we account for the nonconservative forces acting on the wing surface. Given that in-plane deformation is neglected, we consider only aerodynamic forces normal to the wing surface F_N. We incorporate the physical aerodynamic force into the modal equation of motion using the principle of virtual work. The virtual work $\delta\mathcal{W}$ done by the aerodynamic force is

$$\delta\mathcal{W} = \int_{S_w} F_N(\vec{r}_1, t)\delta W(\vec{r}_1, t)dS_w \tag{14}$$

$$\delta\mathcal{W} = \int_{S_w} F_N(\vec{r}_1, t)\sum_{k=1}^{\infty} \phi_k(\vec{r}_1)\delta q_k(t)dS_w \tag{15}$$

where S_w is the surface area of the wing. The nonconservative generalized force Q_k corresponding to the q_k degree-of-freedom is

$$Q_k = \int_{S_w} F_N(\vec{r}_1, t)\phi_k(\vec{r}_1)dS_w \tag{16}$$

With each modal excitation known, we now determine the equation of motion governing generalized coordinate q_k using the Lagrangian formulation. For q_k, the general form of Lagrange's equation is

$$\frac{d}{dt}\left(\frac{\partial T}{\partial \dot{q}_k}\right) - \frac{\partial T}{\partial q_k} + \frac{\partial U}{\partial q_k} = Q_k \tag{17}$$

After substituting the explicit forms of T and U (Eqs. (12) and (13)) into Eq. (17), the equation of motion for q_k is

$$\ddot{q}_k + [\omega_k^2 - (\Omega_x^2 + \Omega_y^2)]q_k = \dot{\vec{\Omega}} \cdot \vec{b_k} - \Omega_z \vec{\Omega} \cdot \vec{a}_k + Q_k \tag{18}$$

The equation of motion is linear and time-varying, where the time variance occurs in the stiffness term due to centrifugal softening. The modal excitation terms to the right-hand side of the equation

correspond to the Euler force, centrifugal force, and aerodynamic force, respectively.

The advantage of this model resides with its generality. It can accommodate any flapping wing for which mode shape and natural frequency data are available. Both quantities can be determined experimentally or through numerical methods such as static FEA. Moreover, this framework can accommodate any fluid loading scheme, ranging from low-fidelity BET approaches to higher-fidelity CFD. It can account for unilateral coupling or bilateral coupling. In the former, the fluid affects the structure but not vice versa, and in the latter, the structural and fluid physics are solved simultaneously. In the sections that follow, we demonstrate the utility of our model investigating a simulated *M. sexta* insect wing.

2.2 Fluid Modeling. To determine the aerodynamic modal forces Q_k, we must first identify the physical aerodynamic force F_N. We consider two fluid modeling approaches in this work: BET and RANS CFD. BET is a reduced-order quasistatic method that approximates aerodynamic forces quickly; however, the method relies on empirical coefficients and lacks the quantitative accuracy of higher-fidelity approaches. RANS is the gold standard for flapping wing fluid dynamics, though the appreciable computational resources required to generate CFD solutions renders this method undesirable for parametric studies. These two fluid dynamics models are detailed in Secs. 2.2.1 and 2.2.2.

2.2.1 Blade Element Theory. Quasi-steady BET is used frequently in the study of insect flight and is useful for reduced-order modeling of wings with high aspect ratios. There are numerous formulations based upon BET which range from relatively basic to reasonably complex [19,21,23]. While BET cannot model certain dynamic phenomena such as clap-and-fling, wing–wake interactions, or dynamic stall that are important to the flight dynamics of many flapping wing fliers [30,31], it does provide order-of-magnitude estimates of aerodynamic forces and moments at substantially lower computational costs compared to direct fluid solvers such as RANS CFD. BET is most suitable for coarse parameter studies where absolute quantitative accuracy is not essential and where high-order fluid solvers are prohibitive. Once approximate solution trends have been identified via BET, high-fidelity CFD can be used to verify the accuracy of BET for parameter sets of interest. This verification will indicate whether or not dynamic effects unaccounted for by the BET formulation will significantly alter aerodynamic loading. In this work, we aim to identify a range over which BET approximates aerodynamic modal forces reasonably well compared to those determined via RANS CFD. We implement a very basic form of the BET framework to illustrate how well a crude fluid loading model performs relative to a higher-fidelity method. The BET formulation used hereafter originated in Ref. [22] and is summarized here for clarity. This previous work treated the wing as rigid and did not consider FSI.

The BET method partitions the wing into chord-wise strips called blade elements (Fig. 2). Each blade element is treated as an airfoil with constant depth. Assuming the aerodynamic coefficients and velocity of each blade element are known, the elemental aerodynamic forces can be calculated and integrated over the wing surface to yield the total forces. In general, the scalar differential force dF acting on a blade element is

$$dF_{[\cdot]} = \frac{1}{2} C_{[\cdot]} \rho_f \vec{V} \cdot \vec{V} dS_w \tag{19}$$

where $(1/2)\rho_f \vec{V} \cdot \vec{V}$ is the dynamic pressure, ρ_f is the fluid density, $\vec{V}$ is the relative velocity between the blade element and the air, C is an arbitrary aerodynamic coefficient, and dS_w is the differential surface area of the blade element, defined by the chord-width $c(r)$ multiplied by the differential length dr. $[\cdot]$ denotes a placeholder for lift (L) or drag (D). The velocity of a blade element is assumed constant across that element with respect to a reference point r on the wing, where r is coincident with the y axis. We choose

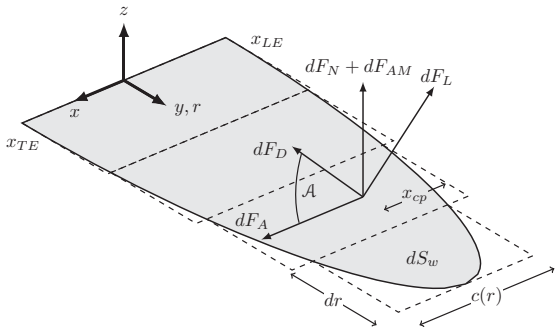

Fig. 2 Blade-element discretization of a wing. Differential aerodynamic forces shown acting at the center of pressure x_{cp} for a single element.

pitching axis as the velocity reference line to be consistent with other flapping wing BET models [20,23]. Because we assume hovering flight, the freestream air velocity is equal in magnitude and opposite in direction of the velocity of the element. The lift and drag coefficients to be substituted into Eq. (19) are

$$C_L(\mathcal{A}) = C_{L,\max} \sin(2\mathcal{A}) \tag{20}$$

$$C_D(\mathcal{A}) = \left(\frac{C_{D,\max} + C_{D,0}}{2}\right) - \left(\frac{C_{D,\max} - C_{D,0}}{2}\right) \cos(2\mathcal{A}) \tag{21}$$

where $C_{L,\max}$, $C_{D,\max}$, and $C_{D,0}$ are empirically measured coefficients. The aerodynamic angle of attack $\mathcal{A}$ is defined as the clockwise angle between $\vec{V}$ and the x axis, or

$$\mathcal{A} = \tan^{-1}\left(\frac{\vec{V} \cdot \vec{e}_z}{\vec{V} \cdot \vec{e}_x}\right) \tag{22}$$

Lift and drag forces are projected onto the wing's axial and normal directions by a simple rotation of $\mathcal{A}$ such that

$$dF_A = dF_D \cos\mathcal{A} - dF_L \sin\mathcal{A} \tag{23}$$

$$dF_N = dF_D \sin\mathcal{A} + dF_L \cos\mathcal{A} \tag{24}$$

Next, we account for added mass. Insect wings are extremely lightweight and have a large surface area; as a result, added mass cannot safely be neglected. The normal component of added mass acting on a blade element is

$$dF_{AM} = -\frac{\pi}{4}\rho_f c(r) r[\dot{\Omega}_x + \Omega_y \Omega_z] dS + \frac{\pi}{8}\rho_f c(r)^2 [c(r) + 2x_{\mathrm{TE}}(r)]\dot{\Omega}_y dr \tag{25}$$

This expression for added mass originated from Ref. [32] has been modified as per the reference frame and kinematics used in this work. We assume that the elemental aerodynamic forces act on the elemental center of pressure $x_{cp}(r)$. We estimate the location of x_{cp} using an approximate form of the empirical relationship in Ref. [23] as

$$x_{cp} = x_{LE}(r) + \frac{1}{4} c(r) |\mathcal{A}| \tag{26}$$

where x_{LE} is the wing's leading edge. Note that the aerodynamic force acts at a single discrete point within an element, whereas in reality, aerodynamic pressure acts over the entire wing surface. We stress that BET is subject to the assumptions that underlie thin airfoil theory. Without modification, BET is not well suited to account for large angles of attack or certain phenomena such as dynamic stall. These assumptions may limit the parameter space where BET provides good estimates of aerodynamic forces.

2.2.2 Reynolds-averaged Navier–Stokes Computational Fluid Dynamics. RANS is one of the most widely used formulations of the Navier–Stokes equations to simulate problems involving turbulent fluid flow. Instead of solving for the instantaneous velocity and pressure, RANS separates these variables into their mean $\langle[\cdot]\rangle$ and perturbed $[\cdot]'$ parts. Taking the average of the incompressible form of the equations results in conservation of mass

$$\frac{\partial <u_i>}{\partial x_i} = 0 \tag{27}$$

and conservation of momentum

$$\rho_f \frac{\partial \langle u_i \rangle}{\partial t} + \rho_f \frac{\partial}{\partial x_i}\left(\langle u_i \rangle \langle u_j \rangle\right) = \frac{\partial P}{\partial x_i} + \mu \nabla^2 \langle u_i \rangle - \frac{\partial \tau_{ij}}{\partial x_j} \tag{28}$$

where u_i is a component of fluid velocity, P is the pressure, μ is the dynamic viscosity, and $\tau_{ij} = \rho_f \langle u_i' u_j' \rangle$ is the Reynolds stress tensor [33]. While the Navier–Stokes equations are largely unchanged and permit a direct calculation of the mean velocity and pressure fields, the perturbed velocities remain within the stress tensor and require additional equations to model. The closure of the RANS equations has resulted in numerous turbulence models that facilitate, though are often insufficient approximations, modeling flow separation near walls.

The eddy viscosity hypothesis relies on assuming turbulence, and momentum diffusion operates under similar mechanisms [33]. This results in the Reynolds stress tensor being a function of a modeled viscosity and the kinetic energy of turbulent fluctuations, k, such that

$$\tau_{ij} = -\mu_t \left(\frac{\partial \langle u_i \rangle}{\partial x_j} + \frac{\partial \langle u_j \rangle}{\partial x_i}\right) + \frac{2}{3}\rho_f \delta_{ij} k \tag{29}$$

where δ_{ij} is the Kronecker delta tensor. The Spalart–Allmaras model is a one-equation model for turbulence closure that solves the transport of a modified diffusivity, which is then used to calculate the eddy viscosity μ_t [34,35]. The Spalart–Allmaras model allows for a compromise between computational efficiency and the difficulty most turbulence models have at capturing flow separation near a wall in highly dynamic systems.

A chimera meshing approach is adopted to account for the large body motions [36]. Unlike small body motions within a CFD simulation that shift surface nodes (and their neighbors to avoid creating negative-volume elements), large body motions often rely on remeshing significant portions of the entire domain. The added computational cost of regenerating a mesh and interpolating solution variables between these grids at each time step does not, however, guarantee that a mesh of sufficient quality is maintained. Alternatively, multiple high-quality meshes for the fluid domain empty of any boundaries (the *background* mesh) and a region surrounding the moving wing (the *overset* mesh) can be overlapped. These meshes remain unchanged throughout the simulation, with the overset mesh undergoing rigid body motion following the wing. At each time step, the region of overlap is determined and an enveloping shell of elements near the boundary of the overset mesh is used to interpolate between the solution in each region. A distance-weighted interpolation is used to couple the background and overset meshes into a strongly coupled system of equations.

dF_A, dF_N, and x_{cp} are easily queried from the time-varying mean velocity and pressure fields on the upper and lower surfaces of the wing. The component values of wall shear stress and pressure are transformed onto the wing reference frame and summed along chordwise and spanwise segments in order to match the desired resolution of the BET model. The Spalart–Allmaras RANS model with chimera grid within STAR-CCM+ v12.04 was used to produce the CFD results in this work.

3 Simulation

In this section, we apply the derived model to a fictitious hawkmoth *M. sexta* wing. We begin the section by describing all simulation parameters. We then (1) compare physical and modal aerodynamic forces predicted by BET and CFD, (2) assess the sensitivity of BET-estimated modal forces with respect to flapping kinematics, (3) compare inertial-elastic to aerodynamic modal forces, and (4) solve for the wing's response in air and in vacuum.

3.1 Simulation Parameters. We first identify the parameters necessary to carry out the simulation. All parameters are shown in Table 1. We develop an idealized model of a hawkmoth *M. sexta* wing using ABAQUS FEA. An image of the forewing is digitally traced to determine the to-scale wing planform. We assume that the wing has constant thickness and density. The values of these properties are estimated from Ref. [37]. Venation, camber, and spatial thickness variation are neglected. The FEA model is composed of 611 shell elements, which is a sufficient number of elements to show convergence of the wing's first two natural frequencies (Fig. 4). We retain the two vibration modes corresponding to these natural frequencies. The first is a bending mode and the second is a torsional mode (Fig. 3). Because of the geometric and structural simplifications of the FEA model, the natural frequencies of the wing had to be adjusted in postprocessing to agree with experimentally reported values [38] shown in Table 1. The first two inertial force center vectors are $\vec{a}_1 = -(0.57\vec{e}_x + 2.0\vec{e}_y) \times 10^{-4}$ and $\vec{a}_2 = -(0.42\vec{e}_x + 0.06\vec{e}_y) \times 10^{-4}$ in units kg/m^2.

Next, we discuss the parameters used for fluid modeling. For the CFD simulations, the wing is represented as an embedded surface within the overset mesh region. The simulation geometry is shown in Fig. 5. A prism layer was introduced to improve the boundary layer representation of the wing. A time step was specified to capture approximately 10 deg of wing rotation and a total of 10 rotation periods were simulated to reach a periodically steady response. Axial and normal forces for every surface element were exported at each time step. CFD parameters are summarized in Table 2. We conduct a mesh independent study that scaled the mesh size and maintained the relative size ratios throughout the simulation space. A mesh of nearly 2 million elements was considered converged, resulting in a root mean square error of 1.5% (with respect to the maximum force value) and an error of 2.5% for a grid of 442,595 elements. A time-step independence study was performed for the selected grid, and convergence was found at a time-step of 1.25×10^{-4} s (1.25 deg/time-step). This resulted in a root mean square error of 4% (with respect to the maximum force value) and a maximum peak error of 7.2% at a time-step of 1.0×10^{-3} s. While the selected time-step only results in 40 points per cycle, it was deemed to adequately capture the first-order forces and their profile within the scope of this paper and with tractable

Table 1 Structural, geometric, and aerodynamic simulation parameters

Variable	Description	Value	Unit
ω_1	First natural frequency	59	Hz
ω_2	Second natural frequency	75	Hz
m_w	Wing mass	47	mg
$C_{L,\max}$	Max lift coefficient	1.68	—
$C_{D,\max}$	Max drag coefficient	3.06	—
$C_{D,\min}$	Min drag coefficient	0.07	—
R	Wing span	54	mm
AR	Aspect ratio	3.48	—
A	Surface area	867	mm^2
$\bar{c}$	Mean chord width	15.5	mm
ρ_f	Fluid density	1.2	kg/m^3
t	Thickness	45	μm
ρ_w	Wing density	1200	kg/m^3

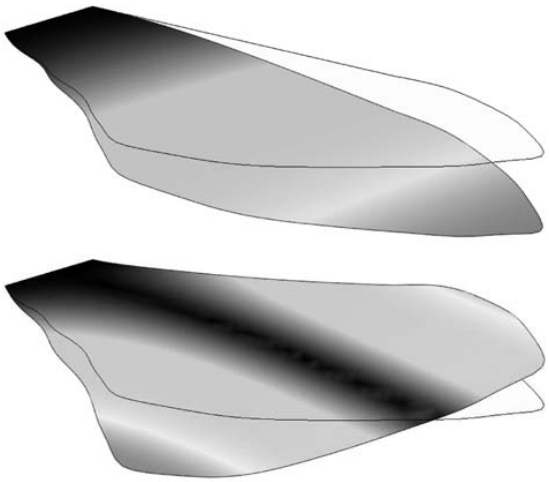

Fig. 3 First two vibration modes of model hawkmoth forewing. (Top) Spanwise bending mode and (bottom) spanwise torsion mode.

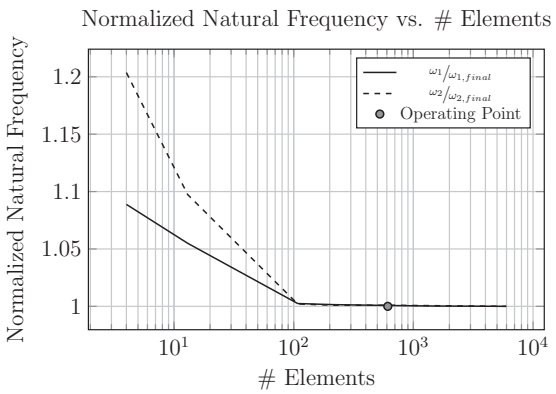

Fig. 4 Convergence study of the FEA model. The first and second natural frequencies normalized by their final values are plotted with respect to number of elements. We use 611 elements for the simulations carried out in this work.

computational times. Phase relationships were determined to be independent of the time step and mesh fineness.

For BET simulations, we discretize the wing into 20 blade elements. This number of elements showed convergence for lift averaged over a single wingbeat. The aerodynamic coefficients are taken from values reported in Ref. [21] for the hawkmoth. BET simulations are conducted numerically using MATLAB. All simulations occur over 25 wingbeats, where each wingbeat is divided into 100 equally spaced time intervals. Because CFD simulations occur on a much coarser time scale, all CFD results are interpolated in time to match the finer MATLAB time scale. All physical aerodynamic forces determined either via CFD or BET are transformed to modal aerodynamic forces through Eq. (16).

When solving for the wing modal responses, we introduce light modal damping ($\zeta = 0.05$) into both modes to attenuate the wing's free vibration. Results presented hereafter are taken once steady-state dynamics have been achieved. For frequency domain calculations, we use MATLAB's curve fitting toolbox to identify Fourier series coefficients and calculate signal magnitude and phase from these coefficients. All flapping kinematics are idealized as harmonic and of the form $\eta = \eta_0 \sin(\omega t + \phi_\eta)$, where η is a general

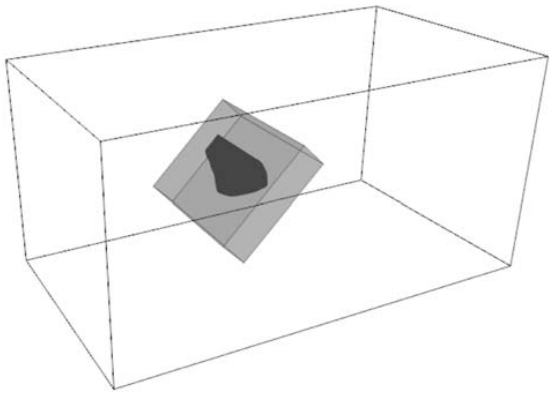

Fig. 5 CFD simulation geometry showing the background region (outline), overset region (shaded), and wing

Table 2 CFD simulation parameters

Variable	Description	Value	Unit
μ	Dynamic viscosity of air	1.85×10^{-5}	Pa · s
Δt	Time step	0.001	s
t_f	Simulation time	0.4	s
	Dimensions of the background mesh ($L \times W \times H$)	$200 \times 110 \times 100$	mm
	Mean element length of the background mesh	1.0	mm
	Number of elements in the background mesh	326,538	—
	Dimensions of the overset mesh ($L \times W \times H$)	$55 \times 70 \times 15$	mm
	Mean element length of the overset mesh	0.5	mm
	Mean element length of the wing surface	0.125	mm
	Number of prism layers off the wing	5 –	
	Prism layer growth rate	1.2	—
	Number of elements in the overset mesh	116,057	—
$\overline{y^+}$	Mean y-plus for one period of rotation	3.763	—

Table 3 Kinematic parameters for hovering flight

Variable	Description	Value	Unit
α_0	Roll amplitude	60	deg
β_0	Pitch amplitude	45	deg
γ_0	Yaw amplitude	0	deg
$\phi_{\alpha\beta}$	Pitch/roll phase difference	$\pi/2$	rad
ω	Flap frequency	25	Hz

rotation function that represents roll, pitch, or yaw, η_0 is the rotation amplitude, ω is the flapping frequency, and ϕ_η is the rotation phase. We consider only hovering flight in this work. We estimate flapping kinematics from Ref. [39], including pitch/roll rotation amplitudes, rotation phase, and flap frequency. We neglect wing yaw which is typically small in insect flight [39]. All kinematic parameters for hovering flight are shown in Table 3.

3.2 Physical and Modal Aerodynamic Forces. We begin by comparing the net aerodynamic normal force F_N calculated via BET and CFD. This comparison provides a baseline accuracy for the

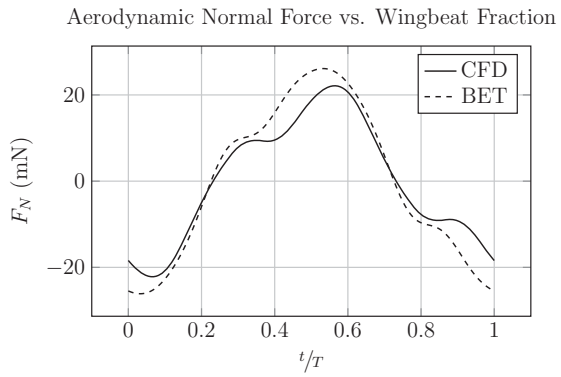

Fig. 6 Aerodynamic normal forces calculated via BET and CFD

BET method. If BET cannot estimate bulk aerodynamic forces within reasonable accuracy, it will be unable to estimate aerodynamic modal forces. In this case, we treat CFD as the ground truth. We calculate F_N using both methods and plot it as a function of wingbeat fraction t/T in Fig. 6.

Both fluid models indicate that F_N oscillates primarily at the driving frequency ω with a notable harmonic at 3ω. Overall, we see good agreement between CFD and BET both in magnitude and phase. Most notably, BET overestimates the primary response magnitude by approximately 30%. This discrepancy is likely due to aerodynamic coefficient constants as well as the idealized relationship between the aerodynamic coefficients and angle of attack (Eqs. (20) and (21)). In general, insect wings will deviate modestly in size and geometry; it is unlikely that a universal set of aerodynamic coefficients exits. Thus, BET is capable of estimating net aerodynamic forces for hovering flapping kinematics with reasonable agreement to CFD. Quantitative accuracy of the BET method is contingent on precise empirical aerodynamic coefficients.

Next, we consider aerodynamic modal forces Q_1 and Q_2. Aerodynamic modal forces are calculated via Eq. (16). For the CFD model, the spatial distribution of aerodynamic forces is known. Conversely, for the BET model, we know only the net force on each blade element and do not know the force distribution. We assume that the elemental aerodynamic normal force acts as a point load at the blade elements center of pressure. Aerodynamic modal forces calculated via CFD and BET are plotted in Fig. 7. The corresponding numeric values are shown in Table 4.

From this comparison, we see modal forces calculated via BET which agree qualitatively with those calculated via CFD. BET accurately predicts the frequency components as well as the phase of these components. In addition, BET agrees with CFD quantitatively for the second aerodynamic modal force Q_2. The ω components are nearly identical in magnitude and phase, and the 3ω components agree in magnitude. There is a slight discrepancy in the phase at 3ω. We observe that the BET-predicted second modal force is not as smooth as that predicted by CFD. This stems from the point load approximation used for the BET model. When the center of pressure crosses over the nodal line of the torsional mode (Fig. 3), the force contribution of that particular blade element to the modal response is effectively negated. In reality, there would be some force distribution about this center of pressure that would generate a smoother second modal force. However, this force distribution is unknown if the pressure coefficients c_p over the range of angles of attack for a blade element are unknown. Then, the nonsmooth behavior arising from the point-load approximation could introduce anomalous high-frequency components into Q_2, though these components likely do not affect the second modal response given that they will occur at frequencies much higher than the second natural frequency. Thus, even with the point load approximation, BET predicts the second modal response fairly well.

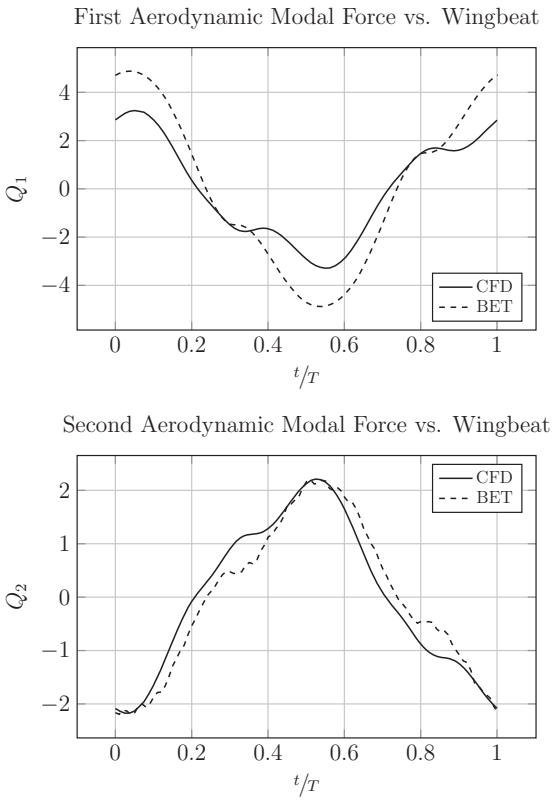

Fig. 7 Aerodynamic modal forces calculated via CFD and BET

Table 4 Numerical comparison between first and second aerodynamic modal forces estimated by BET and CFD for hovering flapping kinematics

	BET	CFD	BET	CFD
	Q_1	Q_1	Q_2	Q_2
$\lvert\omega\rvert$	4.52	2.84	1.92	1.91
$\lvert 3\omega\rvert$	0.67	0.69	0.34	0.35
$\angle\omega$ (rad)	0.08	−0.04	3.25	3.03
$\angle 3\omega$ (rad)	1.34	1.6	4.21	4.23
$\lvert\omega\rvert$ % diff.	58.9		0.26	
$\lvert 3\omega\rvert$ % diff.	3.4		3.2	
$\Delta\angle\omega$ (rad)	−0.12		−0.22	
$\Delta 3\angle\omega$ (rad)	0.27		0.02	

On the other hand, the discrepancy between CFD and BET estimates of Q_1 is larger. BET overestimates the primary response magnitude of Q_1 by approximately 50%. This suggests that BET predicts the spanwise location of the aerodynamic force center further along the r axis than CFD does. To verify this, we plot the time history of the elemental force dF_N as a function of blade element position r for both CFD and BET models. Results are shown in Fig. 8. Note that the spanwise aerodynamic force center moves along r over time with the CFD model and is stationary with the BET model. CFD predicts the time-averaged spanwise location of the aerodynamic force at $r \approx 3.52$ cm, whereas BET predicts it at $r \approx 3.94$ cm. Because the first bending mode (Fig. 3) varies approximately quadratically along the r axis, even a small increase in the spanwise position of the aerodynamic force center significantly affects the first modal force.

Thus, it appears that BET can only crudely estimate the position of the aerodynamic force center. We believe that this is in part

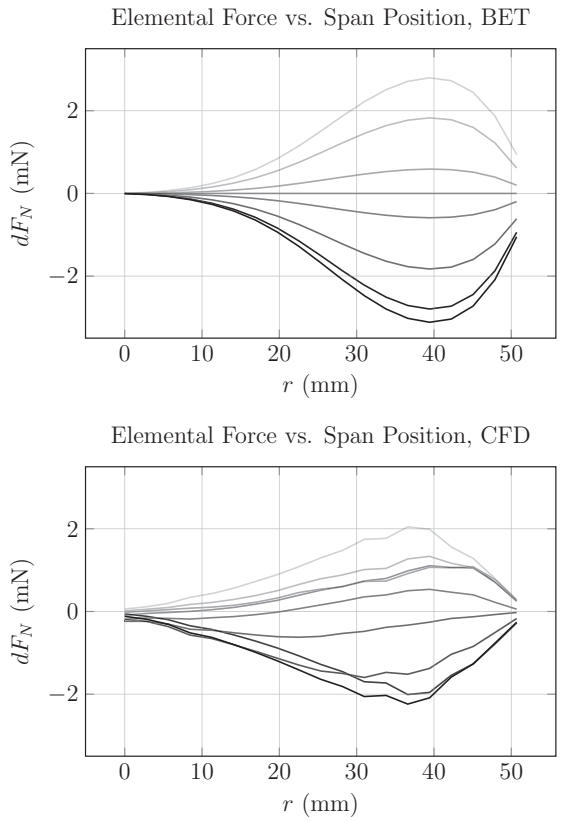

Fig. 8 Elemental aerodynamic normal force dF_N as a function of spanwise position r for both CFD and BET models. Time history shown over a half wingbeat. Dark lines indicate the beginning of the half wingbeat, and lighter lines indicate the end of the half wingbeat.

because BET is not well suited to account for rotational forces. By convention, the blade element velocity is referenced from a line coincident with the y axis (Fig. 2). This implies that if a wing is undergoing pure pitch about the y axis, BET predicts no aerodynamic forces acting on the wing except for those imparted by added mass. Consequently, at least some forces associated with dynamic pitching are not accounted for simply because of the velocity reference line r. However, other rotational forces must be considered to improve the BET formulation as well. For example, Kramer observed that rapid changes in an airfoils angle of attack lead to short spikes in lift force [40]. He conjectured that these spikes were associated with flow separation, where the fluid becomes detached from the surface of an object. Given that an insect wing changes angles of attack rapidly, these dynamic factors may play a nontrivial role in aerodynamic loading. While rotational terms have been incorporated into BET [18,23,41], most are case-specific and cannot be applied with generality. We were unable to incorporate rotational terms into our BET model that reduced the difference between BET and RANS estimated modal forces for all parameters considered in the sensitivity study that follows (Fig. 9). Whitney and Wood used the BET method to estimate the aerodynamic forces of a small flapping wing robot and were also unable to improve model-theory agreement by incorporating a rotational lift term [23]. Sane and Dickinson suggest that rotational coefficients are sensitive to the location of the pitching axis as well as pitching rate and amplitude [18], which makes it difficult to model as a quasi-steady force without sufficient empirical data.

Despite the limitations of BET, it remains a useful tool that provides reasonable estimates of modal forces at significantly reduced computational costs relative to CFD. In this case, BET predicts modal forces staggering five orders-of-magnitude faster than CFD. This enormous reduction in computational time can expedite parametric studies considering wing geometry, mass/stiffness distributions, and flapping kinematics. However, up to this point, we have considered only hovering flight flapping kinematics. It is possible that the BET model breaks down for deviations from these kinematics.

3.3 Sensitivity of Blade Element Theory. In Sec. 3.2, we saw that BET predicted the first and second aerodynamic modal forces reasonably well for hovering flapping kinematics. In this section, we explore how deviations from hovering flapping kinematics affect the agreement between CFD and BET calculated modal forces. Pohly et al. compared BET and CFD fluid models for various flapping kinematics [42]; however, this study focused on how well BET estimates bulk aerodynamic forces (e.g., net lift and thrust) for rigid wings. To estimate the range of parameters over which BET can be used to model FSI, it is more suitable to compare aerodynamic modal forces rather than bulk aerodynamic forces.

For our sensitivity analysis, we consider four kinematic parameters; roll amplitude α_0, pitch amplitude β_0, phase difference between pitch and roll $\phi_{\alpha\beta}$, and driving frequency ω. Starting from their nominal value in hovering flight (Table 3), we vary each rotation parameter from $\pm\pi/8$ in $\pi/16$ increments. We also consider driving frequencies of 15, 25, and 35 Hz for normal hovering kinematics. We do not consider simultaneous variation of parameters because of how computationally demanding CFD solutions are. Nonetheless, varying parameters individually provides a good initial picture of how well BET estimates modal forces under different scenarios.

For each set of parameters, we calculate the first and second aerodynamic modal forces Q_1 and Q_2 via both BET and CFD. Because the modal forces oscillate both at the driving frequency and three times the frequency, we must determine the magnitude and phase at both ω and 3ω. Across all parameters tested, we did not identify any other significant frequency components. We then determine the percent error between the modal force magnitude at each frequency component assuming that CFD provides the "true" solution. We also identify the phase differences at ω and 3ω between CFD and BET modal forces. These calculations are tabulated numerically in Table 4 as an example for hovering flapping kinematics. The percent error and phase difference for deviations from hover kinematics are plotted in Fig. 9.

Overall, BET estimates modal forces reasonably well in both magnitude and phase for modest deviations from hovering flight kinematics. The magnitude error and phase difference of both ω and 3ω components of Q_1 and Q_2 are fairly insensitive to changes in driving frequency. Small changes ($\pm\pi/16$) in rotational kinematic parameters generally had a minor effect on the dominant ω component magnitude error and phase difference of Q_1 and Q_2. The effect of these small changes on the 3ω components of Q_1 and Q_2 is somewhat more pronounced. For Q_1, errors in the magnitude and phase of 3ω components likely do not affect the first modal response significantly. This is because the 3ω component is much smaller in magnitude than the ω component for Q_1, and the wing's first natural frequency does not fall near 3ω ($\omega_1 \approx 59$ Hz). However, the 3ω errors in magnitude and phase of Q_2 may more substantially affect the second modal response because the wing's second natural frequency is near 3ω ($\omega_2 \approx 75$ Hz). Nonetheless, the magnitude error for both ω and 3ω of Q_1 and Q_2 for kinematic deviations of $\pm\pi/16$ is maximally 125%. This suggests that BET performs fairly well for small kinematic deviations.

We observe more significant errors for larger changes ($\pm\pi/8$) in rotational kinematic parameters. Such errors generally occur in the 3ω components of modal forces. However, the largest errors

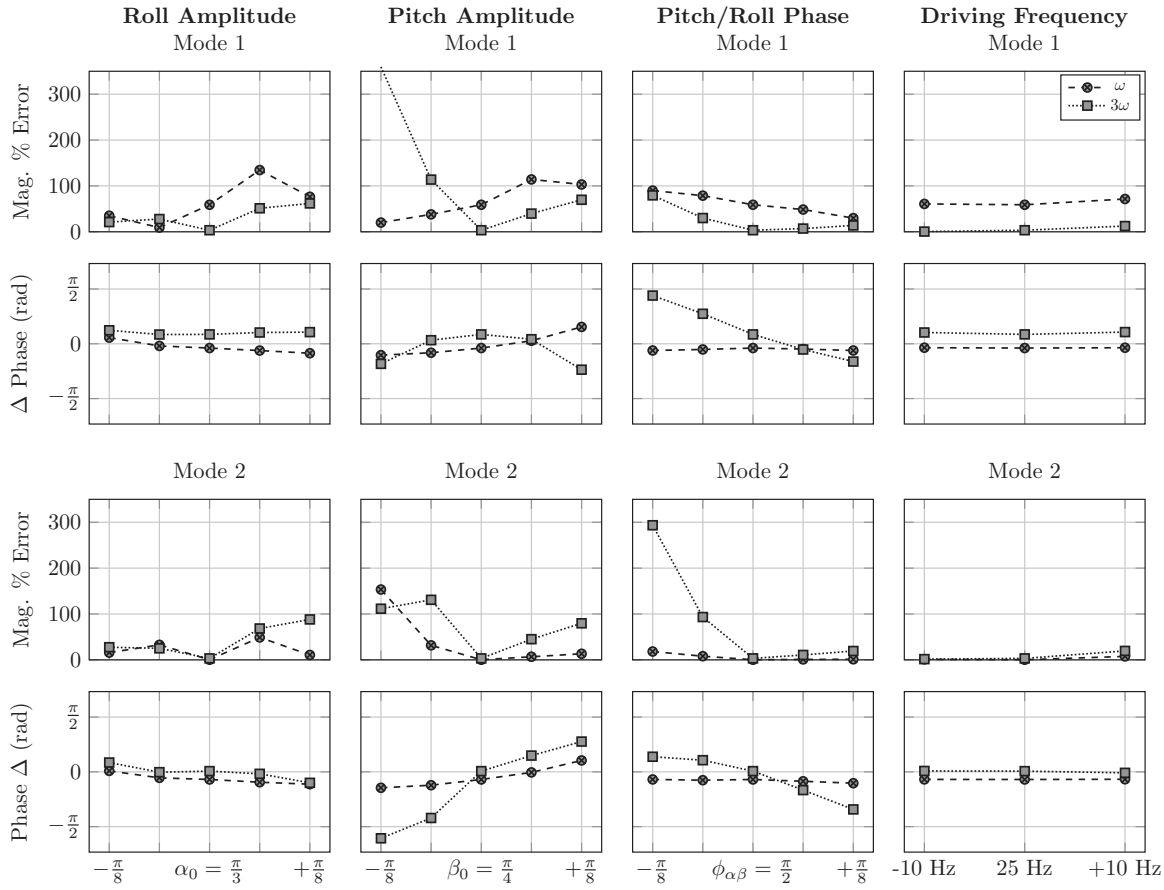

Fig. 9 Sensitivity of BET first and second aerodynamic modal forces as flapping kinematics deviates from hovering flapping kinematics

often coincide with flapping kinematics that would not exist in nature. For example, when the pitch amplitude is reduced by $\pi/8$, the percent error in the 3ω component of Q_1 is over 300% and the phase difference for the 3ω component of Q_2 is roughly $-\pi/2$. While these errors are significant, the reality is that if the pitch amplitude were reduced by $\pi/8$, the insect would produce far less lift than required to fly. For this pitch amplitude, CFD estimates an averaged vertical force of 12.5 mN whereas a hawkmoth that weights roughly 2.0 g [43] would require closer to 20 mN vertical force to fly. The other most significant errors occur when the pitch/roll phase deviates $\pm\pi/8$; however, these kinematics also produce insufficient vertical force for flight.

It is difficult to identify, with absolute certainty and across all parameters considered, why errors between CFD and BET tend to grow as flapping kinematics deviate from those observed in hovering. However, we believe that away from these nominal kinematics, phenomena that are not modeled by BET become increasingly important to CFD-estimated modal forces. Consider when pitch amplitude is increased by $\pi/8$. In this case, the wing undergoes a rotation upon stroke reversal larger than what is typical in hovering. Since rotational affects are not accounted for via BET, we suspect that errors may become greater for increased pitching amplitudes. At the same time, if pitch amplitude is reduced by an equivalent amount, the wing would be nearly vertical and have a very large angle of attack mid-stroke. This poses issues for the classical thin airfoil theory on which BET is based, which is more accurate for small angles of attack because of stall effects at high angles of attack. Thus, there are many mechanisms that could affect the agreement between CFD and BET away from nominal hovering kinematics, but these mechanisms must be treated on a case by case basis.

Despite these differences, the sensitivity analysis also suggests that certain dynamic phenomena unmodeled in BET (e.g., flow separation) only modestly affect its agreement with CFD. Consider the case where roll amplitude is increased from $\alpha_0 = \pi/3 + \pi/16$ to $\alpha_0 = \pi/3 + \pi/8$. CFD shows that the flow is attached to the wing for the lesser roll amplitude, whereas it separates for the greater roll amplitude. But, over this range of roll amplitudes, the maximal magnitude error is 100% and the maximum phase difference is approximately $\pi/10$ for both ω and 3ω components. This suggests that in some cases, quasi-steady aerodynamic forces are larger than or of similar magnitude to aerodynamic forces imparted by dynamic phenomena. Consequently, BET appears to be a reasonable first approximation of aerodynamic modal forces for flapping kinematics that deviate modestly from those seen in hover.

3.4 Inertial-Elastic Versus Aerodynamic Modal Forces and Responses. We now compare inertial-elastic modal forces to aerodynamic modal forces. This comparison provides insight into which physical regime dominates wing deformation in hovering flight conditions. To clarify, both Euler and centrifugal forces (Eq. (18)) are considered inertial-elastic forces. The first and second modal forces are shown in Fig. 10. BET estimated modal forces are omitted from Fig. 10 for clarity.

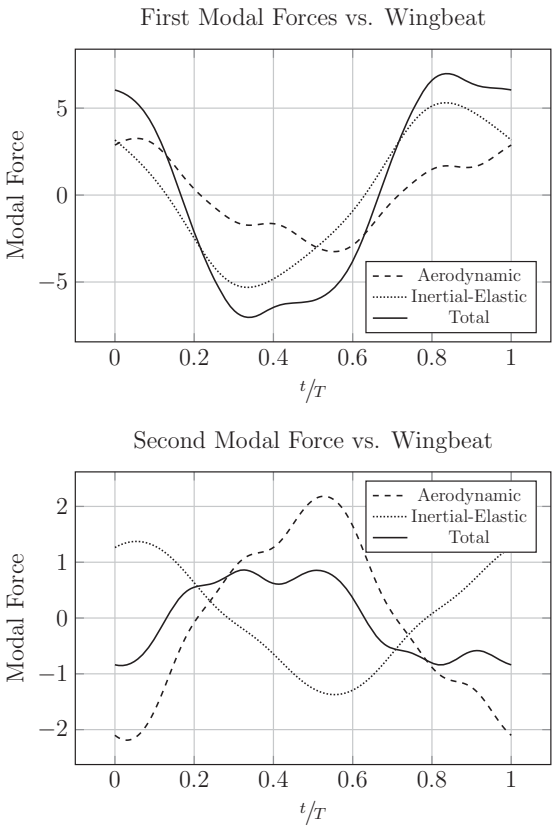

Fig. 10 CFD predicted aerodynamic and inertial-elastic modal forces for first two vibration modes

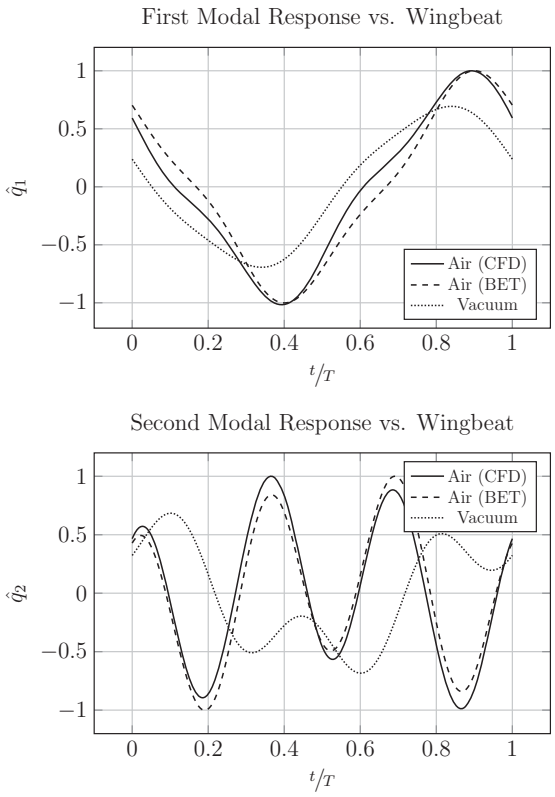

Fig. 11 First two modal responses for flapping in air and in vacuum. Each modal response is normalized with respect to the largest value of the in-air response.

Overall, inertial-elastic forces are larger than aerodynamic forces for the first vibration mode. Both force types oscillate primarily at ω with appreciable components at 3ω. The magnitude of the primary ω component of the inertial-elastic modal force is roughly 1.8 times greater than that of the aerodynamic force. Aerodynamic modal force Q_1 leads the first inertial-elastic modal force by a phase of approximately $\pi/4$. As a result, the two components interact constructively and the net modal force is larger than either of the individual parts. The 3ω magnitude is similar for both aerodynamic and inertial-elastic modal forces and again are out-of-phase by $\pi/4$.

For the second vibration mode, aerodynamic forces are larger than inertial-elastic forces. Again, both oscillate at ω with a harmonic at 3ω. The magnitude at ω is approximately 1.6 times larger for the aerodynamic force modal force Q_2 compared to the inertial-elastic force. The two forces are out of phase by nearly π. Consequently, the components interact destructively and the net second modal force is smaller in magnitude than the individual aerodynamic or inertial-elastic modal force. The magnitude at 3ω is approximately three times larger for aerodynamic modal force Q_2 compared to the inertial-elastic modal force. Despite that the net 3ω magnitude is small for the second modal force, this component is significant given its close proximity to the second natural frequency ($\omega_2 \approx 75$ Hz). We anticipate that this harmonic will dominate the second modal response due to a large gain factor.

Next, we calculate the first and second modal responses for the flapping wing. We consider a wing flapping in air, where both inertial-elastic and aerodynamic forces contribute to deformation, and a wing flapping in vacuum, where only inertial-elastic forces are present. We use both BET and CFD fluid models for the in-air case. This simulation complements the experimental work described in the introduction, where *M. sexta* wings were flapped in air and in reduced-density mediums. The notable exception is that we are able to simulate two rotational degrees-of-freedom, whereas these experiments only flapped the wing about the roll axis. We compare the modal responses rather than a physical response (e.g., wingtip deflection), so we can more accurately capture the full-field structural response. Comparing the response of a single point in air and in vacuum can be misleading. Even if that point behaves similarly, other points on the structure may respond differently in the two mediums. We solve the first two modal responses for flapping in air and in vacuum numerically. To verify the accuracy of our numerical results, we developed a closed-form approximate analytic solution (Appendix). The approximate analytic solution agrees well with numerical findings. Numerical results are plotted in Fig. 11, where each modal response is normalized by the largest value in air.

Perhaps most importantly, we see aerodynamic forces contribute significantly to the modal responses and by extension to the wing deformation. This contradicts the findings of Ref. [4], which suggest wing deformation is primarily a function of inertial-elastic forcing. We acknowledge that their work considered only SDOF roll rotation; for SDOF rotation, it is possible that the balance of inertial-elastic and aerodynamic forces is different. However, it is plausible that for SDOF rotation, the contribution of fluid loading to structural deformation would be larger than if a wing was subject to nominal multi-degrees-of-freedom (MDOF) kinematics. If a wing is subject to SDOF rotation, the induced flow is always normal to the wing over the entire flapping cycle. This creates a large pressure over the wing surface. For the MDOF kinematics considered in this work, the wing crosses its mean position oriented at its maximum pitch angle. The wing will be more streamlined with the flow, and as a result, the net fluid load on the wing is less than in

the SDOF case. We conjecture that even for the SDOF case, fluid loading nontrivially affects wing deformation. Indeed, a quick SDOF numerical simulation using the BET fluid model suggests that the first modal response is 25% larger in air than in vacuum.

We now turn our attention to the specific differences between in-air and in-vacuum flapping. In this comparison, we consider only the CFD fluid model. For the first mode, we see the overall peak-to-peak magnitude of the response is roughly 35% smaller in-vacuum than in-air. Like the first modal forces (Fig. 10), the first modal response occurs at the driving frequency and three times the driving frequency. Response magnitude at ω is approximately 1.4 times larger in air than in vacuum. Response magnitude at 3ω is approximately three times larger in air than in vacuum. The phase of the ω and 3ω components is similar in air and in vacuum. While the first modal response q_1 is somewhat similar in air and in vacuum, differences in the second modal response q_2 in air and in vacuum are more distinct. The in-air second modal response occurs primarily at 3ω with a lesser component at ω. The opposite is true for the in-vacuum q_2 response, where the oscillation occurs primarily at ω with a lesser component at 3ω. These trends can be explained by the second modal forces. As indicated by Fig. 10, the second aerodynamic modal response Q_2 has an appreciable component at 3ω. Because the second natural frequency occurs very close to 3ω, this modest 3ω component of Q_2 dominates the response. The second inertial-elastic modal force also has a 3ω component; however, it is smaller than that of Q_2. Thus, the in-vacuum response of q_2 is dominated by the ω component of the inertial-elastic modal force. Lastly, we note that the phase of oscillation of q_2 is quite different in air and in vacuum. The phase difference between in-air and in-vacuum flapping is nearly π at both ω and 3ω response components.

Lastly, Fig. 11 shows that the in-air first and second modal responses predicted via BET and CFD are similar. The agreement is particularly good for the first vibration mode, since the inertial-elastic modal force is larger than the aerodynamic modal forces predicted by either fluid model (Fig. 10). Agreement between the second modal responses is also fairly good, though BET predicts a slightly larger ω response than CFD. Overall, this comparison further illustrates BET's ability to estimate structural deformation with low computational demands.

4 Discussion

Here, we discuss some of the findings of our study and how they are relevant to biological and artificial flapping wing flight. First, we concede that BET is an imperfect method. The formulations most common to flapping wing literature are not well suited to treat dynamic phenomena such as flow separation, wing-wake interactions, or vortex shedding, all of which are observed in some biological fliers [30]. While some researchers have included rotational correction factors into BET formulations [21], we were unable to improve our predictions of aerodynamic modal forces by doing so. Nonetheless, BET with added mass captures some critical aerodynamic loading features required to inform FSI models. This renders BET a powerful tool for parametric design of FWMAV wings. Designers can leverage the framework to identify solution trends and to tailor flapping kinematics, wing mass/stiffness distributions, and geometry. Of course, it is sensible to verify model findings using a higher-fidelity fluid model such as CFD, particularly if unsteady dynamic phenomena are anticipated to play a role in the dynamics. BET should be used primarily to move design solutions into the proximity of an optimal solution and to reduce the parameter design space.

Next, we turn our attention to the physics governing wing deformation. Prior to this work, the relative contribution of inertial-elastic and aerodynamic forces to wing deformation at moth scale was unknown. We believe that both aerodynamic and inertial-elastic forces are on the same order-of-magnitude and as a result, contribute to wing deformation similarly. However, different forces appear to govern different modes of deformation. For example, inertial-elastic forces are somewhat larger for the bending mode whereas aerodynamic forces are modestly larger for the torsional mode. The implications of different force types governing different modes of deformation may be important.

More evolved insects, such as true flies and bees, have a small club-like appendage called a haltere that devolved from their hindwings [44]. The haltere is a gyroscopic organ that enables insects to identify their angular rates of rotation. Halteres generally sit in clefts between the insect abdomen and thorax and are consequently shielded from aerodynamic forces; haltere dynamics are governed almost entirely by inertia. This decoupling of aerodynamic and inertial-elastic forces is believed to be essential for proper haltere function. How do insects who lack halteres, such as moths and butterflies, receive analogous angular rate feedback? Researchers believe that this feedback stems from deforming mechanoreceptors in the forewing. However, it is unclear how such insects decouple inertial forces from aerodynamic forces. If inertial forces govern some modes of deformation and aerodynamic forces govern others, it may be possible to decouple these force types via careful placement and orientation of mechanoreceptors. Indeed, the campaniform sensilla in insect wings are directionally sensitive and distributed widely over the wing. It is possible that their placement and orientation allow for independent sensing of exogenous forces and internal states, thereby allowing the wing to behave as a large, flexible gyroscope.

However, we acknowledge that our findings were derived assuming unilateral coupling between the fluid and the structure. In practice, wing deformation may be large in some contexts and can indeed influence the surrounding flow field. For our model, if we determine the displacement at all nodes, take the absolute values, and then average them spatially, the maximum "average" time-varying displacement is about 1.2 cm at steady-state, which may considerably affect the flow field. For biological fliers, Nakata and Liu estimated via computational methods that wing flexibility increased peak vertical forces in hovering hawkmoths by approximately 22% [45]. This indicates a change in the flow field as a result of wing deformation. On the other hand, Du and Sun found that for hoverflies, some flow characteristics were insensitive to wing deformation and that flexibility increased averaged lift by only 10% [6]. In this case, it is plausible that the flow field is only modestly affected by deformation and that unilateral coupling between fluid and structure is better justified. Consequently, fluid–structure coupling assumptions must be accounted for on a case-by-case basis, though some dynamic phenomena such as aerodynamic damping will inevitable be absent from a unilaterally coupled model. The unilaterally coupled model detailed in this work can be used in part to identify where bilateral coupling may be required.

5 Conclusion

Flapping insect wings deform under both aerodynamic and inertial-elastic forces. However, the FSI that governs wing deformation is not well understood. This is in part because conventional FSI models are very high order. To gain a better understanding of the physics governing flapping wing deformation, we developed a novel FSI framework that is (1) reduced-order in the structural domain, (2) capable of accommodating arbitrary wing geometry, (3) able to consider any fluid loading model, and (4) suitable for describing unilateral or bilateral fluid–structure coupling. We apply this framework to study the FSI of a simulated hawkmoth wing. Through this simulation, we assess the accuracy of a low-order BET fluid model and its applicability to FSI problems. Moreover, we identify the relative contributions of aerodynamic and inertial-elastic forces to wing deformation. Key findings are summarized as follows.

Overall, BET provides reasonable initial approximations of both net aerodynamic properties as well as aerodynamic modal forces.

Though BET lacks absolute quantitative accuracy, it is much more computationally efficient relative to conventional fluid modeling approaches. For the simulations carried out in this work, BET estimated aerodynamic modal forces five orders of magnitude faster than CFD. We found that for hovering flight kinematics, aerodynamic modal forces estimated via BET agreed fairly well both in magnitude and phase with those calculated via CFD. The largest error (≈50%) was in the magnitude of the primary frequency. We then addressed how well BET estimated aerodynamic modal forces for different flapping kinematics. We found that for small perturbations in rotation amplitude and phase, BET predicted modal forces fairly well. The agreement between CFD and BET began to break down for larger deviations from hovering flapping kinematics; however, these exaggerated cases are generally not characteristic of biological flight. We determined that inertial-elastic and aerodynamic modal forces are generally on the same order of magnitude and that inertial-elastic forces are larger for bending modes while aerodynamic forces are larger for torsional modes. However, additional efforts must be made to identify if bilateral fluid–structure coupling will significantly affect these findings.

To summarize, this novel FSI framework lays the foundation for optimal design of small flapping wing robotic vehicles and enables advanced studies in insect sensorimotor control. This work has demonstrated the feasibility of low-order flapping wing FSI models and has contributed to the understanding of the physics that govern insect wing deformation. Moving forward, we must consider other flight regimes such as forward flight and incorporate more realistic FEA models of insect wings.

Acknowledgment

This material is based upon work supported by the National Science Foundation (NSF) (Grant No. CBET-1855383; Funder ID: 10.13039/501100008982). Any opinions, findings, and conclusions or recommendations expressed in this material are those of the author(s) and do not necessarily reflect the views of the NSF.

Nomenclature

k = turbulent kinetic energy
r = spanwise position of the blade element
P = fluid pressure
W = out-of-plane elastic deformation
$\mathcal{A}$ = angle of attack
$\vec{V}$ = blade element velocity
q_k = kth modal response
u_i = ith component direction of the fluid velocity
Q_k = kth aerodynamic modal force
$c(r)$ = wing chord width
dm = differential mass element
dr = blade element differential length
$\vec{a}_k, \vec{b}_k$ = kth inertial force center vector
dS_w = blade element differential area
$x_{\text{LE}}, x_{\text{TE}}$ = wing leading/trailing edge
C_D, C_L = drag/lift coefficients
F_A, F_N = aerodynamic axial/normal forces
F_L, F_D = aerodynamic lift/drag forces
α = roll rotation
β = pitch rotation
γ = yaw rotation
μ = dynamic viscosity
μ_t = eddy (turbulent) viscosity
ρ_f = fluid density
τ = Reynolds stress tensor
ϕ_k = kth vibration mode
$\vec{\Omega}$ = angular velocity vector
ω_k = kth natural frequency

Appendix: Approximate Analytic Solution

We rely primarily on numerical techniques to solve the linear time-varying equation of motion described by Eq. (18). However, it is prudent to develop an approximate analytic solution to verify the accuracy of our numerical results. We use the harmonic balance method to determine the periodic, steady-state solution of Eq. (18). Note that because of the assumed periodicity, this method cannot identify (1) parametric resonances associated with the periodically varying stiffness or (2) system instability, which may arise if the stiffness coefficient averaged over a wingbeat is negative. The approximate analytic solution is derived as follows. We represent Eq. (18) in the form

$$\ddot{q} + g(t)q = f(t) \tag{A1}$$

where q is the kth modal response (subscript dropped for clarity), $g(t)$ is a general time-varying stiffness term, and $f(t)$ is a general modal force. Each term can be represented via a complex Fourier series such that

$$q(t) = \sum_{n=-\infty}^{\infty} Q_n e^{jn\omega t} \tag{A2}$$

$$f(t) = \sum_{k=-\infty}^{\infty} F_k e^{jk\omega t} \tag{A3}$$

$$g(t) = \sum_{m=-\infty}^{\infty} G_m e^{2jm\omega t} \tag{A4}$$

where Q_n, F_k, and G_m are complex Fourier coefficients. We assume the primary component of $g(t)$ varies at twice the flapping frequency ω. Coefficients F_k and G_k are known because the flapping kinematics are prescribed, and therefore, we must solve only for Q_n to characterize the response. We substitute the above Fourier series into Eq. (A1) and equate similar terms. This forms the linear algebra problem

$$\mathbf{A}(G_m)\vec{Q} = \vec{F} \tag{A5}$$

where $\mathbf{A}(G_m)$ is a square matrix containing known coefficients G_m. Then, $\vec{Q} = [Q_{-n} \cdots Q_{-1}, Q_0, Q_1 \cdots Q_n]^T$ and $\vec{F} = [F_{-k} \cdots F_{-1}, F_0, F_1 \cdots F_k]^T$. Equation (A5) can be readily be solved to determine the unknown modal response coefficients Q_n. Specific to our problem, we assume a three-term Fourier expansion of the modal response, modal force, and stiffness. We consider the flapping kinematics shown in Table 3 and assume the flapping to occur in air. We solve Eq. (18) both numerically and via our approximate method. The comparison between solutions for the first and second modal responses is shown in Fig. 12. Overall, the agreement

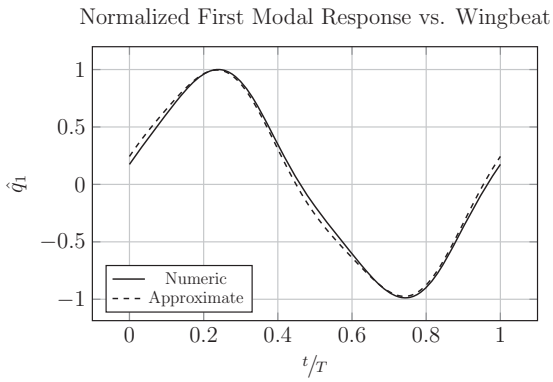

Fig. 12 Comparison between the approximate analytic solution and the numeric solution for the first modal response

is quite good, both in terms of magnitude and phase. The modest difference can be reconciled by assuming a higher-order Fourier expansion; however, harmonics greater than 5ω are very small for all modal forces observed for hovering flight kinematics.

References

[1] Trimmer, W. S., 1989, "Microrobots and Micromechanical Systems," Sens. Actuators, **19**(3), pp. 267–287.
[2] Fuller, S. B., Karpelson, M., Censi, A., Ma, K. Y., and Wood, R. J., 2014, "Controlling Free Flight of a Robotic Fly Using An Onboard Vision Sensor Inspired by Insect Ocelli," J. R. Soc. Interface, **11**(97), p. 20140281.
[3] Wood, R. J., 2008, "The First Takeoff of a Biologically Inspired At-Scale Robotic Insect," IEEE Trans. Robot., **24**(2), pp. 341–347.
[4] Combes, S. A., and Daniel, T. L., 2003, "Into Thin Air: Contributions of Aerodynamic and Inertial-Elastic Forces to Wing Bending in the Hawkmoth Manduca Sexta," J. Exp. Biol., **206**(17), pp. 2999–3006.
[5] Young, J., Walker, S. M., Bomphrey, R. J., Taylor, G. K., and Thomas, A. L., 2009, "Details of Insect Wing Design and Deformation Enhance Aerodynamic Function and Flight Efficiency," Science, **325**(5947), pp. 1549–1552.
[6] Du, G., and Sun, M., 2010, "Effects of Wing Deformation on Aerodynamic Forces in Hovering Hoverflies," J. Exp. Biol., **213**(13), pp. 2273–2283.
[7] Jankauski, M., Guo, Z., and Shen, I., 2018, "The Effect of Structural Deformation on Flapping Wing Energetics," J. Sound. Vib., **429**, pp. 176–192.
[8] Dickerson, B. H., Aldworth, Z. N., and Daniel, T. L., 2014, "Control of Moth Flight Posture is Mediated By Wing Mechanosensory Feedback," J. Exp. Biol., **217**(13), pp. 2301–2308.
[9] Fu, J., Liu, X., Shyy, W., and Qiu, H., 2018, "Effects of Flexibility and Aspect Ratio on the Aerodynamic Performance of Flapping Wings," Bioinspir. Biomim., **13**(3), p. 036001.
[10] Dickinson, M. H., and Tu, M. S., 1997, "The Function of Dipteran Flight Muscle," Comp. Biochem. Physiol. A, **116**(3), pp. 223–238.
[11] Tuthill, J. C., and Wilson, R. I., 2016, "Mechanosensation and Adaptive Motor Control in Insects," Curr. Biol., **26**(20), p. R1022.
[12] Norris, A. G., 2013, "Experimental Characterization of the Structural Dynamics and Aero-Structural Sensitivity of a Hawkmoth Wing Toward the Development of Design Rules for Flapping-Wing Micro Air Vehicles," Air Force Institute of Technology, Technical Report.
[13] Fairuz, Z., Abdullah, M., Yusoff, H., and Abdullah, M., 2013, "Fluid Structure Interaction of Unsteady Aerodynamics of Flapping Wing At Low Reynolds Number," Eng. Appl. Comput. Fluid Mech., **7**(1), pp. 144–158.
[14] Ishihara, D., Horie, T., and Denda, M., 2009, "A Two-Dimensional Computational Study on the Fluid–Structure Interaction Cause of Wing Pitch Changes in Dipteran Flapping Flight," J. Exp. Biol., **212**(1), pp. 1–10.
[15] Nakata, T., and Liu, H., 2012, "Aerodynamic Performance of a Hovering Hawkmoth With Flexible Wings: A Computational Approach," Proc. R. Soc. B, **279**(1729), pp. 722–731.
[16] Pfeiffer, A. T., Lee, J.-S., Han, J.-H., and Baier, H., 2010, "Ornithopter Flight Simulation Based on Flexible Multi-Body Dynamics," J. Bionic Eng., **7**(1), pp. 102–111.
[17] Jankauski, M., and Shen, I., 2014, "Dynamic Modeling of an Insect Wing Subject to Three-Dimensional Rotation," Int. J. Micro Air Veh., **6**(4), pp. 231–251.
[18] Sane, S. P., and Dickinson, M. H., 2002, "The Aerodynamic Effects of Wing Rotation and a Revised Quasi-Steady Model of Flapping Flight," J. Exp. Biol., **205**(8), pp. 1087–1096.
[19] Dickinson, M. H., Lehmann, F.-O., and Sane, S. P., 1999, "Wing Rotation and the Aerodynamic Basis of Insect Flight," Science, **284**(5422), pp. 1954–1960.
[20] Truong, Q., Nguyen, Q., Truong, V., Park, H., Byun, D., and Goo, N., 2011, "A Modified Blade Element Theory for Estimation of Forces Generated By a Beetle-Mimicking Flapping Wing System," Bioinspir. Biomim., **6**(3), p. 036008.
[21] Berman, G. J., and Wang, Z. J., 2007, "Energy-Minimizing Kinematics in Hovering Insect Flight," J. Fluid Mech., **582**, pp. 153–168.
[22] Jankauski, M., Daniel, T., and Shen, I., 2017, "Asymmetries in Wing Inertial and Aerodynamic Torques Contribute to Steering in Flying Insects," Bioinspir. Biomim., **12**(4), p. 046001.
[23] Whitney, J. P., and Wood, R. J., 2010, "Aeromechanics of Passive Rotation in Flapping Flight," J. Fluid Mech., **660**, pp. 197–220.
[24] Wang, Q., Goosen, J., and van Keulen, F., 2017, "An Efficient Fluid–Structure Interaction Model for Optimizing Twistable Flapping Wings," J. Fluids Struct., **73**, pp. 82–99.
[25] Stanford, B., Kurdi, M., Beran, P., and McClung, A., 2012, "Shape, Structure, and Kinematic Parameterization of a Power-Optimal Hovering Wing," J. Aircraft, **49**(6), pp. 1687–1699.
[26] Suzuki, T., and Mahfuz, H., 2018, "Analysis of Large-Scale Ocean Current Turbine Blades Using Fluid–Structure Interaction and Blade Element Momentum Theory," Ships Offshore Struct., **13**(5), pp. 451–458.
[27] Johnson, W., 2013, *Rotorcraft Aeromechanics*, Vol. 36, Cambridge University Press, Cambridge.
[28] Norlin, J., and Järpner, C., 2012, "Fluid Structure Interaction on Wind Turbine Blades," Ph.D. thesis, Master's thesis in Solid and Structural Mechanics and Fluid Dynamics, Chalmers University of Technology, Gothenburg, Sweden.
[29] Bottasso, C. L., Bortolotti, P., Croce, A., and Gualdoni, F., 2016, "Integrated Aero-Structural Optimization of Wind Turbines," Multibody Syst. Dyn., **38**(4), pp. 317–344.
[30] Chin, D. D., and Lentink, D., 2016, "Flapping Wing Aerodynamics: From Insects to Vertebrates," J. Exp. Biol., **219**(7), pp. 920–932.
[31] Shyy, W., Aono, H., Chimakurthi, S. K., Trizila, P., Kang, C.-K., Cesnik, C. E., and Liu, H., 2010, "Recent Progress in Flapping Wing Aerodynamics and Aeroelasticity," Prog. Aerospace Sci., **46**(7), pp. 284–327.
[32] Sedov, L. I., Chu, C., Cohen, H., Seckler, B., and Gillis, J., 1965, "Two-Dimensional Problems in Hydrodynamics and Aerodynamics," Phys. Today, **18**(12), pp. 62–63.
[33] Zikanov, O., 2010, *Essential Computational Fluid Dynamics*, John Wiley & Sons, New York.
[34] Spalart, P., and Allmaras, S., 1992, "A One-Equation Turbulence Model for Aerodynamic Flows," 30th Aerospace Sciences Meeting and Exhibit, Reno, NV, Jan. 6–9, p. 439.
[35] Wilcox, D., 2002, *Turbulence Modeling for CFD*, 2nd ed., DCW Industries, Anaheim, CA.
[36] Hadzic, H., 2006, "Development and Application of Finite Volume Method for the Computation of Flows Around Moving Bodies on Unstructured, Overlapping Grids," Ph.D. thesis, Technische Universität Hamburg, Hamburg.
[37] Combes, S., and Daniel, T., 2003, "Flexural Stiffness in Insect Wings. II. Spatial Distribution and Dynamic Wing Bending," J. Exp. Biol., **206**(17), pp. 2989–2997.
[38] Sims, T. W., Palazotto, A. N., and Norris, A., 2010, "A Structural Dynamic Analysis of a Manduca Sexta Forewing," Int. J. Micro Air Veh., **2**(3), pp. 119–140.
[39] Willmott, A. P., and Ellington, C. P., 1997, "The Mechanics of Flight in the Hawkmoth Manduca Sexta. I. Kinematics of Hovering and Forward Flight," J. Exp. Biol., **200**(21), pp. 2705–2722.
[40] Platzer, M., and Jones, K., 2006, "Steady and Unsteady Aerodynamics," *Flow Phenomena in Nature*, Vol. 4, WIT Transactions on State-of-the-Art in Science and Engineering, WIT Press, Southampton, UK, pp. 531–541.
[41] Nakata, T., Liu, H., and Bomphrey, R. J., 2015, "A CFD-Informed Quasi-Steady Model of Flapping-Wing Aerodynamics," J. Fluid Mech., **783**, pp. 323–343.
[42] Pohly, J., Salmon, J., Bluman, J., Nedunchezian, K., and Kang, C.-K., 2018, "Quasi-Steady Versus Navier–Stokes Solutions of Flapping Wing Aerodynamics," Fluids, **3**(4), p. 81.
[43] Hedrick, T. L., and Daniel, T., 2006, "Flight Control in the Hawkmoth Manduca Sexta: The Inverse Problem of Hovering," J. Exp. Biol., **209**(16), pp. 3114–3130.
[44] Alexandra Yarger, J. F., 2016, "Dipteran Halteres: Perspectives on Function and Integration for a Unique Sensory Organ," Integr. Comp. Biol., **56**(5), pp. 865–876.
[45] Nakata, T., and Liu, H., 2011, "Aerodynamic Performance of a Hovering Hawkmoth With Flexible Wings: A Computational Approach," Proc. R. Soc. B: Biol. Sci., **279**(1729), pp. 722–731.

31

REDUCED-ORDER MODELING AND EXPERIMENTAL STUDIES OF BILATERALLY COUPLED FLUID-STRUCTURE INTERACTION IN SINGLE-DEGREE-OF-FREEDOM FLAPPING WINGS

Contribution of Authors and Co-Authors

Manuscript in following chapter

Author: [Ryan Schwab]

Contributions: [Assisted in experimental work, Assisted in assessment of pertinent physics of reduced order model, Dissemination of work at Society of Integrative & Comparative Biology conference]

Author: [Heidi Reid]

Contributions: [Experimental work]

Author: [Mark Jankauski]

Contributions: [Development of reduced order modeling techniques]

Manuscript Information

[R. Schwab, H.Reid, M. Jankauski]

[Journal of Vibrations and Acoustics]

Status of Manuscript:
____ Prepared for submission to a peer-reviewed journal
____ Officially submitted to a peer-reviewed journal
____ Accepted by a peer-reviewed journal
_X_ Published in a peer-reviewed journal

[ASME]
[April 2020]
[Volume 142, Issue 2]
[DOI: 10.1115/1.4044268]

Reduced-Order Modeling and Experimental Studies of Bilaterally Coupled Fluid–Structure Interaction in Single-Degree-of-Freedom Flapping Wings

Ryan K. Schwab[1]
Department of Mechanical and Industrial Engineering,
Montana State University,
Bozeman, MT 59717-3800
e-mail: ryan.schwab@montana.edu

Heidi E. Reid[1]
Department of Mechanical and Industrial Engineering,
Montana State University,
Bozeman, MT 59717-3800
e-mail: heidi.reid@montana.edu

Mark Jankauski[1,2]
Department of Mechanical and Industrial Engineering,
Montana State University,
Bozeman, MT 59717-3800
e-mail: mark.jankauski@montana.edu

Flapping wings deform under both aerodynamic and inertial forces. However, many flapping wing fluid–structure interaction (FSI) models require significant computational resources which limit their effectiveness for high-dimensional parametric studies. Here, we present a simple bilaterally coupled FSI model for a wing subject to single-degree-of-freedom (SDOF) flapping. The model is reduced-order and can be solved several orders of magnitude faster than direct computational methods. To verify the model experimentally, we construct a SDOF rotation stage and measure basal strain of a flapping wing in-air and in-vacuum. Overall, the derived model estimates wing strain with good accuracy. In-vacuum, the wing has a large 3ω response when flapping at approximately one-third of its natural frequency due to a superharmonic resonance, where the superharmonic occurs due to the interaction of inertial forces and time-varying centrifugal softening. In-air, this 3ω response is attenuated significantly as a result of aerodynamic damping, whereas the primary ω response is increased due to aerodynamic loading. These results highlight the importance of (1) bilateral coupling between the fluid and structure, since unilaterally coupled approaches do not adequately describe deformation-induced aerodynamic damping and (2) time-varying stiffness, which generates superharmonics of the flapping frequency in the wing's dynamic response. The simple SDOF model and experimental study presented in this work demonstrate the potential for a reduced-order FSI model that considers both bilateral fluid–structure coupling and realistic multi-degrees-of-freedom flapping kinematics moving forward. [DOI: 10.1115/1.4045920]

Keywords: insect flight, flexible wings, reduced-order modeling, fluid–structure interaction, flapping wing micro air vehicles, aeroelasticity, flow-induced noise and vibration

1 Introduction

Flapping insect wings continue to inspire several emerging technologies, such as flapping wing micro air vehicles (FWMAVs) and elastic airfoil energy harvesting devices. FWMAVs are a robotic platform [1–3] that could enable low-cost remote sensing with unprecedented spatial resolution. Airfoil-based energy harvesters have the potential for highly efficient energy extraction from ambient flows [4–6] and could power the extensive sensor networks employed in many "Internet of Things" applications. However, the mathematical models necessary to design and optimize such technologies are often inefficient and require significant computational resources. As a result, many flapping wing models are challenged by the high-dimensional parametric studies essential for engineering design.

As an artificial or biological wing flaps, it deforms from both fluid and structural forces. This fluid–structure interaction (FSI) plays a critical role in flapping wing dynamics and has been studied extensively. Many flapping wing FSI models rely on direct computational methods, such as finite element analysis (FEA) coupled to computational fluid dynamics (CFD) [7–13]. However, both CFD and FEA require considerable computational resources to estimate flapping wing dynamics, and these inefficiencies are compounded when the two computational methods are coupled together. From the structural standpoint, large flapping rotations lead to periodic centrifugal forces that cause FEA stiffness matrices to become time-varying [14]. If direct FEA is used to calculate wing deformation, the stiffness matrix must be updated at each interval of analysis. The result is a huge number of degrees-of-freedom (DOFs), and the time required to evaluate the response of all DOFs is extensive. From the fluid standpoint, CFD must resolve the flow field over an entire control volume in order to estimate the pressure distribution over the wing surface [15]. This often requires solving several thousands of equations which makes CFD computationally intensive. To reduce the computational demand of the fluid dynamic solver, others have employed unsteady vortex lattice methods (UVLMs) to investigate flapping wing FSI [16,17]. Despite lower computation times compared to CFD, UVLM is a numerical method that requires considerable resources depending on the desired solution accuracy. Thus, direct computational methods are not well suited for efficient calculations of flapping wing FSI.

To reduce computational complexity, many researchers leverage quasi-static methods rooted in blade element theory (BET) [18–21].

[1]Authors contributed equally to the paper.
[2]Corresponding author.

Contributed by Technical Committee on Vibration and Sound of ASME for publication in the Journal of Vibration and Acoustics. Manuscript received September 20, 2019; final manuscript received December 30, 2019; published online January 8, 2020. Assoc. Editor: Izhak Bucher.

BET discretizes a wing into airfoils (blade elements) that run along the wing's chord. The elemental aerodynamic forces are estimated over each individual blade using 2D airfoil theory and are then integrated over the wing to calculate net aerodynamic forces. While this is an efficient method to estimate aerodynamics, BET is generally limited to rigid wings. It has been used only a handful of times to address the effects of wing flexibility. Wang et al. developed a flapping wing FSI model based upon BET, and assumed the wing's leading edge was rigid [22]. As a result, the model was best suited to estimate torsional deformation rather than bending deformation. Stanford et al. developed an FSI model that accounted for bending, however their structural solver required each *physical* DOF be solved for [23]—they did not leverage modal truncation to reduce the order of the structural model. Jankauski developed a reduced-order aeroelastic framework for flapping wings using modal truncation and BET, but this framework was used only to study one-way coupled FSI where the fluid was able to affect the structure but not vice versa [24]. It is possible that bilateral coupling between fluid and structure non-trivially affects flapping wing dynamics in some circumstances. While differences in unilateral and bilateral FSI models have not been studied extensively in flapping wings, bilateral FSI models of wind turbines predict stresses greater than those predicted by unilateral models [25]. Furthermore, in simplified cases such as a flexible plate in an ambient flow, bilateral FSI models predict physical phenomena missed entirely by unilateral models [26]. Based on these findings in other systems, bilateral coupling must be investigated more thoroughly in the context of flexible flapping wings.

Based upon this literature review, there remains a need for a reduced-order, bilaterally coupled FSI model for flapping, flexible wings. In this work, we develop this FSI model for a rectangular wing undergoing single-degree-of-freedom (SDOF) flapping. Though real insect wings have complex, three-dimensional rotational kinematics [27], these kinematics are challenging to replicate experimentally at high frequencies observed in insect flight. Further, multi-degrees-of-freedom (MDOF) kinematics give rise to complex fluid dynamic phenomena, such as rotational lift and damping [28]. Before formulating a reduced-order FSI model which considers MDOF kinematics, it is sensible to first develop and experimentally study a simpler SDOF model in order to demonstrate the feasibility of the approach. Moving forward, we will generalize this framework in order to account for the more complex flapping kinematics and flight conditions observed in real insects. The work presented here is a necessary first step toward accomplishing this goal.

The remainder of the paper is organized as follows. First, we derive the FSI model using the Lagrangian approach for the structural equation of motion (EoM) and BET for the fluid model. BET is a quasi-steady method which neglects unsteady fluid dynamic phenomena such as dynamic stall or vortex shedding. Next, we detail a simple SDOF flapping experiment used to verify our model both in-air and in-vacuum. We then compare experimental measurements to simulation results, and conclude with a discussion on how the fluid environment affects wing deformation. This paper extends the findings originally published in our ASME IDETC 2020 conference paper [29].

2 Theory

Here, we derive a reduced-order bilaterally coupled FSI model for flexible wings subject to SDOF flapping. We begin by determining the structural EoM via the Lagrangian method. We then identify aerodynamic forces and coupling through a BET approach. Aerodynamic terms are included in the EoM using the principle of virtual work.

2.1 Structural Model. The FSI framework in this section originated in Refs. [24,30] for a wing rotating in three dimensions, though these previous studies considered only unilateral fluid–structure coupling. We now consider SDOF rotation but with bilateral fluid–structure coupling. The model is summarized briefly to provide clarity to this paper. For a more thorough treatment, the reader is directed to these references.

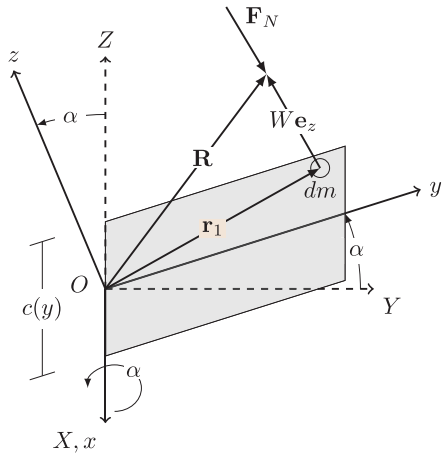

Fig. 1 Wing drawn in the rotating reference frame. Position vector R drawn from a fixed point of rotation *O* to an arbitrary differential mass element. F_N is the aerodynamic force acting normal to the wing surface.

We assume an inertial X–Y–Z coordinate frame undergoes a finite rotation about X with rotation amplitude α. The resulting x–y–z coordinate frame is bound to the rigid body rotation of the wing (Fig. 1) and has an angular velocity

$$\mathbf{\Omega} = \dot{\alpha}\,\mathbf{e}_x \tag{1}$$

In the rotating coordinate frame, we draw a position vector $\mathbf{R}$ from the fixed reference frame origin O to an arbitrary differential mass dm. Position vector $\mathbf{R}$ is

$$\mathbf{R} = \mathbf{r}_1 + W(\mathbf{r}_1, t)\mathbf{e}_z \tag{2}$$

where $\mathbf{r}_1$ describes the planar coordinates of dm with respect to the x–y–z frame (e.g., $\mathbf{r}_1 = x\,\mathbf{e}_x + y\,\mathbf{e}_y$) and $W(\mathbf{r}_1, t)$ is an infinitesimal out-of-plane deflection dependent on both space and time. In-plane deformation is neglected. The velocity of dm is

$$\dot{\mathbf{R}} = \mathbf{\Omega} \times \mathbf{R} + \dot{W}\mathbf{e}_z \tag{3}$$

Note that $\mathbf{e}_z$ is constant with respect to the x–y–z terminal frame and therefore has a time derivative of zero. Then, deflection $W(\mathbf{r}_1, t)$ is expanded as

$$W(\mathbf{r}_1, t) = \sum_{k=1}^{\infty} \phi_k(\mathbf{r}_1) q_k(t) \tag{4}$$

where ϕ_k is the kth mode shape and q_k is the kth modal response to be determined. We normalize ϕ_k with respect to the wing mass such that it satisfies orthonormal conditions. Finally, we determine the total kinetic and potential energies of the wing and use the Lagrangian approach to determine the EoM governing modal response q_k as

$$\ddot{q}_k + 2\zeta_k\omega_k\dot{q}_k + (\omega_k^2 - \dot{\alpha}^2)q_k = \ddot{\alpha}\int_m y\,\phi_k\,dm + Q_k \tag{5}$$

where ω_k is the wing's kth natural frequency, ζ_k is the damping ratio of the kth mode, and Q_k are non-conservative modal forces from aerodynamic loading. The explicit form of Q_k is detailed in

Sec. 2.2. Note that the modal damping term above does not explicitly appear in the derivation and is added after the undamped EoM is formulated.

Once modal responses q_k are known, physical quantities such as wing strain can easily be estimated. In this work, we measure wing strain rather than deformation to assess model accuracy. Physical strain is determined at $\mathbf{r}_1$ by

$$\epsilon(\mathbf{r}_1, t) = \sum_{k=1}^{\infty} \epsilon_k q_k \tag{6}$$

where ϵ_k is the modal strain.

2.2 Aerodynamic Modeling and Fluid–Structure Coupling. Now, we determine the aerodynamic modal force Q_k using a BET formulation. We assume the following:

(i) Unsteady fluid dynamic forces are negligible.
(ii) Drag is the only aerodynamic force that contributes to wing deformation because the induced fluid velocity is always normal to the wing's surface.
(iii) Inertial and aerodynamic forces do not vary along the wing chord and are assumed to act at the chord's centroid.
(iv) The displacement of each vibration mode retained does not vary with respect to the chord. This implies that the wing cannot exhibit a torsional response.

For the SDOF case considered here, these assumptions appear to be valid based on experimental findings presented later in this paper. When this FSI framework is generalized to consider MDOF flapping kinematics, however, these assumptions will need to be relaxed. Under these assumptions, the aerodynamic normal force per unit area $\mathbf{F}_N$ is

$$\mathbf{F}_N = -\frac{1}{2} C_D \rho_f \dot{\mathbf{R}} \cdot \dot{\mathbf{R}} \operatorname{sgn}(\dot{\mathbf{R}}) \mathbf{e}_z \tag{7}$$

where ρ_f is the density of air and C_D is an aerodynamic drag coefficient. The $\operatorname{sgn}(\dot{\mathbf{R}})$ ensures that the aerodynamic force is acting in the direction opposite to the instantaneous velocity at any point on the surface. Expanding $\mathbf{F}_N$ while neglecting small terms of $\mathcal{O}(W^2)$ or higher gives

$$\mathbf{F}_N = -\frac{1}{2} C \rho_f (2\dot{\alpha}\dot{W} y + \dot{\alpha}^2 y^2) \operatorname{sgn}(\dot{\mathbf{R}}) \mathbf{e}_z \tag{8}$$

where y is the spanwise component of $\mathbf{r}_1$ (Fig. 1) where $\mathbf{F}_N$ acts. Substituting the eigenfunction expansion of out-of-plane elastic deformation W gives

$$\mathbf{F}_N = -\frac{1}{2} C \rho_f \left[\sum_{k=1}^{\infty} (2\dot{\alpha}\dot{q}_k \phi_k y) + \dot{\alpha}^2 y^2 \right] \operatorname{sgn}(\dot{\mathbf{R}}) \mathbf{e}_z \tag{9}$$

Next, we project the physical aerodynamic force into the modal domain using the principle of virtual work [31]. The virtual work $\delta\mathcal{W}$ done by the kth modal force is

$$\delta\mathcal{W} = Q_k \delta q_k \tag{10}$$

where δq_k is a kth virtual modal response and Q_k is the nonconservative aerodynamic modal force corresponding to the kth vibration mode. Hereafter, quantities prefaced by δ refer to virtual quantities. More explicitly, the virtual work $\delta\mathcal{W}$ done by $\mathbf{F}_N$ is

$$\delta\mathcal{W} = \int_S \mathbf{F}_N \cdot \delta W \mathbf{e}_z \, dS \tag{11}$$

$$\delta\mathcal{W} = \int_S \mathbf{F}_N \cdot \sum_{k=1}^{\infty} \phi_k \delta q_k \mathbf{e}_z \, dS \tag{12}$$

where dS is the differential surface over which the aerodynamic force acts. Recognizing that dS is wing chord width $c(y)$ multiplied by differential length dy, we expand the above to

$$\delta\mathcal{W} = -\frac{1}{2} C \rho_f \left[\int_y \left(\sum_{r=1}^{\infty} (2\dot{\alpha}\dot{q}_r \phi_r y) + \dot{\alpha}^2 y^2 \right) c(y) dy \right] \sum_{k=1}^{\infty} \phi_k \delta q_k \operatorname{sgn}(\dot{\mathbf{R}}) \tag{13}$$

Note that we have included a second modal index r which contains the kth mode shape. Then, we equate the right-hand sides of Eqs. (10) and (13) and collect similar coefficients of δq_k to determine Q_k as

$$Q_k = \underbrace{-\frac{1}{2} C \rho_f \left[\dot{\alpha}^2 \int_y y^2 c(y) \phi_k \, dy \right]}_{Q_{A,k}} \underbrace{+ 2\dot{\alpha} \sum_{r=1}^{\infty} \int_y \dot{q}_r \phi_r \, \phi_k \, y \, c(y) \, dy \Bigg] \operatorname{sgn}(\dot{\mathbf{R}})}_{Q_{\zeta,k}} \tag{14}$$

The first term, $Q_{A,k}$, is an aerodynamic modal force term dependent only on time. $Q_{A,k}$ is required for both unilaterally and bilaterally coupled FSI models. We will refer to $Q_{A,k}$ as aerodynamic loading for the remainder of the paper. The second term, $Q_{\zeta,k}$, relies on coupling between the fluid and structure and is required only for bilateral fluid–structure coupling. It is a time-varying aerodynamic damping term that couples all vibration modes together and dissipates energy from wing vibration. Depending on the sign of $\dot{q}_k$ and $\operatorname{sgn}(\dot{\mathbf{R}})$, it is possible that $Q_{\zeta,k}$ appears as a negative damping term as well. In this case, $Q_{\zeta,k}$ may add energy to the system until it eventually grows unstable. Equation (14) is combined with Eq. (5) to give the total equation of motion governing modal response q_k.

3 Experiment

In this section, we describe a simple experiment designed to study our SDOF FSI model. We construct an SDOF rotation stage to prescribe flapping kinematics to a rectangular paper wing. Mode shapes and natural frequencies of the paper wing are estimated via FEA and are subsequently verified using a scanning vibrometer. During flapping experiments, we measure the spanwise strain at a point near the base of the wing using a uniaxial strain gage. We conduct flapping experiments both in-vacuum and in-air to verify the isolated structural and FSI models independently.

3.1 Rotation Stage. The SDOF rotation stage is pictured in Fig. 2, and a video of the stage during operation is included in the Supplementary Material on the ASME Digital Collection. All mounting brackets are 3D printed with FormLabs durable resin. A 60 W DC motor (Maxon Motors, 310007) drives the motion of the wing. The motor is equipped with an optical encoder that

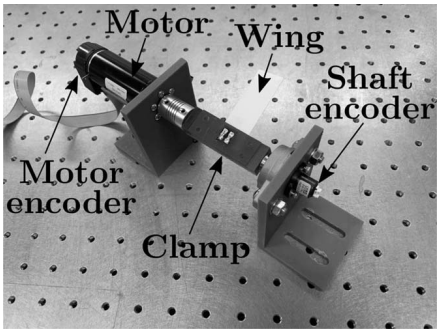

Fig. 2 Annotated motorized SDOF rotation stage used for FSI experiments

provides position feedback to a motor controller/driver (Maxon Motors, EPOS 24/5). The motor controller uses a proportional-integral-derivative framework to maintain prescribed flapping kinematics and minimize overshoot. All motion profiles are prescribed through a laptop computer running LabVIEW. In this work, we consider discrete flapping frequencies ranging from 5 to 15 Hz and a rotation amplitude of 45 deg. All rotations are sinusoidal. Each trial at a particular flapping frequency is conducted three times and the measurements from each trial are averaged in the frequency domain.

The motor connects to a wing clamp through a shaft coupler. The clamp secures the wing edge. A 350 ohm strain gage (Omega Engineering, GD-2/350-DY11) is adhered near the wing base. We use a National Instruments NI 9236 cDAQ module to provide excitation voltage to the gage as well as to record the temporal strain during experiments. The wing clamp is terminated with a low friction flange mount ball bearing. A female-end quantized analog encoder (US Digital, MAE3-A10-250-220-7-B) records the angular position of the terminated shaft end. The entire rotation stage is housed in an acrylic vacuum chamber (Sanatron, Fig. 3) capable of operating at pressures as low as 500 milliTorr. At this pressure, the medium density is roughly 0.05% of ambient air. All vacuum feed-through components are provided by Kurt J. Lesker company. The ability to conduct experiments in-vacuum allows us to evaluate the accuracy of the structural model prior to investigating the FSI model.

3.2 Experimental Paper Wing. We use a simple rectangular paper wing in all flapping experiments. The wing is made of thick card stock and is cut with a shear. All material and geometric properties of the wing and the strain gage mounted to the wing are shown in Table 1. We model the experimental wing in ABAQUS FEA to determine its natural frequencies and mode shapes. The FEA model assumes the wing is clamped at its base edge (Fig. 4) which implies no rotation or translation in this clamped region. We include the strain gage in the FEA model because it has a thickness on the same order of magnitude as that of paper. According to the manufacturer, the gage is composed primarily of polyimide film. As a result, the gage locally stiffens the wing in a way that cannot be neglected. The model is discretized into 250 elements, which we found was sufficient for convergence of the first natural frequency. For this work, we retain only a single vibration mode. Across the experimental parameters considered, higher-order modes had a negligible contribution to the wing's dynamic response. The first natural frequency predicted via FEA is $\omega_1 = 31.5$ Hz and corresponds to a bending mode (Fig. 6).

Next, we verify FEA-predicted mode shapes and natural frequencies experimentally. Because the wing is lightweight and has a large surface area, we measure these parameters in-air as well as in-vacuum to remove added mass effects. We secure the paper wing to a modal shaker (Modal Shop, K2007E007) using a metal clamp. The shaker excites the wing at its base via a linear swept sine signal ranging from 10 to 1000 Hz over 3.2 s. We measure basal excitation with a piezoelectric accelerometer (PCB Piezotronics, 352A21) and the response velocity of the wing at several points using a planar scanning vibrometer (Polytec PSV-400). We acquire data at 2.56 kHz, which results in a spectral resolution of 3200 FFT lines over the frequency range considered. We average the frequency response function over three trials at each measurement point to reduce spectral noise. The FRF averaged over the surface of the wing is shown in Fig. 5. Measured responses are reconstructed to identify the first vibration mode shape. This mode shape agrees well with that determined via FEA (Fig. 6). We then calculate the frequency response function averaged over the wing surface $G(\omega)$ and use FEMTools modal parameter extractor to estimate the first natural frequency and damping ratio from this averaged frequency response (Table 2).

Overall, the agreement between natural frequencies calculated via FEA ($\omega_1 = 31.5$ Hz) and measured experimentally ($\omega_1 = 30.2$ Hz) is good. We consider the natural frequency measured in-vacuum for this comparison. The discrepancy is likely due to uncertainty in Young's modulus of the paper wing. We assume a Young's modulus of 9.5 GPa for paper (Table 1), whereas reported

Table 1 Experimental wing properties

Variable	Description	Value	Unit
L_w	Wing unclamped length	5	cm
W_w	Wing width	2	cm
t_w	Wing thickness	0.17	mm
E_w	Wing Young's modulus	9.5	GPa
L_g	Gage length	5.65	mm
W_g	Gage width	6.35	mm
t_g	Gage thickness	0.13	mm
E_g	Gage Young's modulus	2.5	GPa
m	Total mass	0.21	g

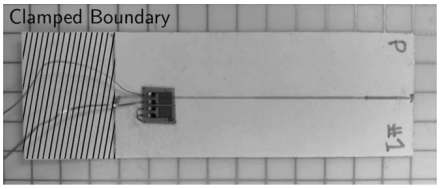

Fig. 4 Experimental paper wing on the gridded mat. Each grid box is 5 mm × 5 mm. Cross hatched area indicates clamped boundary condition.

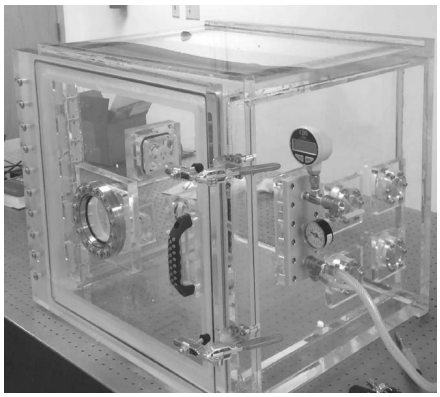

Fig. 3 Custom vacuum chamber used for testing. Chamber constructed by Sanatron LLC.

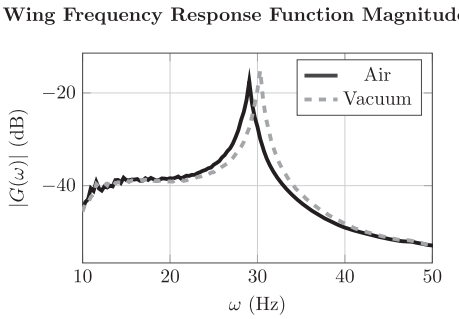

Fig. 5 Magnitude of wing frequency response function relating base acceleration to averaged output velocity

Table 2 Experimentally measured natural frequency and damping ratio for the first vibration mode of paper wing in-air and in-vacuum

	Air	Vacuum
Natural frequency ω_1	29.06 Hz	30.23 Hz
Damping ratio ζ_1	1.29%	0.89%

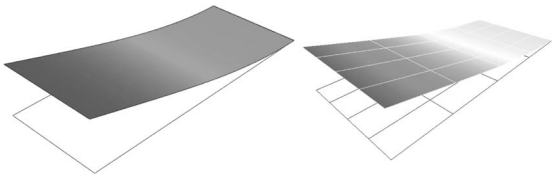

Fig. 6 First vibration mode shape of paper wing. (Left) Predicted via FEA and (right) measured experimentally.

values range between roughly 7 and 12 GPa [32]. To minimize the uncertainty in material properties, we use measured natural frequencies rather than those determined via FEA for all simulations that follow. This effectively adjusts Young's modulus of the FEA model to reconcile differences between it and the physical structure.

The natural frequency in-air is slightly lower than that measured in-vacuum due to the added mass. We also observe that the damping ratio is greater in-air, which suggests that aerodynamic damping may affect the structural response during flapping experiments. We found no notable differences between the mode shape measured in-air and in-vacuum. For the simulations that follow, we use experimentally measured natural frequencies and damping ratios rather than those determined via FEA.

4 Results

In this section, we compare model predictions to measurements taken from a wing flapping in-vacuum and in-air. We then use the FSI model to gain insight into the mechanisms responsible for wing deformation.

4.1 Model-Theory Comparison. We first evaluate the accuracy our structural model (Eq. (5)) without aerodynamics ($Q_k = 0$). We compare model predictions of strain to those measured from the wing flapping in-vacuum. Equation (5) is solved numerically over 50 periods (where each period is discretized into 100 uniform time-steps) to estimate the wing's modal response. We selected this temporal discretization such that the effective sampling frequency is 20 times greater than the fifth harmonic of the flapping frequency. Increasing the time-steps per period from 100 to 500 maximally affected peak wing strains by less than 0.5%, so we maintained the 100 time-steps per period in order to facilitate efficient parametric studies. We consider 100 evenly spaced flapping frequencies from 5 to 15 Hz, which is the same flapping frequency range considered in the experiment. Strain at the location of the gage is determined through Eq. (6). We calculate the Fourier transform of strain numerically and identify peak-to-peak magnitude at the driving frequency and each significant harmonic thereof. Across the range of flap frequencies ω considered, we observe appreciable response components at ω and 3ω. We see a large 5ω response for flapping frequencies between 5 and 7 Hz, however we do not focus on these responses here given that most insects flap at 30% or higher of their wing's first natural frequency [33].

Then, the magnitude of ω and 3ω strain components as a function of flapping frequency ω is shown in Fig. 7. In general, the model predicts experimental findings fairly well. However, the predicted strain at ω is slightly higher than what is measured experimentally

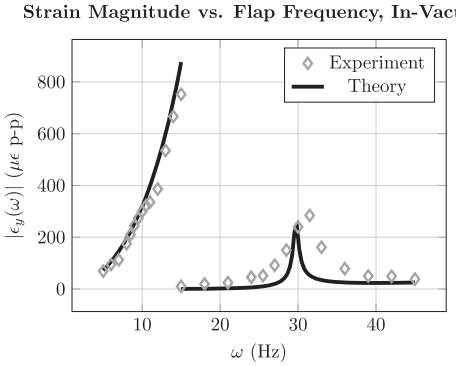

Fig. 7 Strain magnitude as a function of flapping frequency for in-vacuum flapping experiments. Each diamond represents the average of three 20-s flapping trials at a particular flapping frequency. Note that flapping frequencies range from 5 to 15 Hz and 3ω harmonics of the flapping frequency range from 15 to 30 Hz. Error bars for experimental strain measurements are of small magnitude ($\pm 3\mu\epsilon$ maximally) and are omitted from the figure for clarity.

(particularly when flapping frequencies exceed 10 Hz), and the peak 3ω response occurs at a lower frequency for the model than for the experiment. We conjecture these small discrepancies stem a weak hardening nonlinearity, which may occur in thin plates undergoing large displacements [34].

Note the significant 3ω response when $\omega = 10$ Hz. The strain response at 3ω has nearly the same magnitude as the primary ω response. For the model, the 3ω response is a result of the inertial force (which has frequency content only at ω) interacting with the time-varying wing stiffness (Eq. (5)). Because 3ω is near the fundamental frequency of the wing, the dynamic response at 3ω is large. Thus, even though the wing model is linear, the time-variance of the stiffness coefficient may still elicit superharmonic resonances [35].

Now that we have verified that the structural model predicts in vacuo dynamics with reasonable accuracy, we repeat the flapping experiment in air. We include the aerodynamic modal forces given by Eq. (14) into the EoM assuming the aerodynamic drag coefficient is $C = 3.0$ and the density of air is $\rho_f = 1.22$ kg/m^3. The aerodynamic drag coefficient and air density were not measured explicitly and are instead approximated from Refs. [19,32]. Please note that inaccuracies in these parameters may introduce systematic bias into the model, however potential errors appear to be small in the context of this work. All other parameters are identical to those presented for in vacuo simulations. FSI model predictions and experimental results are compared in Fig. 8. In general, the model-theory agreement is very good. We find the primary ω strain response increases modestly in air, while the 3ω strain response is substantially attenuated. We believe the increased ω response is due to aerodynamic loading, whereas the decreased 3ω response is due to aerodynamic damping. This is discussed in greater detail in Sec. 4.2.

In terms of computational efficiency, we are able to predict the response over a flapping cycle in about 50 ms with MATLAB's ODE45 solver. Unfortunately, we were unable to find any reported computation times of direct FSI methods for comparison. However, in the past we have used CFD to calculate pressure distributions over a rigid flapping wing [30]. Using an equivalent time-step and coarse surface mesh, it required approximately one hour per wingbeat to resolve to the flow field without considering fluid–structure coupling. Both computations are made using the same custom workstation with the following hardware: Intel Core i9-9900K Coffee Lake 8-Core, 16-Thread, 3.6 GHz processor, CORSAIR Vengeance LPX 32GB (2 × 16GB) 288-Pin DDR4 SDRAM, Gigabyte Z390 Aorus PRO WIFI LGA 1151 (300 Series) Intel Z390 HDMI SATA 6 Gb/s USB 3.1 ATX Intel

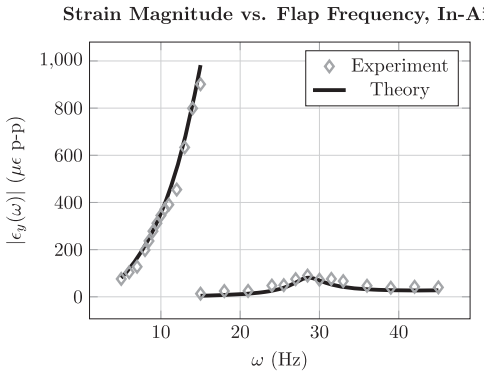

Fig. 8 Strain magnitude as a function of flapping frequency for in-air flapping experiments. Each diamond represents the average of three 20-s flapping trials at a particular flapping frequency. Note that flapping frequencies range from 5 to 15 Hz and 3ω harmonics of the flapping frequency range from 15 to 30 Hz. Error bars for experimental strain measurements are of small magnitude ($\pm 3\mu\epsilon$ maximally) and are omitted from the figure for clarity.

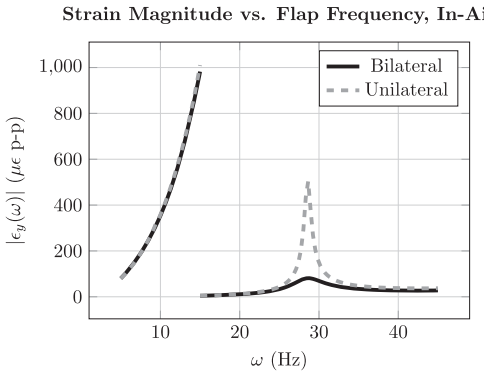

Fig. 9 Comparison of strain magnitude as a function of flapping frequency ω estimated by unilaterally and bilaterally coupled FSI models

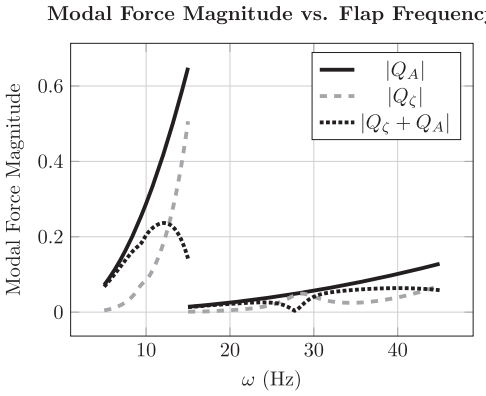

Fig. 10 Comparison of modal aerodynamic force magnitudes as a function of flap frequency ω. Note that modal force units are not physically meaningful and are excluded from the *y*-axis.

Motherboard, Seagate BarraCuda ST2000DM008 2TB 7200 RPM 256MB Cache SATA 6.0Gb/s 3.5″ Hard Drive, and Samsung 970 Evo PLUS 2TB Internal Solid State Drive. Based on these evaluation times, we estimate our new model predicts the wing response *at least* four orders of magnitude faster than direct FSI methods. In reality, the computational savings are likely much greater.

4.2 Unilateral Versus Bilateral Fluid–Structure Coupling. In Sec. 4.1, we observed a large 3ω dynamic response when the wing flapped at roughly one-third of its first natural frequency. The 3ω response was pronounced in vacuum but significantly attenuated in air. Here, we aim to identify the aerodynamic mechanism responsible for attenuating the 3ω response. There are two plausible explanations by which aerodynamics will reduce the 3ω response. The first mechanism is aerodynamic loading, Q_A, which does not rely on structural deformation. If Q_A has a 3ω component, it is possible that it will either constructively or destructively interfere with the in vacuo 3ω response depending on their relative phase. The second mechanism is through aerodynamic damping, Q_ζ, which relies on bilateral coupling of fluid and structure. This term is less straightforward to analyze because the structural response must be known in order to calculate it.

In order to identify which mechanism is responsible for attenuating the 3ω response in air, we simulate both unilaterally and bilaterally coupled FSI models. The unilateral model includes only aerodynamic loading, Q_A, whereas the bilateral model considers both aerodynamic loading Q_A and aerodynamic damping Q_ζ. We use the same parameters and flapping frequency that were used in previous simulations. Strain magnitude as a function of flap frequency for both unilateral and bilateral FSI models is shown in Fig. 9. Both the unilateral and bilateral FSI models suggest that aerodynamic loading Q_A increases the ω response magnitude relative to the in vacuo case. The unilateral model also predicts that strain magnitude at 3ω will approximately double from the in vacuo case as a result of aerodynamic loading, which is not consistent to what we observed experimentally. On the other hand, the bilateral FSI accurately predicts the experimentally measured 3ω response which suggests that aerodynamic damping Q_ζ is responsible for attenuating the 3ω response.

To explore this further, we calculate the magnitude of Q_A and Q_ζ individually, as well as their sum, as a function of ω (Fig. 10). Q_A has a nontrivial 3ω component that leads to the large 3ω response predicted by the unilateral FSI model in Fig. 9. In contrast, when Q_A and Q_ζ are considered together, their 3ω components interact destructively due to a difference in phase. When the wing is flapping at approximately one-third of its natural frequency, the net aerodynamic force has no 3ω component. We note that Q_ζ is dependent on the modal response and cannot be treated as a simple time-dependent input, and thus the coupling of the fluid and structure is ultimately what attenuates the 3ω component of the net aerodynamic force.

Additionally, Fig. 10 indicates that over the range of flapping frequencies considered, Q_A is always greater than Q_ζ and that the two forces interfere destructively. As a result, the magnitude of Q_A by itself is always greater than the magnitude of Q_A and Q_ζ summed together. At flapping frequencies of approximately 12 Hz and higher, Q_ζ grows faster than Q_A at ω. Consequently, the net aerodynamic forces at ω shrink as flapping frequencies exceed 12 Hz. The net aerodynamic forces at 3ω shrink as flapping frequencies exceed 13 Hz. However, it is difficult to see the reduction in aerodynamic loads at high frequency in the experimental results because inertial forces tend to dominate the structural response for the wing considered. Inertial forces increase monotonically with respect to flapping frequency, which implies wing deformation in general increases with flapping frequency despite reductions in aerodynamic forces.

5 Discussion

The two primary insights identified by our flapping FSI model and experiment are (1) a 3ω superharmonic resonance when the wing flaps at one-third of its natural frequency in vacuo, and

(2) significant attenuation of this superharmonic resonance in air due to aerodynamic damping. Superharmonic resonance and aerodynamic damping have been addressed using other analytic [36,37] and computational [38,39] FSI models, however we believe the framework presented here provides additional understanding into the mechanisms that underlie them.

The 3ω superharmonic resonance in flapping wings is often attributed to a weak cubic stiffness term in the wing's structural equation of motion [36,39]. Weak nonlinear cubic stiffness can generate odd harmonics for a system excited by a harmonic force at ω, and if one of these harmonics coincides with the system's resonant frequency, a superharmonic resonance occurs [40]. However, linear time-varying stiffness, a characteristic of flapping wings much less discussed in the literature, contributes to superharmonic resonance as well. Time-varying stiffness arises from centrifugal softening, where centrifugal softening relies on coupling between the flapping angular velocity and wing elastic deformation [14]. Physically, centrifugal softening implies the perceived stiffness of the wing is at a minimum as it passes its mid-stroke (maximum angular velocity) and at a maximum upon stroke reversal (zero angular velocity). Like a system with cubic stiffness, a system with linear time-varying stiffness excited at a single input frequency will exhibit a response at that input frequency and odd harmonics thereof. In the present work, the linear time-varying approximation yields good agreement between the experiment and theory which leads us to believe time-variance is primarily responsible for the superharmonic resonance observed here. Nonetheless, we saw secondary effects of strain hardening behavior during in vacuo experiments. In reality, it is likely that both time-variance and structural nonlinearity contribute to flapping wing dynamics—additional efforts must be made to identify under which conditions one is dominant over the other.

Our FSI model also provides an approximate expression for aerodynamic damping, which relies on the interplay of the wing's rotational velocity and structural deformation. Because wing kinematics are prescribed, the aerodynamic damping term is also linear and time-varying. Kang and Shyy utilized a similar linear time-varying analytic expression for aerodynamic damping, though the flapping kinematics considered in their study are different than those considered here [37]. In contrast to this linear time-varying form, Ramananarivo et al. employed a nonlinear aerodynamic damping model that does not rely on the wing's rigid body motion [36]. Despite the differences in the two models, both Kang and Ramananarivo found in their respective studies that aerodynamic damping caused a phase lag in the wing's structural response that was beneficial to aerodynamic thrust production. In the present study, we identify another critical function of aerodynamic damping: to attenuate superharmonic resonances. This may be important in the context of insect flight, where several insects flap around one-third the fundamental frequency of their wings [33]. While a modest 3ω wing response is thought to be beneficial to flapping wing flight in terms of energy efficiency [35] and aerodynamic performance [39], an extremely large 3ω resonant response would eventually compromise lift production or damage the wing. It is plausible that aerodynamic damping, which scales linearly with rotation amplitude according to our model, is responsible for maintaining beneficial deformation amplitudes at higher order harmonics of the flapping frequency. This must be further investigated via FSI models that can account for MDOF flapping kinematics.

6 Conclusion

Artificial and biological wings deform under both aerodynamic and inertial forces. This deformation is believed to play an important role in flight and has a notable effect on aerodynamic force production and energy efficiency. However, most flapping wing FSI models are high-order and require long solution times, which hinders their ability to carry out parameter studies efficiently. Lower-order models may employ assumptions that limit their accuracy, for example assuming unilateral coupling between fluid and structure.

Here, we formulate a reduced-order bilaterally coupled FSI model of a wing undergoing SDOF flapping. The structural model is derived via the Lagrangian approach and general fluid loading is accounted for via the principle of virtual work. We then estimate specific fluid forces using a quasi-steady BET approach. We find that the fluid forces can be represented as two terms: (1) a time-dependent fluid loading term that is a function only of rigid body flapping kinematics and (2) a fluid damping term that is a function both of the wing's rigid body motion and rate of elastic deformation. The fluid damping term effectively couples fluid and structure.

To study this model experimentally, we construct a mechanical flapper and measure the basal strain of a paper wing flapping at 45 deg with frequencies from 5 to 15 Hz. We initially flap the wing in-vacuo to benchmark the structural model. We find that when flapping at one-third the wing's natural frequency, the wing experiences a large superharmonic resonance. In air, this superharmonic response is attenuated substantially. Through simulation, we determine that aerodynamic damping is responsible for attenuating this superharmonic resonant response. The developed models predict the strain response magnitude with good accuracy for both in-air and in-vacuo experimental studies. In addition to its accuracy, the model is very efficient and can be solved in milliseconds.

However, the model and experiment here are limited to SDOF flapping. We also neglected unsteady fluid dynamic phenomena such as vortex shedding or flow separation. It is unclear if these assumptions will be justified in the context of real insect flight, where the wing structure and MDOF flapping kinematics are significantly more complex. Nonetheless, we have demonstrated here that a reduced-order, bilaterally coupled flapping wing FSI model performs well in a simplified case. This motivates possible extensions of this general modeling approach to consider more realistic flight conditions.

Acknowledgment

This research was supported by the National Science Foundation under Award No. CBET-1855383. Any opinions, findings, and conclusions or recommendations expressed in this material are those of the author(s) and do not necessarily reflect the views of the National Science Foundation. We would like to thank Sanatron LLC for providing us with the vacuum chamber used in our experiments.

References

[1] Shyy, W., Berg, M., and Ljungqvist, D., 1999, "Flapping and Flexible Wings for Biological and Micro Air Vehicles," Prog. Aerosp. Sci., **35**(5), pp. 455–505.
[2] Mueller, T. J., 2001, *Fixed and Flapping Wing Aerodynamics for Micro Air Vehicle Applications*, American Institute of Aeronautics and Astronautics, Reston, VA.
[3] Ellington, C. P., 1999, "The Novel Aerodynamics of Insect Flight: Applications to Micro-air Vehicles," J. Exp. Biol., **202**(23), pp. 3439–3448.
[4] Zhu, Q., and Peng, Z., 2009, "Mode Coupling and Flow Energy Harvesting by a Flapping Foil," Phys. Fluids, **21**(3), p. 033601.
[5] Zhu, Q., 2011, "Optimal Frequency for Flow Energy Harvesting of a Flapping Foil," J. Fluid Mech., **675**, pp. 495–517.
[6] Xiao, Q., and Zhu, Q., 2014, "A Review on Flow Energy Harvesters Based on Flapping Foils," J. Fluids Struct., **46**, pp. 174–191.
[7] Shyy, W., Aono, H., Chimakurthi, S. K., Trizila, P., Kang, C.-K., Cesnik, C. E., and Liu, H., 2010, "Recent Progress in Flapping Wing Aerodynamics and Aeroelasticity," Prog. Aerosp. Sci., **46**(7), pp. 284–327.
[8] Tian, F.-B., Dai, H., Luo, H., Doyle, J. F., and Rousseau, B., 2014, "Fluid–Structure Interaction Involving Large Deformations: 3d Simulations and Applications to Biological Systems," J. Comput. Phys., **258**, pp. 451–469.
[9] Hamamoto, M., Ohta, Y., Hara, K., and Hisada, T., 2007, "Application of Fluid–Structure Interaction Analysis to Flapping Flight of Insects with Deformable Wings," Adv. Robotics, **21**(1–2), pp. 1–21.
[10] Takizawa, K., Tezduyar, T. E., and Kostov, N., 2014, "Sequentially-Coupled Space–Time FSI Analysis of Bio-inspired Flapping-Wing Aerodynamics of An MAV," Comput. Mech., **54**(2), pp. 213–233.

[11] Nakata, T., and Liu, H., 2012, "A Fluid–Structure Interaction Model of Insect Flight With Flexible Wings," J. Comput. Phys., **231**(4), pp. 1822–1847.
[12] Shahzad, A., Tian, F.-B., Young, J., and Lai, J. C., 2018, "Effects of Flexibility on the Hovering Performance of Flapping Wings With Different Shapes and Aspect Ratios," J. Fluids Struct., **81**, pp. 69–96.
[13] Ishihara, D., Horie, T., and Denda, M., 2009, "A Two-Dimensional Computational Study on the Fluid–Structure Interaction Cause of Wing Pitch Changes in Dipteran Flapping Flight," J. Exp. Biol., **212**(1), pp. 1–10.
[14] Jankauski, M., and Shen, I., 2014, "Dynamic Modeling of An Insect Wing Subject to Three-Dimensional Rotation," Int. J. Micro Air Veh., **6**(4), pp. 231–251.
[15] Gresho, P. M., 1991, "Some Current CFD Issues Relevant to the Incompressible Navier–Stokes Equations," Comput. Methods Appl. Mech. Eng., **87**(2–3), pp. 201–252.
[16] Roccia, B. A., Preidikman, S., and Balachandran, B., 2017, "Computational Dynamics of Flapping Wings in Hover Flight: A Co-Simulation Strategy," AIAA J., **55**(6), pp. 1806–1822.
[17] Fitzgerald, T., Valdez, M., Vanella, M., Balaras, E., and Balachandran, B., 2011, "Flexible Flapping Systems: Computational Investigations Into Fluid–Structure Interactions," Aeronaut. J., **115**(1172), pp. 593–604.
[18] Sane, S. P., and Dickinson, M. H., 2002, "The Aerodynamic Effects of Wing Rotation and a Revised Quasi-Steady Model of Flapping Flight," J. Exp. Biol., **205**(8), pp. 1087–1096.
[19] Whitney, J. P., and Wood, R. J., 2010, "Aeromechanics of Passive Rotation in Flapping Flight," J. Fluid Mech., **660**, pp. 197–220.
[20] Jankauski, M., Daniel, T., and Shen, I., 2017, "Asymmetries in Wing Inertial and Aerodynamic Torques Contribute to Steering in Flying Insects," Bioinspiration Biomimetics, **12**(4), p. 046001.
[21] Berman, G. J., and Wang, Z. J., 2007, "Energy-Minimizing Kinematics in Hovering Insect Flight," J. Fluid Mech., **582**, pp. 153–168.
[22] Wang, Q., Goosen, J., and van Keulen, F., 2017, "An Efficient Fluid–Structure Interaction Model for Optimizing Twistable Flapping Wings," J. Fluids Struct., **73**, pp. 82–99.
[23] Stanford, B., Kurdi, M., Beran, P., and McClung, A., 2012, "Shape, Structure, and Kinematic Parameterization of a Power-Optimal Hovering Wing," J. Aircr., **49**(6), pp. 1687–1699.
[24] Jankauski, M. A., 2019, "Low-Order Aeroelastic Modeling of Flapping, Flexible Wings," ASME 2018 International Design Engineering Technical Conferences and Computers and Information in Engineering Conference, Quebec City, Canada, Aug. 26–29, 2018.
[25] Yi-Bao, C., Wang, Z.-K., and Tsai, G.-C., 2015, "Two-Way Fluid–Structure Interaction Simulation of a Micro Horizontal Axis Wind Turbine," Int. J. Eng. Technol. Innovation, **5**(1), p. 33.
[26] Benra, F.-K., Dohmen, H. J., Pei, J., Schuster, S., and Wan, B., 2011, "A Comparison of One-Way and Two-Way Coupling Methods for Numerical Analysis of Fluid–Structure Interactions," J. Appl. Math., **2011**, p. 853560.
[27] Willmott, A. P., and Ellington, C. P., 1997, "The Mechanics of Flight in the Hawkmoth Manduca Sexta. I. Kinematics of Hovering and Forward Flight," J. Exp. Biol., **200**(21), pp. 2705–2722.
[28] Walker, J. A., 2002, "Rotational Lift: Something Different Or More of the Same?," J. Exp. Biol., **205**(24), pp. 3783–3792.
[29] Schwab, R., Reid, H., and Jankauski, M., 2019, "Reduced-Order Modeling and Experimental Studies of Two-Way Coupled Fluid-Structure Interaction in flapping Wings," ASME 2019 International Design Engineering Technical Conferences and Computers and Information in Engineering Conference, Aug. 18-21, American Society of Mechanical Engineers Digital Collection, New York.
[30] Schwab, R., Johnson, E., and Jankauski, M., 2019, "A Novel Fluid–Structure Interaction Framework for Flapping, Flexible Wings," ASME J. Vib. Acoust., **141**(6), p. 061002.
[31] Rao, S. S., 2007, *Vibration of Continuous Systems*, Vol. 464, Wiley Online Library, New York.
[32] Baumeister, T., and Sadegh, A. M., 1978, *Marks' Standard Handbook for Mechanical Engineers*, Vol. 1, McGraw-Hill, New York.
[33] San Ha, N., Truong, Q. T., Goo, N. S., and Park, H. C., 2013, "Relationship Between Wingbeat Frequency and Resonant Frequency of the Wing in Insects," Bioinspiration Biomimetics, **8**(4), p. 046008.
[34] Malatkar, P., 2003, "Nonlinear Vibrations of Cantilever Beams and Plates," Ph.D. thesis, Virginia Tech.
[35] Jankauski, M., Guo, Z., and Shen, I., 2018, "The Effect of Structural Deformation on Flapping Wing Energetics," J. Sound Vib., **429**, pp. 176–192.
[36] Ramananarivo, S., Godoy-Diana, R., and Thiria, B., 2011, "Rather Than Resonance, Flapping Wing Flyers May Play on Aerodynamics to Improve Performance," Proc. Natl. Acad. Sci. U. S. A., **108**(15), pp. 5964–5969.
[37] Kang, C.-k., and Shyy, W., 2014, "Analytical Model for Instantaneous Lift and Shape Deformation of An Insect-Scale Flapping Wing in Hover," J. R. Soc. Interface, **11**(101), p. 20140933.
[38] Tang, J., Chimakurthi, S., Palacios, R., Cesnik, C., and Shyy, W., 2008," Computational Fluid–Structure Interaction of a Deformable Flapping Wing for Micro Air Vehicle Applications," 46th AIAA Aerospace Sciences Meeting and Exhibit, Reno, NV, Jan. 7–10, p. 615.
[39] Vanella, M., Fitzgerald, T., Preidikman, S., Balaras, E., and Balachandran, B., 2009, "Influence of Flexibility on the Aerodynamic Performance of a Hovering Wing," J. Exp. Biol., **212**(1), pp. 95–105.
[40] Kovacic, I., and Brennan, M. J., 2011, *The Duffing Equation: Nonlinear Oscillators and Their Behaviour*, John Wiley & Sons, Hoboken, NJ.

REDUCED-ORDER MODELING AND THE PHYSICS GOVERNING FLAPPING WING FLUID-STRUCTURE INTERACTION

Contribution of Authors and Co-Authors

Manuscript in following chapter

Author: [Ryan Schwab]

Contributions: [Integrated computational fluid dynamics and finite element analysis solvers into a high fidelity flapping wing model]

Author: [Erick Johnson]

Contributions: [Assistance with development of high fidelity model]

Author: [Mark Jankauski]

Contributions: [Development of reduced order model through blade element theory and modal truncation, Experimental study and motion tracking]

Manuscript Information

[R. Schwab, E. Johnson, M. Jankauski]

[bioRxiv]

Status of Manuscript:
_X_ Prepared for submission to a peer-reviewed journal
____ Officially submitted to a peer-reviewed journal
____ Accepted by a peer-reviewed journal
____ Published in a peer-reviewed journal

Reduced-Order Modeling and the Physics Governing Flapping Wing Fluid-Structure Interaction

Ryan Schwab, Erick Johnson and Mark Jankauski

Montana State University, Mechanical & Industrial Engineering, Bozeman, MT 59717

Engineering, theoretical Biology

Keywords:
Insect flight, fluid-structure interaction, flapping wings, reduced-order modeling

Author for correspondence:
Mark Jankauski
e-mail:
mark.jankauski@montana.edu

Flapping, flexible insect wings deform during flight from aerodynamic and inertial forces. This deformation is believed to enhance aerodynamic and energetic performance. However, the predictive models used to describe flapping wing fluid-structure interaction (FSI) often rely on high fidelity computational solvers such as computational fluid dynamics (CFD) and finite element analysis (FEA). Such models require lengthy solution times and may obscure the physical insights available to analytical models. In this work, we develop a reduced order model (ROM) of a wing experiencing single-degree-of-freedom flapping. The ROM is based on deformable blade element theory and the assumed mode method. We compare the ROM to a high-fidelity CFD/FEA model and a simple experiment comprised of a mechanical flapper actuating a paper wing. Across a range of flapping-to-natural frequency ratios relevant to flying insects, the ROM predicts wingtip deflection five orders of magnitude faster than the CFD/FEA model. Both models are resolved to predict wingtip deflection within 30% of experimentally measured values. The ROM is then used to identify how the physical forces acting on the wing scale relative to one another. We show that, in addition to inertial and aerodynamic forces, added mass and aerodynamic damping influence wing deformation nontrivially.

1. Introduction

Insects leverage flexible, flapping wings to realize flight. Unsteady aerodynamic forces generated by flapping wings allow insects to hover or advance forward [1], while aerodynamic and inertial asymmetries caused by differences in left-right flapping kinematics enable insects to perform complex aerial maneuvers [2]. Through a combination of experimental, analytical and numerical studies, tremendous progress has been made over the past several decades to characterize the aeromechanics of insect flight during hovering [3–5], climbing [6–8] and maneuvering [9–11]. More recently, the wing structure itself has garnered attention, where structural features such as venation, corrugation, and camber have been determined to augment aerodynamic performance [12–15].

During flight, insect wings deform under both aerodynamic and inertial-elastic forces [16]. The fluid and structural physics are tightly coupled, where aerodynamic forces influence how the wing deforms and resulting wing deformation influences the surrounding flow field. Computational methods, typically computational fluid dynamics (CFD) coupled to finite element analysis (FEA) based solvers, have been used to simultaneously resolve the instantaneous wing shape and surrounding flow field [12,17–24]. While direct computational methods can provide accurate estimates of flapping wing dynamics, they often require computational times on the order of hours to days to generate solutions. Both CFD and FEA face computational challenges, and their individual challenges are compounded when the two computational solvers are coupled together. CFD necessitates the Navier-Stokes equations be solved across a discretized fluid domain [25], which may result in tens of thousands of conditions that must be satisfied at each time interval of analysis. From the structural perspective, the large rotational kinematics of flapping wings give rise to centrifugal forces that periodically influence the wing's stiffness [26]. Centrifugal effects require that the FEA stiffness matrix be updated at each interval of analysis if the angular velocity is not constant. The high computational resources demanded by direct computational methods therefore render them unsuitable for parametric studies that consider variable wing geometry, kinematics or structural properties. Moreover, reliance on computational models may obscure the physical phenomena governing (e.g., aerodynamic drag, added mass, etc.) wing deformation.

In this regard, analytic models may be preferable to computational models because (1) they provide physical insights into flapping wing dynamics, and (2) in some cases, can identify response trends more quickly due to lower solution times. The most commonly used analytic models in flapping wing literature are based on quasi-steady blade element theory (BET) [27]. BET assumes that a wing can be discretized into chordwise strips (blade elements). Based on known flapping kinematics and measured or estimated aerodynamic coefficients, thin airfoil theory is used to predict aerodynamic forces and moments acting on a single blade element, and these differential forces are integrated over the wing surface to estimate total aerodynamic forces. BET is often restricted to describing the aerodynamics of rigid wings, though Wang et al. developed a fluid-structure interaction (FSI) model based on BET to estimate the aerodynamics of twistable wings [28]. Other researchers have used Theoderson's unsteady aerodynamic model to predict flapping forces of flapping wings [29–31]. Kodali et al. derived an analytical FSI model of a flexible pitching, plunging wing based on Theoderson's model. Their model predicted wingtip deflection with reasonable accuracy compared to experimental and numerical findings [32]. However, Theodorsen's model is based on inviscid assumptions, and may be limited in contexts where drag influences wing loading considerably; in these cases, BET may perform more favorably than Theoderson's model.

Based on this review, the first objective of this research is to develop a reduced-order FSI model of a flapping wing experiencing single-degree-of-freedom (SDOF) rotation. Aerodynamic drag is appreciable when the wing is undergoing SDOF rotation. The fluid model is based on BET, but because it permits elastic deformation, we refer to it as *deformable* blade element theory (DBET). The analytical model provides insights into the physics governing flexible wing

aerodynamics and expands upon the research in [33]. The second objective of this work is to validate the reduced-order model against experimental results as well as solutions generated via high-fidelity coupled CFD/FEA. This allows us to quantitatively compare accuracy and solution times achievable by both low and high-order models. While the SDOF flapping kinematics in this work are simplified from the multiple-degree-of-freedom (MDOF) wing kinematics of flying insects, this work is a foundational step towards reduced-order modeling of FSI in wings subject to more realistic motions.

The remainder of this manuscript is organized as follows. First, we derive the reduced-order FSI model based on DBET and the assumed mode method (AMM). Next, we detail the high-fidelity coupled CFD/FEA used to predict wing deformation. We then present a simple experiment to assess the accuracy of both models. We conclude by discussing insights gained from the DBET model and comment on its efficiency relative to the computational model.

2. Theory

Here, we present two models capable of resolving the deformation of a wing experiencing SDOF rotation. The first model is low-fidelity and semi-analytical, whereas the second model is high-fidelity and computational. The objective of this research is to compare the accuracy and computation times achievable by both models. Note that the following FSI frameworks are general and applicable to a range of wings and SDOF flapping kinematics; for this reason, the simulation parameters specific to experimental validation are presented in Section 3.

(a) Reduced-Order Modeling

The reduced-order FSI model is based upon AMM and DBET. The structural and aerodynamic drag models originated in [33], however this previous work did not compare the ROM to high-fidelity coupled CFD/FEA. This research further advances the previous ROM by incorporating added mass, which we show influences the wing's perceived stiffness and increases aerodynamic loading.

(i) Structural Model

The motion of a flapping wing can be modeled as a superposition of elastic deformation on top of larger rigid body rigid body rotation. Rigid body rotation is generally an active or controlled

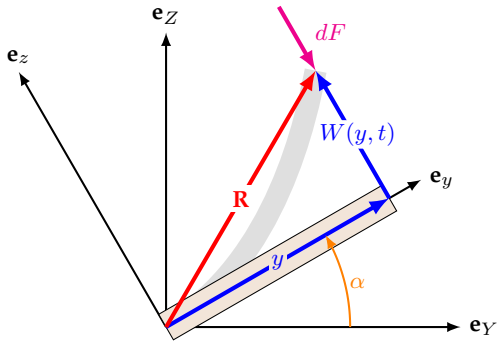

Figure 1. An xyz reference frame rotates with the rigid body rotation of the wing, where α denotes the wing's flap angle. Within the rotating reference frame, the wing experiences small out-of-plane deflection $W(y,t)$, where y is the axial location of a point on the wing. The wing is subject to an aerodynamic force per unit area dF. Gray region shows a deformed state of the wing.

degree-of-freedom, whereas elastic deformation occurs passively under internal and external forces. Provided elastic deformation is small, it can be treated as a summation of vibration mode shapes multiplied by their modal responses, also called modal participation factors. The benefit to formulating the structural model in terms of modal coordinates instead of physical coordinates is that the wing's mode shapes are independent of dynamic inputs. They can be pre-computed prior to dynamic simulation based on knowledge of the structure alone. Further, we can truncate higher modes that do not contribute meaningfully to wing deformation (e.g., modes that correspond to natural frequencies substantially outside of the range of input frequencies), which reduces the computational time required to solve the structural model.

We establish a reference frame that rotates with the rigid body rotation of the wing (Fig. 1). An inertial XYZ coordinate system undergoes a rotation of magnitude α, where α is the wing's flapping angle. The resulting xyz coordinate system has an angular velocity $\boldsymbol{\Omega}$, where

$$\boldsymbol{\Omega} = \dot{\alpha}\mathbf{e}_x \tag{2.1}$$

where $\dot{}$ denotes a derivative with respect to time and $\mathbf{e}_n$ denotes a unit vector in the n direction. Within the xyz frame, we draw a position vector $\mathbf{R}$ from a fixed point of rotation to a differential mass element dm (Fig. 1), where

$$\mathbf{R} = y\mathbf{e}_y + W(y,t)\mathbf{e}_z \tag{2.2}$$

Above, y denotes the planar coordinates of the differential mass and $W(y,t)$ describes and a small out-of-plane elastic deformation. In-plane deformation and twisting about the y axis are neglected. The out-of-plane deformation can be expanded via the separation principle such that

$$W(y,t) = \sum_{k=1}^{\infty} \phi_k(y) q_k(t) \tag{2.3}$$

where $\phi_k(y)$ is the wing's k^{th} mode shape normalized with respect to the wing's mass and q_k is the corresponding time-dependence, or modal participation factor to be determined. $\phi_k(y)$ is a static quantity and can be determined either via modal analysis in FEA or analytically for simple structures. The velocity $\dot{\mathbf{R}}$ of the differential mass is

$$\dot{\mathbf{R}} = \boldsymbol{\Omega} \times \mathbf{R} + \dot{\mathbf{R}}_{xyz} \tag{2.4}$$

where $\dot{\mathbf{R}}_{xyz}$ is the differential mass velocity referenced from the rotating frame. The kinetic energy T of the entire wing is

$$T = \frac{1}{2}\int_m \dot{\mathbf{R}} \cdot \dot{\mathbf{R}}\, dm \tag{2.5}$$

which can be represented in modal coordinates as

$$T = \frac{1}{2}\left[\dot{\alpha}^2\left(Ixx + \sum_{k=1}^{\infty} q_k^2\right) + \dot{\alpha}\sum_{k=1}^{\infty}\left(2\lambda_k q_k + \dot{q}_k^2\right)\right] \tag{2.6}$$

where I_{xx} is the wing moment of inertia about x and λ_k is an inertial constant defined by $\lambda_k = \int_m y\phi_k\, dm$. The wing's potential energy U is

$$U = \int_V \mathcal{S}(W,W)\, dV \tag{2.7}$$

where $\mathcal{S}$ is a symmetric, quadratic strain energy density function and V is the wing's volume. By applying Lagrange's equation, we arrive at the equation governing modal response q_k as

$$\ddot{q}_k + (\omega_k^2 - \dot{\alpha}^2)q_k = -\ddot{\alpha}\lambda_k + Q_k \tag{2.8}$$

where ω_k is the wing's k^{th} natural frequency *in vacuo* and Q_k includes all non-conservative modal forces to be determined. The above equation is linear and time-varying, where the wing stiffness

is influenced by its angular rate of rotation through a phenomena called centrifugal softening. Lastly, a general physical force $d\mathbf{F}$ per unit area is converted to the k^{th} modal force by

$$Q_k = \int_S (d\mathbf{F} \cdot \phi_k \mathbf{e}_z)\, dS \tag{2.9}$$

where S is the surface over which the force acts. In the following sections, we determine the modal forces Q_k associated with aerodynamic drag and added mass via DBET.

(ii) Aerodynamic Drag

Due to simplified SDOF flapping kinematics, the wing will produce negligible lift and drag becomes the dominant aerodynamic force. Assuming drag acts only in the z direction and does not vary over the wing's chord, the drag per unit area is $d\mathbf{F}_D$ is

$$d\mathbf{F}_D = -\frac{1}{2} C_D \rho_f (\dot{\mathbf{R}} \cdot \mathbf{e}_z)^2 \operatorname{sgn}(\dot{\mathbf{R}})\, \mathbf{e}_z \tag{2.10}$$

where C_D is an empirical drag coefficient and ρ_f is fluid density. C_D typically varies with respect to the wing's angle of attack, but in this case can be treated as a constant since the wing's angle of attack is always $\pi/2$ or $3\pi/2$ because in a static fluid air is only moved normal to the wing surface. Expanding this expression in terms of $\dot{\mathbf{R}}$ and the expansion in Eq. 2.3 gives

$$d\mathbf{F}_D = -\frac{1}{2} C_D \rho_f \left[\dot{\alpha}^2 y^2 + 2\dot{\alpha} y \sum_{k=1}^{\infty} \dot{q}_k \phi_k \right] \operatorname{sgn}(\dot{\mathbf{R}})\, \mathbf{e}_z + \mathcal{O}(W^2) \tag{2.11}$$

where we neglect terms of $\mathcal{O}(W)^2$ because deformation is small. Projecting the physical drag force into the modal domain via Eq. 2.9 yields two modal force terms. The first modal force term is

$$Q_{D,k} = -\frac{1}{2} C_D \rho_f \dot{\alpha}^2 \Gamma_k \operatorname{sgn}(\dot{\mathbf{R}}) \tag{2.12}$$

where Γ_k is a constant defined by $\Gamma_k = \int_y b(y) y^2 \phi_k\, dy$ and $b(y)$ is the wing chord. $Q_{D,k}$ depends only on the rigid body rotation of the wing and is not significantly affected (besides the sgn term) by elastic deformation. We therefore refer to $Q_{D,k}$ as rigid body drag. The second modal force term is

$$Q_{\zeta,k} = C_D \rho_f \dot{\alpha} \sum_{r=1}^{\infty} \Psi_k \dot{q}_r \operatorname{sgn}(\dot{\mathbf{R}}) \tag{2.13}$$

where Ψ_k is a constant defined by $\Psi_k = \int_y b(y) y \phi_r \phi_k\, dy$, and r is a new modal index inclusive of k. Unlike the aerodynamic loading term, $Q_{\zeta,k}$ is a function of the wing's elastic deformation velocity as well as its rigid body rotation. It effectively behaves as a time-periodic aerodynamic damping term that attenuates the elastic oscillations of the wing. For this reason, we refer to $Q_{\zeta,k}$ as aerodynamic damping hereafter.

(iii) Added Mass

Added mass is a phenomena where a volume of air displaced by an accelerating structure increases the effective inertia of that structure. Insect wings have a low surface density and high surface area, so added mass cannot safely be neglected. In this section, we derive an expression to incorporate added mass into the FSI model.

Added mass is proportional to the differential mass's out-of-plane acceleration $\mathbf{a}_z$ given by

$$\mathbf{a}_z = [y\ddot{\alpha} + \sum_{k=1}^{\infty} \phi_k (\ddot{q_k} - q_k \dot{\alpha}^2)] \mathbf{e}_z \tag{2.14}$$

From [34], the added mass force per unit length $d\mathbf{F}_{am}$ for a thin two-dimensional wing section is

$$d\mathbf{F}_{am} = -\mathbf{a}_z \pi \rho_f \left[\frac{b(y)}{2}\right]^2 \tag{2.15}$$

Substituting $\mathbf{a}_z$ into the above and converting the physical force to the modal domain through Eq. 2.3 yields three terms. The first added mass term is

$$Q_{am,k} = -\ddot{\alpha} \sum_{k=1}^{\infty} \tau_k \tag{2.16}$$

where $\tau_k = \pi \rho_f \int_y [b(y)/2]^2 y \phi_k \, dy$. Similar to rigid body drag, this added mass term is a function of rigid body rotation only and is not influenced by the elastic deformation of the wing. We will refer to this term as rigid body added mass. The second added mass term is

$$Q_{S,k} = \dot{\alpha}^2 \sum_{k=1}^{\infty} \mu_k q_k \tag{2.17}$$

where $\mu_k = \pi \rho_f \int_y [b(y)/2]^2 \phi_k^2 \, dy$. Interestingly, $Q_{S,k}$ is influenced both by the wing's angular velocity as well as its instantaneous shape. Similar to the centrifugal softening observed in the structural model, this term modulates the wing's stiffness periodically; for this reason, we refer to $Q_{S,k}$ as added mass stiffness. The final added mass term is

$$Q_{M,k} = -\sum_{k=1}^{\infty} \mu_k \ddot{q}_k \tag{2.18}$$

where $Q_{M,k}$ is proportional to the acceleration resulting from structural deformation. This term adds to the perceived mass of the wing if the wing is vibrating in air, and thus we refer to it as added mass inertia. Due to added mass inertia, the natural frequencies of the wing are lower in air than in vacuum.

(b) Computational Modeling

Numerical studies focused on flapping wings often rely on CFD and FEA. The accuracy of these direct numerical models is generally assumed to be better than that of their reduced-order counterparts, though at the expense of greater computational costs. Here, we develop a two-way coupled CFD and FEA model to predict the dynamic response of the flapping wing. This high-fidelity computational model enables us to incorporate dynamic phenomena neglected by the DBET model, such as unsteady aerodynamics and structural non-linearity. For our model, we use Siemens' Star-CCM+ (v15.04.008) CFD package and Dassault Systèmes Abaqus 2019 (6.19-1) FEA package interfaced via Co-simulia.

CFD calculates the pressure on the wing's surface and surrounding flow field by solving the Navier-Stokes equations. In order to resolve turbulence without requiring untenable computation times, we rely on a Spalart-Allmaras (SA) model to close the Reynolds-averaged Navier-Stokes (RANS) equations. RANS formulations are the most commonly used methods for modeling turbulent flows, and the SA model was chosen for its efficiency as a one-equation model as well as its efficacy in aerodynamic and transient flows. We use a Chimera mesh approach to account for the larger rigid-body rotation of the flapping wing [35]. This method uses multiple meshes (Fig. 2) – one that rotates with the wing (the *overset* mesh) and another that remains stationary and describes the entire fluid domain (the *background* mesh). Interpolation between the boundary of the overset mesh and the background mesh allows the conservation of mass and momentum to be maintained across both regions. In addition to the large prescribed rotations, there is a significant deformation on the wing due to its flexibility. To account for this deformation, our overset mesh region uses a radial basis function (RBF) mesh morphing method to stretch and compress elements around the wing as it deforms. These meshing methods allow the CFD model to run dynamically without the requirement of remeshing the domain at each timestep.

We used Abaqus FEA to resolve wing deformation resulting from aerodynamic loads interpolated onto the wing from the Star-CCM+ simulation and the prescribed rotational kinematics. The FEA model incorporates nonlinear geometric effects to account for the large displacements associated with our prescribed flapping profile. To apply the flapping kinematics to the FEA model, we imposed pinned boundary conditions along the wing's root edge. The root edge was prescribed a periodic angular displacement consistent with the rotation amplitudes and frequencies described in the simulation parameters section. We use an implicit solver to calculate the spatiotemporal deformation field at each time step.

Lastly, the CFD and FEA models are integrated via Abaqus Co-simulia. This allows for communication between the structural and fluid solvers at each timestep. Abaqus leads the time marching by first applying the prescribed kinematics described above, then resolving the structural deformation of the wing. The wing's new geometry and rigid body rotation are then sent to Star-CCM+ in terms of its nodal displacements. Star-CCM+ applies the imported displacements to its wing geometry and uses the displacements for the initiation of the RBF morphing of the overset mesh. The fluid domain in Star is resolved based on the impact of the wing's rotation and deformation on the fluid, and then the shear and normal pressures on the wing surfaces are exported and sent back to Abaqus. Finally, the wing's structural deformation is resolved in Abaqus, and the process repeats until a quasi-steady state response and desired physical time are reached.

3. Experimental Methods

We developed a simple experiment to evaluate the accuracy of the flapping wing FSI models. We used a mechanized rotation stage to prescribe flapping kinematics to a thin paper wing. Wing deformation was recorded via high-speed videography and wingtip displacement was calculated relative to the rigid body rotation of the wing using motion capture.

The mechanized rotation stage (Fig. 3) used for all experiments is summarized in [33]. Flapping trials were filmed with a high-speed video camera (Krontech, Chronos 2.1-HD) at 2996 frames per second with a spatial resolution of 1280 x 512 pixels; see supplementary material for a video of

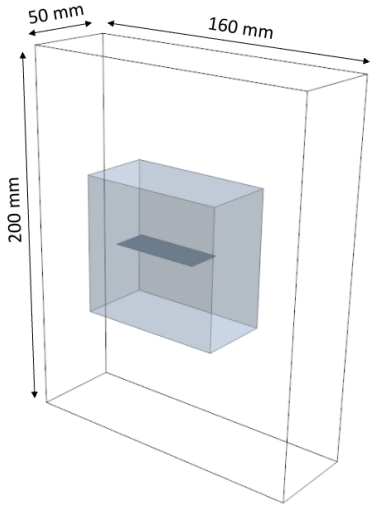

Figure 2. Background mesh (dimensions labeled) and overset mesh (grey) of the fluid domain in Star-CCM+. The rectangular wing is seen in dark grey within the overset mesh. The background mesh must be large enough to accommodate flapping kinematics, while the overset mesh must accommodate the out-of-plane deformation of the wing.

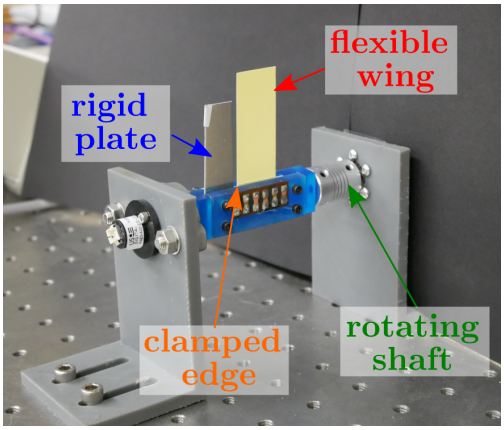

Figure 3. Mechanized SDOF rotation stage used to drive the rigid body rotation of the flexible wing.

the wing flapping at 10 Hz. The experiment was back-lit using a Godox SL-200W LED studio light. Recordings were post-processed in MATLAB. The tip of the flexible wing and the reference plate were tracked in a world frame using the DLTdv digitizing tool from the Hedrick lab [36]. We placed a thick metal plate behind the flexible paper wing to serve as a reference for the wing's rigid body. The rotation angle was measured from the center of rotation and the tip of the reference plate. The out-of-plane displacement of the flexible wing was determined with respect to a rotating coordinate system attached to the reference plate. We identified wingtip displacement for three consecutive flapping periods and then fit the wingtip displacement as a function of time using a fifth order Fourier series. We compared curve-fitted wingtip displacement to model predictions.

(a) Experimental & Simulation Parameters

All simulation properties are summarized in Tab. 1. The paper wing's length, chord width and surface area are similar to that of a Hawkmoth *Manduca sexta* forewing, though the paper wing weighs about four or five times as much; about 200 mg for the paper wing compared to 40 mg for the moth wing [37]. *M. sexta* are a common model organism in the study of flapping wing flight.

Experimental studies show that *M. sexta* flap at about 1/3 the natural frequency of their forewing [38], and research suggests this flapping-to-natural frequency ratio is aerodynamically and energetically beneficial as well [39–42]. Consequently, we wanted to ensure experiments encompassed the 1/3 flapping-to-natural frequency ratio. We measured the first natural frequency of the wing by displacing it and allowing it to freely vibrate. Free vibration was recorded using a laser vibrometer (Polytec, PSV-400). The first natural frequency was 30.1 Hz, which includes the effect of added mass. Based on this finding, we selected a flapping frequency range from 8 - 12 Hz at 1 Hz increments with a target amplitude of around 60°. Actual experimental rotation amplitudes varied between 52 - 58°; we used these measured rotation amplitudes to populate models.

Both DBET and computational models require a representation of the wing structure. For the DBET model, we use analytical expressions to calculate the wing's natural frequencies and mode shapes [43]. We retained only a single vibration mode. For the computational model, we used Abaqus FEA. The wing was assumed to be isotropic and homogeneous. It was discretized into 2560 eight node brick elements (4 through thickness, 640 over the surface), which was sufficient for the wing's first three natural frequencies to converge (Fig. S1). The first natural frequency occurred at 31.6 Hz and corresponded to the bending mode (Fig. 4). Prior wing characterization *in vacuo* suggests added mass will reduce this natural frequency by about 1.2 Hz, bringing it

Table 1. Simulation parameters.

Wing Parameters			
Variable	**Description**	**Value**	**Unit**
L	Length	5	cm
w	Width	2	cm
t	Thickness	0.017	cm
ρ	Density	1.2	g/cm^3
E_{DBET}	Young's modulus (DBET)	9.5	GPa
E_{COMP}	Young's modulus (Computational)	9.085	GPa
f	Flap frequency	8 - 12	Hz
α_0	Flap angle	0.9-1.01	Rad
Fluid Models			
Variable	**Description**	**Value**	**Unit**
Δt	Time step	1	ms
ρ_f	Air Density	0.001250	g/cm^3
C_D	Drag Coefficient	3.4	-
μ_a	Dynamic Viscosity of Air	1.855×10^5	Pa-s
	Dimensions of the background mesh (L $\times$ W $\times$ H)	160 X 50 X 200	mm
	Mean element length of the background mesh	1.2	mm
	Number of elements in the background mesh	641,817	-
	Dimensions of the overset mesh (L $\times$ W $\times$ H)	40 X 80 X 60	mm
	Mean element length of the overset mesh	0.6	mm
	Mean element length of the wing surface	0.6	mm
	Number of prism layers off the wing	5	-
	Prism-layer growth rate	1.5	-
	Number of elements in the overset mesh	535,653	-

into close agreement with the experimentally measured value [33]. Note that natural frequencies calculated via FEA are typically higher than those calculated by analytically; we therefore used different Young's modulus to ensure both computational and DBET models have the same wing natural frequencies (Tab. 1).

The background mesh region of the CFD model was sized to enclose the wing's full flapping motion and the major flow structures leaving the wing's surface. The overset mesh region around the wing was sized to enclose the total wing deformation and included additional clearance to minimize the creation of malformed or warped elements during the RBF morphing step. In order to increase the accuracy of the pressure calculation on the surface of the wing, prism-layers at a finer resolution were added with the default growth rate of 1.5. An appropriate element size was determined by monitoring the maximum aerodynamic moment of the wing. The average element length was decreased while ensuring that cells along the boundary of the overset mesh were never smaller than half those of the neighboring background mesh cells to minimize numerical diffusion across the Chimera boundary. Results of the mesh convergence can be seen in (Fig. S2), with a total

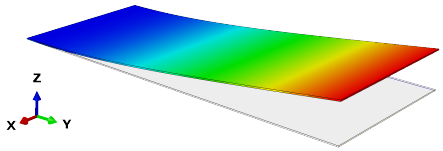

Figure 4. First vibration mode of the wing superimposed on undeformed wing geometry.

number of elements of above one million being considered sufficiently converged relative to the computational time required. After conducting the mesh convergence, a time-step convergence study was also performed, resulting in a time-step of 1 ms, and seen in (Fig. S2). Monitoring the aerodynamic moment and tip deflection, a total of 0.5 sec were simulated to ensure the results were periodically steady.

4. Results

In this section, we investigate wingtip deflection measured experimentally and compare it to that calculated via DBET and computational FSI models. First, consider the experimental results. Wingtip deflection is shown as a function of stroke phase for flapping frequencies between 8-12 Hz in Fig. 5. Peak wingtip deflections range from 0.69 cm at 8 Hz to 1.83 cm at 12 Hz, representing deflections with magnitudes of 15 - 37% of the wing length. For all frequencies, maximum peak deflection is delayed from the transition between the upstroke and downstroke. The delay between stroke transition and peak deflection increases with flap frequency. Because inertial forces are proportional to the angular acceleration, this delay likely results from aerodynamic effects. The wing deforms primarily at the flapping frequency, but also experiences a lesser response at three times the flapping frequency. The displacement waveform qualitatively changes with flapping frequency, suggesting the third harmonic response is sensitive to flap frequency and does not scale proportionally to the first harmonic response.

To quantitatively compare model predictions to experimental findings, we curve fitted steady-state wingtip displacements using a fifth-order Fourier series considering three subsequent wingbeats for experimental measurements and the final wingbeat simulated for DBET and computational models. From the curve-fitted data, we calculated the overall wingtip displacement and first and third harmonic magnitudes as a function of flap frequency (Fig. 6). No other harmonics contributed significantly to wing deformation. Note that for the experimental case, overall wingtip displacement varied modestly between the upstroke and downstroke (Fig. 5). This occurred due to a weight imbalance of the wing clamping mechanism, which caused the prescribed rotation to overshoot slightly more on the downstroke than on the upstroke. We averaged maximum displacements on the upstroke and downstroke for the experimental case in order to make better comparisons against the models.

DBET and computational models predicted the wing response fairly well. Across the considered frequency range, the DBET and computational models captured peak displacements within 13% and 30%, respectively. In agreement with the experiment, both models showed that the wing deformed at its flap frequency and three times its flap frequency. The DBET and computational models had maximum magnitude errors of 16% and 34% at the first harmonic and 72% and 63% at the third harmonic. The largest magnitude errors occur at the highest flapping frequency considered, while the error at reduced frequencies was much lower for both models.

Both models captured qualitative changes in the wing response. Each predicted that the first harmonic magnitude grows monotonically with respect to flap frequency. The experiment showed that the third harmonic magnitude experiences a local maximum and subsequently decreases. The peak in the third harmonic response indicates resonance, where the resonance condition may occur from an aerodynamic force coinciding with the wing's first natural frequency. Previous work suggests this resonance may occur even in a vacuum due to the interaction of inertial forces with the wing's periodically varying stiffness. Within the flapping frequency range considered, the DBET and computational model predicted a monotonic increase of the third harmonic magnitude. However, the slope of the third harmonic response suggests that its magnitude may decrease at flap frequencies exceeding 12 Hz. In general, the computational model captures the timing of the deformation waveform more accurately relative to the DBET model.

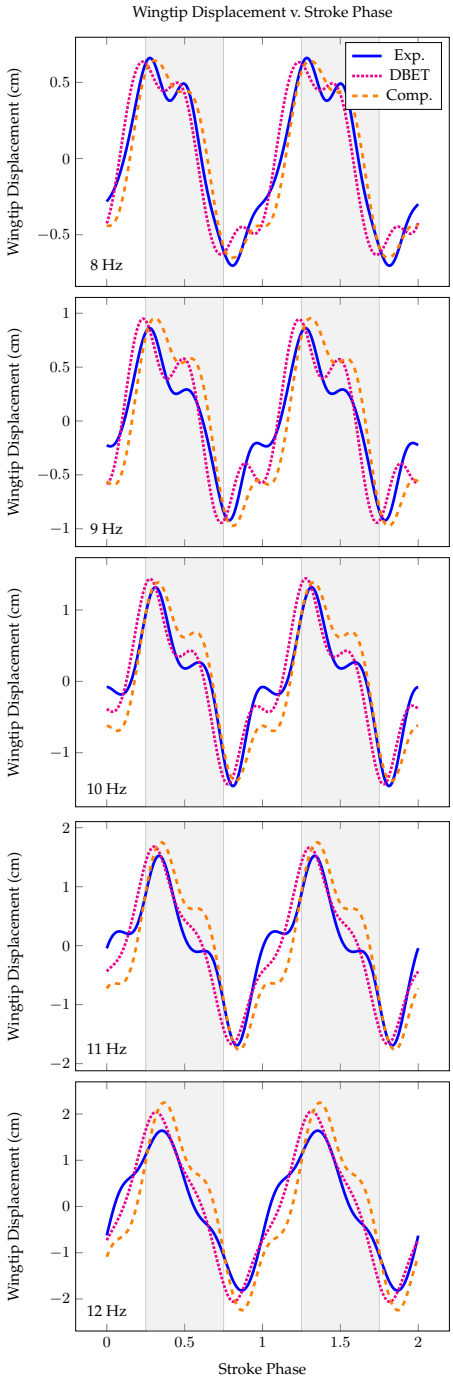

Figure 5. Wingtip displacements calculated via DBET and computational models are compared to experimental measurements for flapping frequencies 8 - 12 Hz. Displacements are shown as a function of stroke phase over two flapping cycles. Gray regions indicate downstroke and white regions indicate upstroke.

5. Discussion

Experimental results suggest that both the DBET and computational models are accurate within a range of flapping-to-natural frequency ratios and wingtip displacements relevant to larger flying

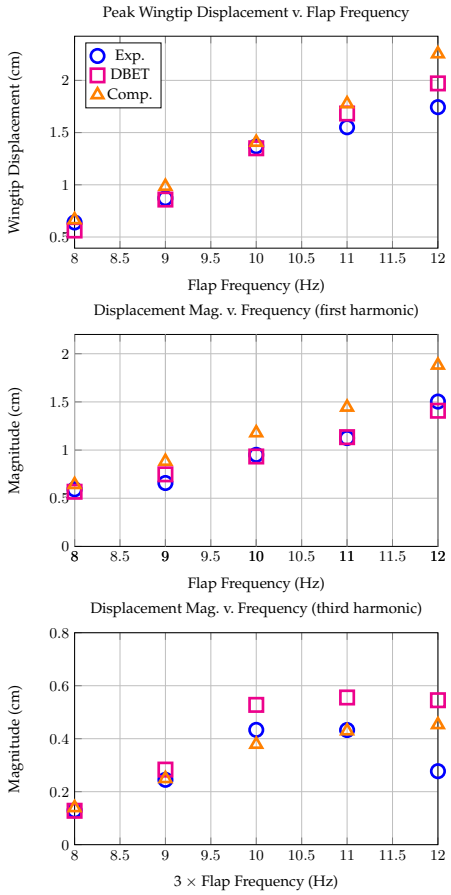

Figure 6. Peak wingtip displacement, as well as first and third harmonic magnitude components of wingtip displacement, as a function of flap frequency measured experimentally and as predicted by DBET and computational models.

insects. The DBET model solves for wing deformation faster than the computational model; using a workstation with 32GB of DDR4 RAM, an Intel i9-9900K 3.6GHz CPU (4 processing threads in

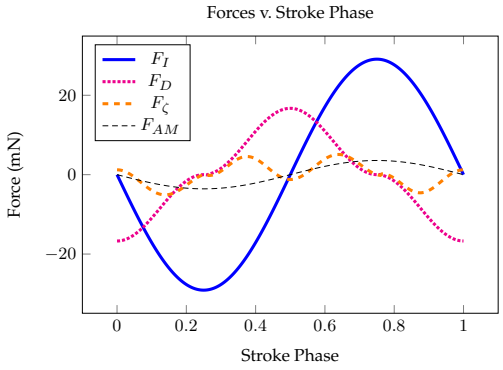

Figure 7. DBET model predictions of the steady-state inertial and aerodynamic forces acting on the experimental wing flapping at 10 Hz. Added mass stiffness and inertia are small compared to the forces pictured and are omitted for clarity.

the CFD model), the DBET model solves in about 30 ms per wingbeat whereas the computational model solves in about 8.9×10^6 ms per wingbeat. This represents a 5 order of magnitude difference between the solution times achievable by DBET and computational methods. Given the level of accuracy achieved, the DBET framework is therefore a promising development that could underpin more complex flapping wing FSI models.

While economical, the DBET model has limitations that may make computational modeling desirable in some contexts. First, the computational model resolves the entire flow structure surrounding the deforming wing whereas the DBET model does not. As a result, computational models are more appropriate for capturing certain fluid phenomena such as clap-and-fling or vortex shedding. Second, the 3D computational model can capture pressure variations along the chord width. Indeed, pressure varied along the wing chord throughout the stroke cycle, though these pressures were symmetric about the wing's centerline and did not cause it to twist. Third, the DBET framework does not account for in-plane stretching or geometric nonlinearity, though experimental results do not indicate these factors contribute significantly to the wing's structural response. Lastly, while DBET provides a significant tool in the analysis of flapping wings, more complex fluid dynamics could be incorporated to improve the accuracy of these models, particularly as they are scaled to accommodate MDOF kinematics. Because the computational models can calculate the full fluid dynamics of a system, they will allow for better tuning of parameters that can account for phenomena, such as dynamic stall, in the future.

Despite these limitations, the semi-analytical nature of the DBET model allows us to interpret it in order to better understand the physics governing wing deformation. For example, DBET can be used to evaluate the forces acting on the wing and how these forces scale relative to one another. Understanding this physical scaling can elucidate the influence wing deformation has on different flying insects, particularly those with variable wing lengths or aspect ratios and flapping amplitudes. Derived expressions for inertial and aerodynamic forces can also be used to better understand how deformation affects other physics relevant to flight, such as power expenditures.

In what follows, we use the DBET model to investigate the forces responsible for wing deformation. The forces acting on the experimental wing flapping at 10 Hz, estimated via the DBET model, are shown as a function of stroke phase in Fig. 7.

(a) Aerodynamic Drag vs. Inertia

Research suggests that deformation in Hawkmoth *M. sexta* wings, which are of comparable size to the experimental wing, is dominated by inertial forces [16]. Rigid body drag was the largest aerodynamic force acting on the wing during our experiment. The magnitude ratio between rigid body drag force F_D and inertial force F_I scales with

$$\left|\left|\frac{F_D}{F_I}\right|\right| \propto \frac{\alpha_0 \rho_f L}{\rho_s} \tag{5.1}$$

where ρ_s is the wing's mass per unit area and α_0 is the flapping amplitude. Intuitively, deformation will be dominated by inertial forces in heavy wings and aerodynamic forces in lightweight wings. Inertial forces increase linearly with wing length, while aerodynamic forces scale quadratically. Consequently, longer wings experience greater aerodynamic loading. When rotation amplitudes are much less than one radian, inertial forces tend to overwhelm aerodynamics. Specific to our wing and flapping amplitude, F_I is approximately two times greater than F_D (Fig. 7). However, the surface density of the paper wing is about 4-5 times larger than that of an *M. sexta* wing of comparable size. Adjusting the wing's surface density to 20% its original value inverts this trend, where F_D now exceeds F_I by 2.5 times. Based on this simplified analysis, we conjecture that if the complex wing structure and flapping kinematics were taken into account, the aerodynamic and inertial forces contributing to *M. sexta* wing deformation are similar in magnitude.

(b) Aerodynamic Drag vs. Aerodynamic Damping

Though rigid body drag dominates the remainder of the aerodynamic forces in most cases, there are instances where aerodynamic damping is appreciable. If the wing's elastic response occurs primarily at the flapping frequency, the ratio between rigid body drag F_D and aerodynamic damping F_ζ is proportional to

$$\left|\left|\frac{F_D}{F_\zeta}\right|\right| \propto \frac{\alpha_0 L^3}{\int_y yW(y)\,dy} \tag{5.2}$$

If we assume the deformed shape is a bending mode represented by $W(y) = \frac{\beta}{L}y^2$, where β is the ratio between the wingtip deflection and wing length, this simplifies to

$$\left|\left|\frac{F_D}{F_\zeta}\right|\right| \propto \frac{\alpha_0}{\beta} \tag{5.3}$$

This expression demonstrates the significance of the relative magnitudes of the wing's rigid body motion and elastic deformation. For a fixed rotation amplitude of 1 radian, aerodynamic damping will exceed rigid body drag only when wingtip deflection exceeds the length of the wing, a condition which is physically unrealistic in flight. However, for a much smaller rotation amplitude, the wingtip deflection could easily exceed 10% of wing length if the wing was highly flexible. For the experimental parameters in this work, β ranges about 0.15 - 0.37, where rigid body drag is larger than aerodynamic damping but on the same order of magnitude.

This scaling behavior between rigid body drag and aerodynamic damping has interesting implications at resonance. Most insects flap below the first natural frequency of their wings [44], but superharmonic resonance, or resonance induced by higher-order harmonics of aerodynamic forces, may occur if the insect flaps at an integer quotient of its wing's natural frequency. Indeed, prior work suggests flapping at 1/3 of the wing's natural frequency may confer energetic and aerodynamic benefits [40,41]. However, these benefits would diminish if wing deformation becomes excessive. The above scaling suggests that aerodynamic damping may restrict unfavorable levels of deformation, since β becomes large in these contexts. In our own experiment, we found that aerodynamic damping overwhelms viscous damping of the wing structure. Thus, aerodynamic damping may play a more substantial role in attenuating large deformations relative to viscous damping inherent to the structure.

(c) Aerodynamic Drag vs. Added Mass

After rigid body drag and aerodynamic damping, rigid body added mass is the last fluid forcing term of significance at these length scales (Fig. 7). The magnitude ratio between rigid body drag F_D and rigid body added mass F_{AM} is proportional to

$$\left|\left|\frac{F_D}{F_{AM}}\right|\right| \propto \frac{\alpha_0 L}{b} \tag{5.4}$$

Rigid body added mass is greater in short, fat wings, whereas rigid body drag is greater in longer, more slender wings. Because rigid body added mass scales linearly with length and rigid body drag quadratically, wings with low rotation amplitudes are more influenced by the former. Added mass may also drastically lower the natural frequency of insect wings. Modal analysis in air and *in vacuo* shows that added mass reduces the first natural frequency of the *M. sexta* forewing by 30% [45]. The wing's effective kth natural frequency $\omega_{eff,k}$ satisfies

$$\omega_{eff,k}^2 = \frac{\omega_k^2}{1+\mu_k} \tag{5.5}$$

where for a cantilever beam, μ_k is proportional to

$$\mu_k \propto \frac{b\rho_f}{\rho_s} \tag{5.6}$$

The reduction of the wing's fundamental frequency from added mass is therefore sensitive to the ratio between the density of air and the wing's surface density. This explains why the fundamental frequency of the *M. sexta* forewing is more greatly influenced by added mass compared to the paper wing used in our experiment.

Acknowledgment

This research was supported the National Science Foundation under awards Nos. CBET-1855383 to MJ and EJ and CMMI-1942810 to MJ. Any opinions, findings, and conclusions or recommendations expressed in this material are those of the author(s) and do not necessarily reflect the views of the National Science Foundation.

References

1. Steven Ho, Hany Nassef, Nick Pornsinsirirak, Yu-Chong Tai, and Chih-Ming Ho. Unsteady aerodynamics and flow control for flapping wing flyers. *Progress in Aerospace Sciences*, 39(8):635–681, 2003.
2. Mark Jankauski, TL Daniel, and IY Shen. Asymmetries in wing inertial and aerodynamic torques contribute to steering in flying insects. *Bioinspiration & biomimetics*, 12(4):046001, 2017.
3. Wei Shyy, Hikaru Aono, Satish Kumar Chimakurthi, Pat Trizila, C-K Kang, Carlos ES Cesnik, and Hao Liu. Recent progress in flapping wing aerodynamics and aeroelasticity. *Progress in Aerospace Sciences*, 46(7):284–327, 2010.
4. Gordon J Berman and Z Jane Wang. Energy-minimizing kinematics in hovering insect flight. *Journal of Fluid Mechanics*, 582:153–168, 2007.
5. Sanjay P Sane and Michael H Dickinson. The aerodynamic effects of wing rotation and a revised quasi-steady model of flapping flight. *Journal of experimental biology*, 205(8):1087–1096, 2002.
6. Anh Tuan Nguyen, Vu Dan Thanh Le, VN Duc, et al. Study of vertically ascending flight of a hawkmoth model. *Acta Mechanica Sinica*, 36(5):1031–1045, 2020.
7. Chong Shen, Yanpeng Liu, and Mao Sun. Lift and power in fruitflies in vertically-ascending flight. *Bioinspiration & biomimetics*, 13(5):056008, 2018.
8. Xueguang Meng, Yanpeng Liu, and Mao Sun. Aerodynamics of ascending flight in fruit flies. *Journal of Bionic Engineering*, 14(1):75–87, 2017.
9. Simon M Walker and Graham K Taylor. A semi-empirical model of the aerodynamics of manoeuvring insect flight. *J. R. Soc. Interface*, 2020.
10. Mohamed Yehia Zakaria. Unsteady aerodynamics of highly maneuvering flyers. In *Biomimetics*. IntechOpen, 2021.
11. Hao Wang, Lijiang Zeng, Hao Liu, and Chunyong Yin. Measuring wing kinematics, flight trajectory and body attitude during forward flight and turning maneuvers in dragonflies. *Journal of Experimental Biology*, 206(4):745–757, 2003.
12. Toshiyuki Nakata and Hao Liu. A fluid–structure interaction model of insect flight with flexible wings. *Journal of Computational Physics*, 231(4):1822–1847, 2012.
13. Guoyu Luo and Mao Sun. The effects of corrugation and wing planform on the aerodynamic force production of sweeping model insect wings. *Acta Mechanica Sinica*, 21(6):531–541, 2005.
14. Xue Guang Meng, Lei Xu, and Mao Sun. Aerodynamic effects of corrugation in flapping insect wings in hovering flight. *Journal of Experimental Biology*, 214(3):432–444, 2011.
15. Robert Richard Harbig, John Sheridan, and Mark Christopher Thompson. Relationship between aerodynamic forces, flow structures and wing camber for rotating insect wing planforms. *Journal of Fluid Mechanics*, 730:52, 2013.
16. Stacey A Combes and Thomas L Daniel. Into thin air: contributions of aerodynamic and inertial-elastic forces to wing bending in the hawkmoth manduca sexta. *Journal of Experimental Biology*, 206(17):2999–3006, 2003.
17. Fang-Bao Tian, Hu Dai, Haoxiang Luo, James F Doyle, and Bernard Rousseau. Fluid–structure interaction involving large deformations: 3d simulations and applications to biological systems. *Journal of computational physics*, 258:451–469, 2014.

18. Daisuke Ishihara, T Horie, and Mitsunori Denda. A two-dimensional computational study on the fluid–structure interaction cause of wing pitch changes in dipteran flapping flight. *Journal of Experimental Biology*, 212(1):1–10, 2009.
19. Masaki Hamamoto, Yoshiji Ohta, Keita Hara, and Toshiaki Hisada. Application of fluid–structure interaction analysis to flapping flight of insects with deformable wings. *Advanced Robotics*, 21(1-2):1–21, 2007.
20. T Fitzgerald, M Valdez, M Vanella, E Balaras, and B Balachandran. Flexible flapping systems: Computational investigations into fluid-structure interactions. *The Aeronautical Journal*, 115(1172):593–604, 2011.
21. Jian Tang, Satish Chimakurthi, Rafael Palacios, Carlos Cesnik, and Wei Shyy. Computational fluid-structure interaction of a deformable flapping wing for micro air vehicle applications. In *46th AIAA Aerospace Sciences Meeting and Exhibit*, page 615, 2008.
22. Tomonori Yamada and Shinobu Yoshimura. Line search partitioned approach for fluid-structure interaction analysis of flapping wing. *Computer Modeling in Engineering and Sciences*, 24(1):51, 2008.
23. David Willis, Emily Israeli, Per-Olof Persson, Mark Drela, Jaime Peraire, Sharon Swartz, and Kenny Breuer. A computational framework for fluid structure interaction in biologically inspired flapping flight. In *25th AIAA Applied Aerodynamics Conference*, page 3803, 2007.
24. Bruno A Roccia, Sergio Preidikman, and Balakumar Balachandran. Computational dynamics of flapping wings in hover flight: a co-simulation strategy. *AIAA Journal*, 55(6):1806–1822, 2017.
25. John David Anderson and J Wendt. *Computational fluid dynamics*, volume 206. Springer, 1995.
26. Mark Jankauski and IY Shen. Dynamic modeling of an insect wing subject to three-dimensional rotation. *International Journal of Micro Air Vehicles*, 6(4):231–251, 2014.
27. Charles P Ellington. The novel aerodynamics of insect flight: applications to micro-air vehicles. *Journal of Experimental Biology*, 202(23):3439–3448, 1999.
28. Q Wang, JFL Goosen, and F van Keulen. An efficient fluid–structure interaction model for optimizing twistable flapping wings. *Journal of Fluids and Structures*, 73:82–99, 2017.
29. Haithem E Taha, Muhammad R Hajj, and Philip S Beran. State-space representation of the unsteady aerodynamics of flapping flight. *Aerospace Science and Technology*, 34:1–11, 2014.
30. Krithika Manohar, Steven L Brunton, and J Nathan Kutz. Environment identification in flight using sparse approximation of wing strain. *Journal of Fluids and Structures*, 70:162–180, 2017.
31. Deepa Kodali and Chang-kwon Kang. An analytical model and scaling of chordwise flexible flapping wings in forward flight. *Bioinspiration & biomimetics*, 12(1):016006, 2016.
32. Deepa Kodali, Chang-Kwon Kang, and Hikaru Aono. Analytical aerodynamic model of spanwise flexible flapping wings in forward flight. In *55th AIAA Aerospace Sciences Meeting*, page 0331, 2017.
33. Ryan K Schwab, Heidi E Reid, and Mark Jankauski. Reduced-order modeling and experimental studies of bilaterally coupled fluid–structure interaction in single-degree-of-freedom flapping wings. *Journal of Vibration and Acoustics*, 142(2), 2020.
34. John P Whitney and Robert J Wood. Aeromechanics of passive rotation in flapping flight. *Journal of Fluid Mechanics*, 660:197–220, 2010.
35. Hidajet Hadzic. Development and application of finite volume method for the computation of flows around moving bodies on unstructured, overlapping grids. *Ph.D. thesis, Technische Universität Hamburg, Hamburg*, 2006.
36. Tyson L Hedrick. Software techniques for two-and three-dimensional kinematic measurements of biological and biomimetic systems. *Bioinspiration & biomimetics*, 3(3):034001, 2008.
37. Heidi Reid, Huimin Zhou, Miles Maxcer, Robert KD Peterson, Jia Deng, and Mark Jankauski. Toward the design of dynamically similar artificial insect wings. *International Journal of Micro Air Vehicles*, 13:1756829321992138, 2021.
38. Aaron Norris, Anthony Palazotto, and Richard Cobb. Structural dynamic characterization of an insect wing. In *51st AIAA/ASME/ASCE/AHS/ASC Structures, Structural Dynamics, and Materials Conference 18th AIAA/ASME/AHS Adaptive Structures Conference 12th*, page 2790, 2010.
39. Heidi E Reid, Ryan K Schwab, Miles Maxcer, Robert KD Peterson, Erick L Johnson, and Mark Jankauski. Wing flexibility reduces the energetic requirements of insect flight. *Bioinspiration & biomimetics*, 14(5):056007, 2019.

40. Mark Jankauski, Ziwen Guo, and IY Shen. The effect of structural deformation on flapping wing energetics. *Journal of Sound and Vibration*, 429:176–192, 2018.
41. Marcos Vanella, Timothy Fitzgerald, Sergio Preidikman, Elias Balaras, and Balakumar Balachandran. Influence of flexibility on the aerodynamic performance of a hovering wing. *Journal of Experimental Biology*, 212(1):95–105, 2009.
42. Hu Dai, Haoxiang Luo, and James F Doyle. Dynamic pitching of an elastic rectangular wing in hovering motion. *Journal of Fluid Mechanics*, 693:473–499, 2012.
43. Singiresu S Rao. *Vibration of continuous systems*, volume 464. Wiley Online Library, 2007.
44. Ngoc San Ha, Quang Tri Truong, Nam Seo Goo, and Hoon Cheol Park. Relationship between wingbeat frequency and resonant frequency of the wing in insects. *Bioinspiration & biomimetics*, 8(4):046008, 2013.
45. Aaron G Norris. *Experimental characterization of the structural dynamics and aero-structural sensitivity of a hawkmoth wing toward the development of design rules for flapping-wing micro air vehicles*. Air Force Institute of Technology, 2013.

Supplementary Material

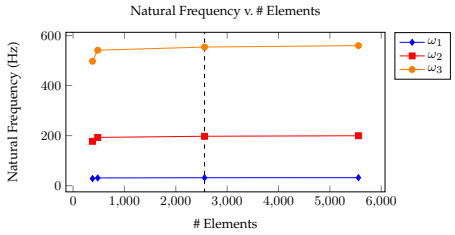

Figure S1. Convergence studies for the FEA model show that the first three natural frequencies converge around 2500 elements. Operating point shown in dashed lines.

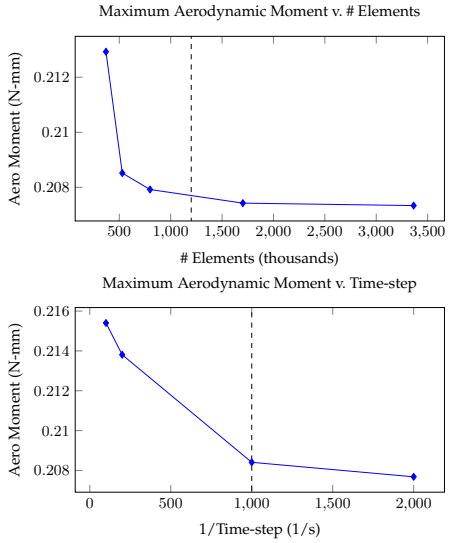

Figure S2. Convergence studies for the CFD model. (Top) Maximum aerodynamic moment at steady-state as a function of element count, and (Bottom) Maximum aerodynamic moment at steady-state as a function of the inverse of the time step. Operating points shown in dashed lines.

QUASI-3D DEFORMABLE BLADE ELEMENT AND UNSTEADY VORTEX LATTICE REDUCED-ORDER MODELING OF FLUID-STRUCTURE INTERACTION IN FLAPPING WINGS

Contribution of Authors and Co-Authors

Manuscript in following chapter

Author: [Ryan Schwab]

Contributions: [Integrated computational fluid dynamics and finite element analysis solvers into a high fidelity flapping wing model used to validate reduced order models]

Author: [Joseph Reade]

Contributions: [Developed quasi-3D Unstead Vortex Latice Method reduced order model for flapping wings, two-way coupled to a modal-truncation based structural solver]

Author: [Mark Jankauski]

Contributions: [Developed blade element theory reduced order model for flapping wings and modal-truncation based structural solver, and two-way coubled these to form "Deformable Blade Element Theory" model]

Manuscript Information

[R. Schwab, J. Reade, M. Jankauski]

[Physics of Fluids]

Status of Manuscript:
____ Prepared for submission to a peer-reviewed journal
____ Officially submitted to a peer-reviewed journal
____ Accepted by a peer-reviewed journal
_X_ Published in a peer-reviewed journal

[American Institute of Physics]
[Submitted: October 3rd, 2022]
[Published: 7 December 2022]
[Volume: 34]
[doi: 10.1063/5.0129128]

Physics of Fluids

Quasi three-dimensional deformable blade element and unsteady vortex lattice reduced-order modeling of fluid–structure interaction in flapping wings

Cite as: Phys. Fluids **34**, 121903 (2022); https://doi.org/10.1063/5.0129128
Submitted: 03 October 2022 • Accepted: 21 November 2022 • Accepted Manuscript Online: 21 November 2022 • Published Online: 07 December 2022

R. Schwab, J. Reade and M. Jankauski

Physics of Fluids ARTICLE scitation.org/journal/phf

Quasi three-dimensional deformable blade element and unsteady vortex lattice reduced-order modeling of fluid–structure interaction in flapping wings

Cite as: Phys. Fluids **34**, 121903 (2022); doi: 10.1063/5.0129128
Submitted: 3 October 2022 · Accepted: 21 November 2022 ·
Published Online: 7 December 2022

R. Schwab, J. Reade, and M. Jankauski[a)]

AFFILIATIONS

Department of Mechanical & Industrial Engineering, Montana State University, 220 Roberts Hall, Bozeman, Montana 59717, USA

[a)]Author to whom correspondence should be addressed: mark.jankauski@montana.edu

ABSTRACT

Flapping, flexible insect wings deform under inertial and fluid loading. Deformation influences aerodynamic force generation and sensorimotor control, and is thus important to insect flight mechanics. Conventional flapping wing fluid–structure interaction models provide detailed information about wing deformation and the surrounding flow structure, but are impractical in parameter studies due to their considerable computational demands. Here, we develop two quasi three-dimensional reduced-order models (ROMs) capable of describing the propulsive forces/moments and deformation profiles of flexible wings. The first is based on deformable blade element theory (DBET) and the second is based on the unsteady vortex lattice method (UVLM). Both rely on a modal-truncation based structural solver. We apply each model to estimate the aeromechanics of a thin, flapping flat plate with a rigid leading edge, and compare ROM findings to those produced by a coupled fluid dynamics/finite element computational solver. The ROMs predict wing deformation with good accuracy even for relatively large deformations of 25% of the chord length. Aerodynamic loading normal to the wing's rotation plane is well captured by the ROMs, though model errors are larger for in-plane loading. We then perform a parameter sweep to understand how wing flexibility and mass affect peak deflection, mean lift and average power. All models indicate that flexible wings produce less lift but require lower average power to flap. Importantly, these studies highlight the computational efficiency of the ROMs—compared to the convention modeling approach, the UVLM and DBET ROMs solve 4 and 6 orders of magnitude faster, respectively.

I. INTRODUCTION

Flying insects often serve as model organisms in the study of sensorimotor and neuromuscular control because they have relatively simple neural systems, yet are able to perform sophisticated tasks.[1] Insects may utilize halteres to sense angular velocities of their bodies,[2] campaniform sensilla to detect strains of their legs and exoskeleton,[3] and Johnston's organs to detect vibrations in the antennae to sense airflow.[4] Some insects utilize campaniform sensilla (strain-sensitive mechanoreceptors) distributed across their wings to encode deformations such that they can adjust their flapping kinematics for improved flight control.[5–7] Information regarding the insect body's angular velocity is also believed to be encoded in wing deformation,[8,9] hence making wing-based mechanoreception an essential sensory modality in insects that lack dedicated gyroscopic sensing organs. Wing flexibility and deformation are, therefore, critical to flight in many insect species.

In addition to sensory functions, deformation also influences wings' aerodynamic performance. Insect wings undergo large deformations due to both aerodynamic and inertial forces.[10–12] The surrounding fluid affects the wing deformation and vice versa, leading to a strong fluid–structure coupling. Wing flexibility may reduce the energetic requirements of flapping, since strain energy stored in the wing during elastic deformations may be recovered later in the wingbeat.[13] Wing flexibility also has a significant influence on thrust production through passive wing pitching and bending, which lowers drag forces and strengthens vortex production near the wing surface, thereby increasing lift forces.[14–16] Wing mass and the relative contribution of inertial and aerodynamic forces also play a role in efficiency. Lift-to-drag ratio is higher in cases where aerodynamic forces dominate deformation (e.g., low wing mass), likely due to smaller shed vortices and thus lower drag forces.[17] Additionally, flexibility may benefit

Physics of Fluids ARTICLE scitation.org/journal/phf

wing–wing interactions, such as during clap and fling type flapping, to enhance force generation. Studies show that wing deformation improves leading edge vortex (LEV) attachment and wake capture, where the wing interacts with shed vortices from the previous flap cycle to enhance force production.[18]

Owing to the experimental limitations in real insects, the characterization of structural and fluid phenomena surrounding flapping wings often relies on computational modeling.[11,19–26] Fluid modeling usually involves computational fluid dynamics (CFD) to solve the Navier–Stokes equations—a set of partial differential equations that describe the conservation of mass and conservation of momentum in fluid flows.[27] This fluid model is often used in conjunction with structural solvers such as finite element analysis (FEA) to evaluate bilateral fluid–structure interactions (FSIs).[11,19,22] Computational models have driven much of our current understanding of flapping wing mechanics, such as the development of LEVs[28] and the influence of venation patterns on spatially variable stiffness.[29] Additionally, computational models provide a platform to compare the performance of flexible wings to idealized rigid wings, where the latter are mathematically convenient but unrealistic in natural contexts.[11,30] While these computational models are an accepted instrument for studying flapping wing flight, they necessitate considerable computational resources, often requiring several days to reach converged solutions for each simulation. They are consequently challenged by studies that consider large parameter spaces, for example variable wing morphologies, flapping kinematics and material properties.

Because of the solution times required by higher-order flapping wing models, reduced-order models (ROMs) have emerged as useful frameworks to efficiently perform parametric and optimization studies. The two most common ROMs in flapping wing flight are based on quasi-static blade element theory (BET) and unsteady vortex lattice method (UVLM).[22,26,31–34] BET functions by discretizing a wing into airfoils that run along the wing's chord. The local aerodynamic forces and moments are determined via thin airfoil theory and are subsequently integrated over the wing surface to give the net forces and moments. BET is typically used to model rigid wings but has been extended to flexible wings in some contexts. For example, a BET-based formulation was used to model flexible wings experiencing single-degree-of-freedom rotation,[35] but because of the simplified kinematics, such a model cannot accommodate lifting flow. Wang *et al.* used BET to describe the aerodynamics of twistable wings subject to multiple-degree-of-freedom rotation,[36] though the structural model in this work is not amendable to the anisotropic or spatially variable material properties present in real insect wings.[37] Walker and Taylor developed a similar BET model for twistable wings, where the twist angle must be prescribed within this approach.[38]

UVLM estimates pressure over the wing surface by treating the wing and shed wake as an infinitely thin sheet of discrete vortices. These vortices cause a velocity gradient across the wing and thus a pressure differential. This method has the advantage of being significantly faster than high-fidelity CFD while still accounting for many unsteady phenomena.[22,39] Compared to BET, UVLM is more commonly used to describe the mechanics of two-dimensional (2D) or three-dimensional (3D) flexible wings,[22,26,33] but is more computationally expensive as well. One method to reduce the computational costs of UVLM (perhaps at the expense of accuracy) is to use a quasi three-dimensional approximation, similar to the one employed by BET. For a wing discretized spanwise into n segments, a quasi-3D approach reduces the number of required calculations by at least a factor of n. Vector calculations being reduced to two dimensions further enhance computational savings. However, to our knowledge, no such model has been developed for flapping wing flight.

Given the importance of wing flexibility in insect flight and the limitations of existing flapping wing fluid–structure interaction (FSI) models, the goal of the present work is to develop two quasi-3D ROMs of flapping, flexible wings and to benchmark the accuracy and computational times enabled by these models against a more conventional high-fidelity (HiFi hereafter) approach. Each ROM must be capable of estimating wing deformation and the bulk propulsive forces and moments of flapping. The first ROM is rooted in BET but accommodates wing deformation; we, therefore, refer to this model as deformable blade element theory (DBET hereafter). The second ROM is based on a quasi-3D UVLM approach (simply UVLM hereafter).

The remainder of the paper is organized as follows. First, we formulate the ROMs and describe the basis of the HiFi computational model. Then, we apply each model to predict the deformation and aerodynamics of a thin rectangular plate flapping in a quiescent environment. We assume the wing has a rigid leading edge, since the vibration modes measured in insect wings indicate that deformation is more pronounced at the trailing edge relative to the leading edge.[40,41] Though the ROMs may generalize to more complex wing structures (e.g., realistic planforms, vein structures), it is prudent to first benchmark their accuracy in a simplified context. We then compare propulsive forces and wing deformations estimated by each model, and perform a parametric study to quantify how wing stiffness and mass affect lift, peak deflection and average power requirements. Finally, we discuss the utility of these models within the field of insect flight and address some of the model limitations.

II. MATHEMATICAL MODELING

A. Flapping kinematics

First, we establish a wing-fixed system that rotates with the wing's rigid body motion (Fig. 1). The reference frame kinematics are identical across all modeling efforts and originated in Ref. 42. A wing is situated in an $X-Y-Z$ inertial coordinate system. The $X-Y-Z$ coordinate system undergoes a finite rotation α about the positive X direction, where α denotes the roll angle (also called flap angle) of the wing. The resulting $x''-y''-z''$ coordinate system is then rotated about y'' by angle β, where β represents wing pitch (also called wing rotation). The ensuing $x'-y'-z'$ system experiences finite rotation γ about the z' axis, where γ is wing yaw (sometimes stroke deviation). The terminal wing-fixed $x-y-z$ coordinate system is bound to the wing's rigid body rotation, where the wing is rotating about fixed point O. The unit vectors in the wing fixed frame are $\mathbf{e}_x$, $\mathbf{e}_y$, $\mathbf{e}_z$ and are directed along the x, y, and z axes, respectively. The angular velocity $\boldsymbol{\Omega}$ is

$$\boldsymbol{\Omega} = \underbrace{(\dot{\alpha}\cos\beta\cos\gamma + \dot{\beta}\sin\gamma)}_{\Omega_x}\mathbf{e}_x + \underbrace{(\dot{\beta}\cos\gamma - \dot{\alpha}\cos\beta\sin\gamma)}_{\Omega_y}\mathbf{e}_y + \underbrace{(\dot{\gamma} + \dot{\alpha}\sin\beta)}_{\Omega_z}\mathbf{e}_z, \tag{1}$$

where Ω_x, Ω_y, and Ω_z are the x, y, and z components of angular velocity with respect to the wing-fixed coordinate system.

Physics of Fluids ARTICLE scitation.org/journal/phf

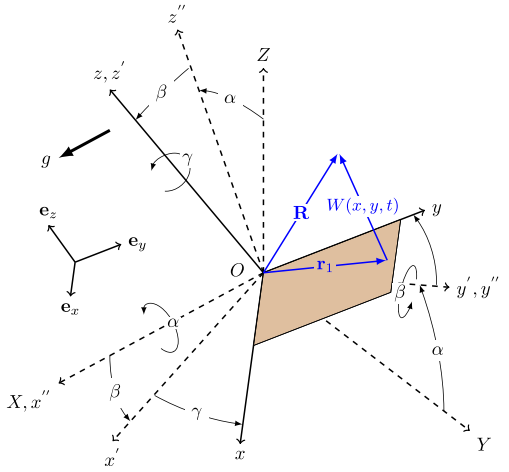

FIG. 1. Development of a $x - y - z$ coordinate system that rotates with the wing's rigid body motion. **R** is a position vector between the wing's fixed point of rotation O and a differential mass dm. Per our coordinate convention, gravity g acts in the $-X$ direction.

B. Reduced-order modeling

1. Structural modeling

Next, we derive a reduced-order structural modeling of the rotating, flexible wing. The structural model is general in the sense that it can incorporate any planar wing geometry and can interface with any appropriate fluid dynamic model. Within this work, we use this structural model in conjunction with the DBET and UVLM aerodynamic solvers. The benefit to this approach is that we must solve only for the time-response of the wing's vibration mode shapes rather than the time-response of the wing's individual degrees-of-freedom (assuming the wing can be discretized as a multiple-degree-of-freedom system). In practice, the number of modes needed to represent wing deformation is usually much smaller than the number of physical degrees of freedom, thereby representing a computational savings within the structural domain. The wing's vibration modes can be pre-computed analytically for simple structures or via finite element for more complex structures. The structural model framework originated in Ref. 43 and was extended in Ref. 44, and is summarized here to provide context to the present work. For a more thorough derivation, the reader is encouraged to refer to these references.

Consider a position vector **R** from the wing's fixed point of rotation O to a differential mass element dm located on the wing (Fig. 1). Position vector **R** is

$$\mathbf{R} = \underbrace{x\mathbf{e}_x + y\mathbf{e}_y}_{\mathbf{r}_1} + W(x,y,t)\mathbf{e}_z, \tag{2}$$

where x and y are the planar coordinates of dm (also described by position vector $\mathbf{r}_1$) and $W(x,y,t)$ is a small, unknown out-of-plane elastic deformation dependent on both space and time. The wing's in-plane motion is neglected. The velocity of dm is

$$\dot{\mathbf{R}} = \boldsymbol{\Omega} \times \mathbf{R} + \dot{W}(x,y,t)\mathbf{e}_z. \tag{3}$$

The wing's kinetic energy T is

$$T = \frac{1}{2}\int_m \dot{\mathbf{R}} \cdot \dot{\mathbf{R}}\, dm, \tag{4}$$

where the above represents an integration of the differential kinetic energy of dm over the wing's mass domain. Next, the potential energy U resulting from the wing's elastic deformation is

$$U = \frac{1}{2}\int_V \sigma(W, W)\, dV, \tag{5}$$

where σ is a symmetric, quadratic strain energy density function dependent on wing deformation $W(x,y,t)$ and V is the wing's volume. Next, we represent elastic deformation $W(x,y,t)$ via an eigenfunction expansion such that it can be calculated as space dependent mode shapes $\phi_k(x,y)$ multiplied by their time-dependent modal responses $q_k(t)$, given by

$$W(x,y,t) = \sum_{k=1}^{\infty} \phi_k(x,y) q_k(t). \tag{6}$$

Vibration modes $\phi_k(x,y)$ can be calculated via finite element or in some cases analytically. Mode shapes are normalized with respect to the wing's mass such that they satisfy

$$\int_m \phi_k \phi_r\, dm = \delta_{kr}, \tag{7}$$

$$\int_V \sigma(\phi_k, \phi_r)\, dV = \omega_k^2\, \delta_{kr}, \tag{8}$$

where δ_{kr} is the Kronecker delta function, and ω_k is the kth natural frequency associated with mode shape ϕ_k.

Finally, we expand the kinetic and potential energies in terms of Eq. (6) and apply Lagrange's equation to determine the equation of motion governing modal response q_k as follows:

$$\ddot{q}_k + 2\zeta_k\omega_k\dot{q} + \left[\omega_k^2 - (\Omega_x^2 + \Omega_y^2)\right] q_k = \dot{\boldsymbol{\Omega}} \cdot \mathbf{b}_\mathbf{k} - \Omega_z\, \boldsymbol{\Omega} \cdot \mathbf{a}_k + Q_k, \tag{9}$$

where $\mathbf{a}_\mathbf{k}$, $\mathbf{b}_\mathbf{k}$ are constant vectors related to the position of the inertial force center of the kth vibration mode defined by

$$\mathbf{a}_k = \int_m \phi_k (x\,\mathbf{e}_x + y\,\mathbf{e}_y)\, dm, \tag{10}$$

$$\mathbf{b}_k = \int_m \phi_k (-y\,\mathbf{e}_x + x\,\mathbf{e}_y)\, dm. \tag{11}$$

The first term in the equation of motion is the modal acceleration. The second term is an empirical viscous damping term, where ζ_k is the wing's kth modal damping ratio. The third term is a time-varying stiffness term dependent on the wing's angular velocity. The modal excitation terms to the right-hand side of the equation of motion are the Euler force, the centrifugal force, and the kth non-conservative aerodynamic force Q_k. Non-conservative aerodynamic modal force Q_k can be determined via the principle of virtual work as follows:

$$Q_k = \int_{S_w} dF_z(x,y,t)\phi_k(x,y)\, dS_w, \tag{12}$$

Physics of Fluids ARTICLE scitation.org/journal/phf

where dF_z is the differential aerodynamic force acting in the z direction and S_w is the wing's surface. The physical aerodynamic force F_z can be determined via any fluid model, including DBET and UVLM.

Finally, we determine the inertial moments $\mathbf{M}_0$ acting at the wing's point of rotation O. The inertial moments are needed to calculate the instantaneous power delivered to the flapping wing. We use a derivation from,[13] which derives $\mathbf{M}_0$ starting from angular momentum $\mathbf{H_0}$. The angular momentum of a rotating, flexible wing is

$$\mathbf{H}_0 = \int_m \mathbf{R} \times \dot{\mathbf{R}}\, dm, \tag{13}$$

which can be expanded via the wing's mode shapes and modal responses as follows:

$$\mathbf{H}_0 = \mathbf{I}_0\boldsymbol{\Omega} + \sum_{k=1}^{\infty}\left[-q_k(\mathbf{a}_k \cdot \boldsymbol{\Omega})\mathbf{e}_z - \mathbf{b}_k\dot{q}_k - (\mathbf{e}_z \cdot \boldsymbol{\Omega})\mathbf{a}_k q_k + (\boldsymbol{\Omega} - \omega_z\mathbf{e}_z)q_k^2\right], \tag{14}$$

with $\mathbf{I}_0$ being the inertial tensor of the wing. The inertial moments about fixed point O can then be determined by differentiating angular momentum $\mathbf{H}_0$ with respect to time, yielding

$$\mathbf{M}_0 = \boldsymbol{\Omega} \times \mathbf{H}_0 + \dot{\mathbf{H}}_{0,xyz}. \tag{15}$$

2. Deformable blade element theory

Blade element theory (BET) is a quasi-static modeling approach that is used frequently to estimate the aerodynamic forces and moments acting on flapping wings.[38,45,46] BET is usually formulated via multiple sets of algebraic equations and is thus computationally efficient. On the other hand, BET has several limitations; it neglects spanwise flows, vortex shedding, wing–wake interactions, and other phenomena that rely on the time history of the surrounding fluid. Further, BET does not provide information about the spatial force distribution acting over the wing. Nonetheless, BET provides order-of-magnitude propulsive force estimates and has been applied extensively to describe the aerodynamics of rigid wings. In the present work, we expand the BET approach to accommodate wing deformation. We refer to this framework as deformable blade element theory (DBET). We neglect added mass and rotational lift terms, which are included in some BET formulations.

A quasi-static differential aerodynamic force dF acting on an airfoil (Fig. 2) is described by

$$dF_{[\cdot]} = \frac{1}{2}\rho_f C_{[\cdot]}(\mathcal{A})\mathbf{V}_\infty \cdot \mathbf{V}_\infty\, dS, \tag{16}$$

where ρ_f is fluid density, $\mathbf{V}_\infty$ is the induced or free stream velocity, $C_{[\cdot]}$ is an aerodynamic coefficient ($[\cdot]$ is a placeholder to indicate either lift or drag) dependent on angle of attack $\mathcal{A}$, and dS is the differential surface over which the differential aerodynamic force acts. Assuming the wing flaps in a quiescent environment, the induced fluid velocity is equal in magnitude and opposite in direction to the wing's velocity, or $\mathbf{V}_\infty = -\dot{\mathbf{R}}$. Then, the differential surface can be described by $dS = c(y)dy$, where $c(y)$ is the wing's chord dependent on location

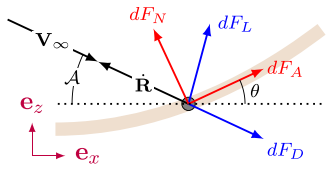

FIG. 2. Free-body diagram showing differential aerodynamic forces acting upon an individual blade element.

along the wing span y and dy is the blade element's width. We assume lift and drag coefficients of the form from[38] as follows:

$$C_P(\mathcal{A}) = C_P \sin(\mathcal{A})\cos(\mathcal{A}), \tag{17}$$

$$C_D(\mathcal{A}) = C_P \sin(\mathcal{A})^2 + C_{D,0}, \tag{18}$$

where C_P and $C_{D,0}$ are empirical aerodynamic coefficients. $C_{D,0}$ represents the drag the wing experiences at zero angle of attack. Since the wing is infinitely thin, this term effectively scales the total shear load acting over the wing's surface. The angle of attack $\mathcal{A}$ is defined as the angle between the wing's velocity vector and the x axis and is calculated via

$$\mathcal{A} = \tan^{-1}\left(\frac{\dot{\mathbf{R}} \cdot \mathbf{e}_z}{\dot{\mathbf{R}} \cdot \mathbf{e}_x}\right). \tag{19}$$

Drag acts collinear to the wing's velocity vector and lift acts orthogonal to drag. Differential lift and drag components dF_L and dF_D must be rotated by $\mathcal{A}$ to determine the differential aerodynamic forces acting normal to the deformed wing dF_N and axial to the deformed wing dF_A. This transformation is given by

$$dF_N = dF_D\cos(\mathcal{A}) + dF_L\sin(\mathcal{A}), \tag{20}$$

$$dF_A = -dF_D\cos(\mathcal{A}) + dF_L\sin(\mathcal{A}). \tag{21}$$

The normal and axial forces do not coincide with the wing's x–z coordinate basis (Fig. 2). To determine the aerodynamic forces acting in the x and z directions, the normal and axial forces must be rotated by the wing's local angle of rotation θ, where θ arises from wing deformation.

3. Quasi three dimensional unsteady vortex lattice method

The unsteady vortex lattice method (UVLM) is an established method, described in detail by Katz and Plotkin.[47] It is a potential flow method governed by

$$\nabla^2\boldsymbol{\Phi} = 0, \tag{22}$$

where $\boldsymbol{\Phi}$ is the velocity potential. As such, the fluid is considered incompressible throughout and irrotational except on the surface of the wing and in the wake. Viscous forces are ignored.

The wing is divided spanwise into multiple blades, each with a constant chord length. The aerodynamic loads on each blade are determined using a 2D UVLM solver. The blade is divided chordwise into panels. Each panel has a bound vortex attached at the quarter-chord and a control point at three-quarters-chord (Fig. 3).

Physics of Fluids ARTICLE scitation.org/journal/phf

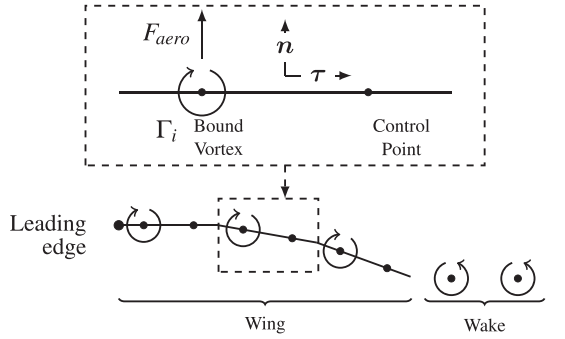

FIG. 3. Panel discretization used by the 2D UVLM solver.

Additionally, the trailing-edge panel sheds free wake vortices which are convected with the flow. Each vortex induces a tangential velocity field around it, described by the Biot–Savart law,

$$\boldsymbol{V}_{\text{ind}} = \frac{\Gamma_j}{2\pi}\frac{(r_{i,z}-r_{j,z})\mathbf{e}_x + (r_{j,x}-r_{i,x})\mathbf{e}_z}{|\boldsymbol{r_i}\text{-}\boldsymbol{r_j}|^2}, \tag{23}$$

where $\boldsymbol{V}_{\text{ind}}$ is the velocity at some point $\boldsymbol{r_i}$ induced by a vortex located at $\boldsymbol{r_j}$, and Γ_j is the vortex strength. This results in a singularity; as r gets smaller, the induced velocity becomes unreasonably large. To remedy this, a cutoff radius r_{co} is defined so that within this radius, the induced velocity decreases linearly as separation decreases, and the induced velocity function becomes

$$\begin{aligned}\boldsymbol{V}_{\text{ind}} &= \frac{\Gamma_j}{2\pi}\frac{(r_{i,z}-r_{j,z})\mathbf{e}_x + (r_{j,x}-r_{i,x})\mathbf{e}_z}{|\boldsymbol{r_i}\text{-}\boldsymbol{r_j}|^2}; \quad |\boldsymbol{r_i}\text{-}\boldsymbol{r_j}| > r_{co},\\ \boldsymbol{V}_{\text{ind}} &= \frac{\Gamma_j}{2\pi}\frac{(r_{i,z}-r_{j,z})\mathbf{e}_x + (r_{j,x}-r_{i,x})\mathbf{e}_z}{r_{co}^2}; \quad |\boldsymbol{r_i}\text{-}\boldsymbol{r_j}| \le r_{co}.\end{aligned} \tag{24}$$

At each time step, the strengths of the bound vortices on the wing as well as the newly shed wake vortex are found by enforcing the non-penetration condition; the wing is a solid barrier through which the fluid is unable to flow. This means the fluid can only move across the surface, and the velocity component normal to the wing surface is zero, stipulated by

$$\boldsymbol{V}\cdot\mathbf{n} = 0, \tag{25}$$

where $\boldsymbol{n}$ is the surface-normal vector on the wing and the flow velocity $\boldsymbol{V}$ is in a wing-fixed frame of reference. When this condition is enforced at the control point of each wing panel, this takes the form

$$\begin{bmatrix} a_{1,1} & a_{1,2} & \cdots & a_{1,N_p} & a_{1,N_p+1} \\ a_{2,1} & a_{2,2} & \cdots & a_{2,N_p} & a_{2,N_p+1} \\ \vdots & \vdots & \ddots & \vdots & \vdots \\ a_{N_p,1} & a_{N_p,2} & \cdots & a_{N_p,N_p} & a_{N_p,N_p+1} \\ 1 & 1 & \cdots & 1 & 1 \end{bmatrix} \begin{Bmatrix} \Gamma_1 \\ \Gamma_2 \\ \vdots \\ \Gamma_{N_p} \\ \Gamma_{W_1} \end{Bmatrix} = \begin{Bmatrix} rhs_1 \\ rhs_2 \\ \vdots \\ rhs_{N_p} \\ rhs* \end{Bmatrix}, \tag{26}$$

where aerodynamic influence coefficient $a_{i,j}$ is the surface-normal velocity induced at the control point of panel i by a unit strength vortex on panel j. rhs_i is the total surface-normal velocity at the ith control point due to all other sources—rigid body kinematics, wing deformation, and wake vortices, and rhs^* is the total bound vorticity on the wing. $\Gamma_{1\ldots N_p}$ is the bound vortex strength of the corresponding panel and Γ_{W_1} is the strength of the newly shed wake vortex, equal to the change in total bound vorticity over the wing from the previous time step. The free wake vortices are massless, and follow the local flow velocity induced by the wing bound vortices and other wake vortices as determined from Eq. (23). The pressure jump at the ith panel is found using the unsteady Bernoulli equation[47]

$$\Delta P_i = -\rho_f\left[(-\dot{\boldsymbol{R}}_{\boldsymbol{i}} + \boldsymbol{V}_{ind,i})\cdot\boldsymbol{\tau}_i\frac{\Gamma_i}{ds} + \frac{\partial}{\partial t}\sum_{j=1}^{i}\Gamma_j\right], \tag{27}$$

where ΔP_i is the pressure jump across the ith panel, $\dot{\boldsymbol{R}}_{\boldsymbol{i}}$ is the velocity of the panel ith in the inertial reference frame arising from the rigid body kinematics and the wing deformation, $\boldsymbol{V}_{ind,i}$ is the velocity induced by the ith bound and wake vortices, $\boldsymbol{\tau}$ is the panel surface-tangent vector, and ds is the panel length. The first term on the right-hand side describes the pressure resulting from quasi-steady aerodynamic forces such as lift and drag. The second term accounts for the pressure due to added mass, where the summation is from the leading edge to the ith panel. The aerodynamic force on each panel acts normal to the surface, and the total force on each blade is obtained by summing the x and z components of the panel forces.

C. High-fidelity computational model

Computational fluid dynamics (CFD) is a common approach to solving the Navier–Stokes equations across a discretized domain. These equations are derived from continuum mechanics and serve to maintain conservation of mass and momentum, and are accepted in the engineering community to encompass most physics pertinent to modeling a fluid domain. Finite element analysis (FEA) is a method for modeling the deformations and stresses throughout structures across a wide range of geometry, material properties, and composite assemblies. To build a two-way coupled model to use as a validation tool for the ROMs, we interface a CFD model using Siemens' Star-CCM+ (v15.04.008) to an FEA model using Dassault Systèmes Abaqus 2019 (6.19-1). Communication between the two commercial packages is handled through SIMULIA Co-simulation Engine (CSE).

For a reduction in computational expense, the CFD model uses a Spalart–Allmaras (SA) closure model in a Reynolds-averaged Navier–Stokes (RANS) scheme. RANS models are used throughout turbulent flow research, and the SA was chosen for its efficiency as a one-equation model as well as its previous use in studying flapping wing aerodynamics.[48,49] This modeling technique was used to calculate the pressure across the wing's surface as influenced by the entire flow field. To resolve this flow field accurately without remeshing the entire fluid domain at each time step, we used a Chimera mesh approach to keep a consistent discretization around the rotating wing.[50] This allows for a finely discretized region surrounding the wing (the *overset* mesh) to move with prescribed kinematics while the surround fluid domain discretization (the *background* mesh) remains motionless (Fig. 4). At each time step, the overset mesh region is cut from the background mesh, and overlapping cells along the edges of the overset region are used to interpolate data between the two meshes,

Physics of Fluids ARTICLE scitation.org/journal/phf

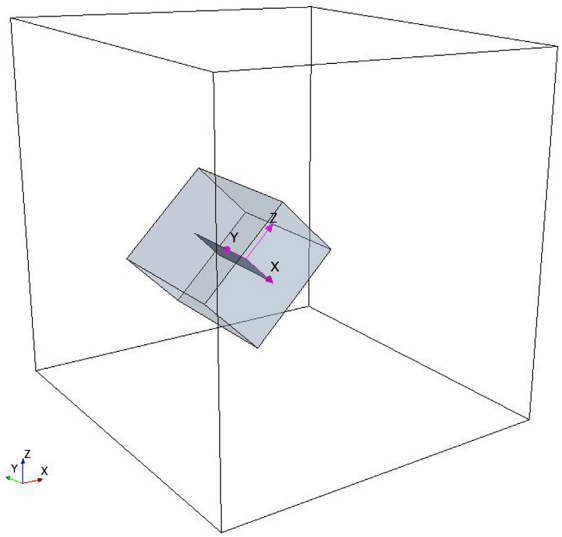

FIG. 4. Background mesh (outlined) and overset mesh (light gray) of the fluid domain in Star-CCM+. The rectangular wing is seen in the dark gray within the overset mesh. The wing-fixed coordinate system is shown in pink, with an origin at the wing root's leading edge. The background mesh must be large enough to accommodate flapping kinematics and encompass pertinant flow features, while the overset mesh must accommodate the out-of-plane deformation of the wing.

thereby maintaining the conservation of mass and momentum. A radial basis function (RBF) mesh morphing algorithm is also applied to the overset mesh, allowing these cells and the overset region boundary to stretch and compress to accommodate the deformation of the wing as calculated in FEA.

The deformations calculated in FEA are influenced by the centrifugal and Euler forces associated with flapping motions as well as the aerodynamic forces calculated by CFD at every time step. We applied the flapping kinematics by imposing angular velocity-dependent boundary conditions at the wing's fixed point of rotation. Abaqus' implicit solver was then used to resolve deformations, which were in turn sent back to CFD.

The communication between FEA and CFD facilitated by SIMULIA CSE allowed us to capture aeroelastic interactions through bilateral coupling, as data are transferred between both software at every time step specified in CFD (Fig. 5). After CFD initializes the motionless fluid domain, kinematics are applied in FEA, and deformations due to inertial and centrifugal forces are resolved. Abaqus uses a dynamic time step to allow for a converged structural solution at each time step, but when the time step specified in CFD has been reached, the new wing geometry is sent to Star-CCM+ CFD in the inertial and wing-fixed frames. This change in geometry is then interpreted as movement of the wing boundary in CFD caused by both the rotation and deformation. Next, the overset mesh region is rotated by the flapping kinematics, and then is morphed based on the wing deformations. Finally, the entire fluid domain in CFD is resolved, and the resulting distribution of aerodynamic forces is sent back to Abaqus FEA. In FEA, the process continues, now adding the aerodynamic forces into the calculation of wing deformation. This cycle continues until a user-specified solution time is reached.

The HiFi model makes minimal assumptions about insignificant physics parameters aside from those associated with the influence of turbulence on the fluid domain as modeled with the SA RANS model. This allows the HiFi model to capture some of the physics that the ROMs ignore, such as spanwise flow which is clearly resolved by the three-dimensional application of the Navier–Stokes equations, and the influence of added mass which is captured through the acceleration term of the conservation of momentum.

III. NUMERICAL SIMULATION PARAMETERS

We now establish the simulation parameters necessary to implement and compare the HiFi model and ROMs. We investigate a thin, homogeneous rectangular wing with flapping kinematics idealized from those of a flying insect. We consider three modulus values (flexible, medium, and stiff hereafter) to explore the influence of flexibility on deflection and aerodynamic forces/moments. The wing is assumed to have a rigid leading edge. All rotations are assumed harmonic.

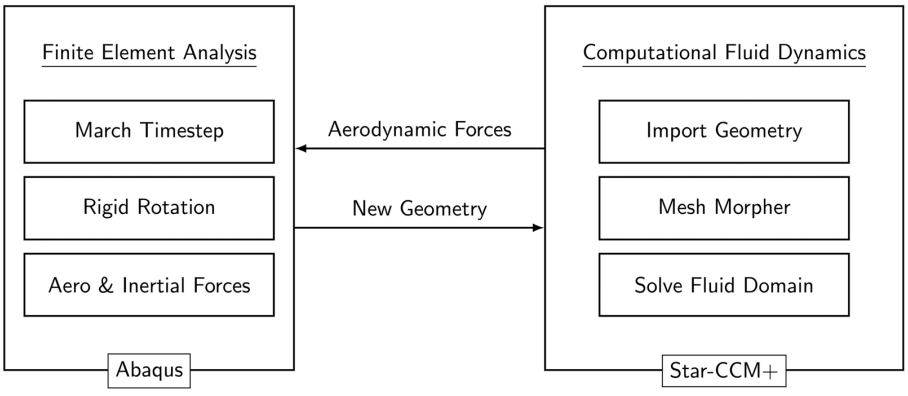

FIG. 5. Bilaterally coupled workflow between Abaqus FEA and Star-CCM+ CFD. This cycle continues at every time step described by CFD.

Physics of Fluids ARTICLE scitation.org/journal/phf

TABLE I. Wing parameters.

Variable	Description	Value	Unit
L	Wing span	5	cm
c	Wing chord	2	cm
t	Wing thickness	0.17	mm
α_0	Roll amplitude	60	°
β_0	Pitch amplitude	45	°
γ_0	Yaw amplitude	0	°
⋯	Pitch phase	90	°
f	Flap frequency	10	Hz
ρ	Material density	235.5	kg m^{-3}
E	Elastic modulus	(Flexible) 7.3×10^7	Pa
		(Normal) 1.365×10^8	Pa
		(Stiff) 2.4×10^8	Pa
Re	Reynold's number	4400	⋯

The wing flaps about a stationary point in a quiescent environment, which is most representative of hovering flight. Wing parameters are summarized in Table I, and the geometry is shown in Fig. 6. Wing morphology and flapping kinematics are based roughly on the forewing of the monarch butterfly.[51]

The structural model used in DBET and UVLM ROMs [Eq. (9)] is fully defined by flapping kinematics, wing mode shapes ϕ_k, natural frequencies ω_k, damping ratios ζ_k, and the non-conservative load Q_k. We use a numerical modal analysis implemented via Abaqus to calculate ϕ_k and ω_k. The finite element model used for modal analysis is identical to that used for dynamic simulation in the HiFi model, with the primary difference residing in the solution procedure (finite element details are discussed with HiFi model parameters). Practically, we retain two vibration modes (Fig. 6) for the structural solver, which have natural frequencies ($\omega_1 = 40$ Hz, $\omega_2 = 52.2$ Hz) for the flexible wing, ($\omega_1 = 55$ Hz, $\omega_2 = 74.6$ Hz) for the medium wing and ($\omega_1 = 73$ Hz, $\omega_2 = 99$ Hz) for the stiff wing. Damping ratio ζ_k is set to 5% for both vibration modes. The structural model is solved using MATLAB (V2021b) "ode45" at time steps dictated by the DBET and UVLM ROMs.

Simulation parameters for the DBET and UVLM models are summarized in Table II. The DBET model requires empirical aerodynamic coefficients and reference locations for the angle of attack and where aerodynamic forces are assumed to act. We use aerodynamic coefficients in proximity to the values used in Ref. 38. The angle of attack is referenced from the three quarter chord and aerodynamic forces act at the quarter chord. The wing must be broken into ten blade elements for maximum wing deformation and mean force in the $-X$ direction (opposite of gravity, Fig. 1) to converge. The UVLM model requires the wing to be discretized into blades and both the wing and wake must be discretized into bound and shed vortices. The values for panel count, wake count and time step were determined based on convergence studies for a previous 2D model.[52] On each panel, the bound vortex is placed one quarter chord back from the leading edge and the control point is at three quarter chords from the leading edge. The cutoff radius is selected such that results largely match those found without a cutoff, except that large transient spikes should be reduced. Both models are coded in MATLAB (V2021b).

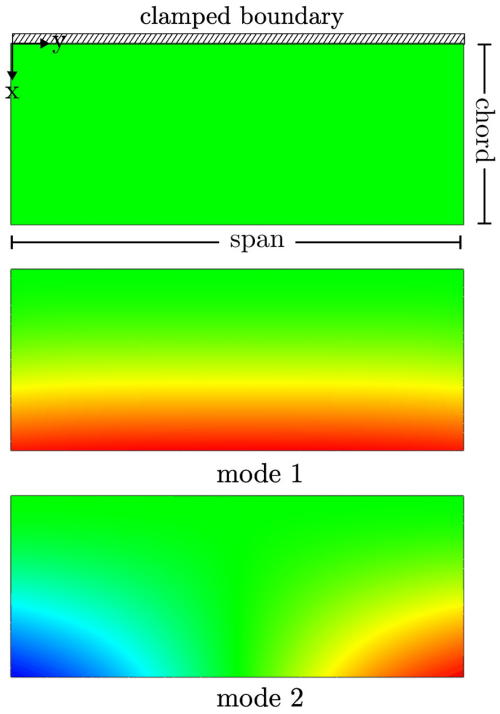

FIG. 6. Geometry and vibration modes of the rectangular wing used in numerical simulation. The first mode represents a chordwise-bending mode, and the second represents a chord-wise torsional mode. Red indicates positive out-of-plane motion, green indicates no motion and black indicates negative out-of-plane motion. Mode shapes are arbitrary in magnitude, which is why a colorbar is omitted.

Parameters for the HiFi model are summarized in Table III. The CFD domain size was chosen with sufficient distance behind the wing's trailing edge and away from the wing's tip to capture flow structures releasing from the wing that could affect the transient fluid forces acting on the wing. The overset mesh size was chosen to capture the

TABLE II. DBET and UVLM simulation parameters.

Variable	Description	Value	Unit
DBET			
C_P	Pressure coefficient	2.9	⋯
$C_{D,0}$	Drag offset coefficient	0.1	⋯
N_s	Number of blades	10	⋯
N_t	Steps-per-wingbeat	100	⋯
UVLM			
N_s	Number of blades	20	⋯
N_p	Number of panels-per-blade	20	⋯
N_w	Number of wake vortices	100	⋯
N_t	Steps-per-wingbeat	200	⋯
r_{co}	Cutoff radius	$0.25c$	cm

Physics of Fluids ARTICLE scitation.org/journal/phf

TABLE III. High-fidelity modeling parameters.

Variable	Description	Value	Unit
Computational fluid dynamics			
μ	Dynamic viscosity of air	1.86×10^{-5}	Pa s
ρ	Density of air	1.18	kg m^{-3}
⋯	Domain dimensions	$0.19 \times 0.21 \times 0.2$	m
⋯	Overset dimensions	$0.04 \times 0.08 \times 0.06$	M
⋯	Mean element length (domain)	1.2	mm
⋯	Mean element length (overset)	0.6	mm
⋯	Total number of elements	3 319 937	⋯
⋯	Prism layers	5	⋯
⋯	Prism layer growth rate	1.5	⋯
Δt	Timestep	0.001	s
Finite element analysis			
⋯	Element type	S4R	⋯
α	Raleigh damping factor	(Flexible) 14.472	⋯
		(Normal) 19.858	⋯
		(Stiff) 26.344	⋯
⋯	Number of nodes	1071	⋯
⋯	Shell thickness	0.17	mm
⋯	Number of shell element integration points	5	⋯
Δt_{min}	Minimum automatic timestep	1×10^{-6}	s
Δt_{max}	Maximum automatic timestep	0.001	s

flow structures immediately surrounding the wing with higher resolution and to allow for large wing deformations without over-compression or elongation of any elements by the mesh morpher. An earlier study involving single degree of freedom flapping of a rigid wing with identical geometry revealed converged results with 1.2-mm-sized elements in the domain region and 0.6-mm elements in the overset region.[53] Within the same study, we determined an adequate time step for solution convergence was 0.001 s. At each time step, 25 inner iterations were used to resolve the Navier–Stokes equations, based on convergence of the model residuals. These meshing and time-stepping studies were performed with a rigid wing, so mesh refinement was increased modestly to account for the additional motion of the wing's deflection.

The finite element structural model was comprised of 1000 four-node quadrilateral (S4R) shell elements (1071 nodes), which was sufficient for the wing's first two natural frequencies to converge. We used an automated dynamic time step within FEA, where the minimum time step used was 1×10^{-6} s and the maximum time step was 0.001 s when deformation data were saved and passed to Star-CCM+ CFD. The wing was modeled with a rigid leading edge by applying kinematic constraints to all nodes along this edge to a control point at the wing's point of rotation *O*. At *O*, angular velocity boundary conditions were applied to prescribe the flapping kinematics which the entire leading edge rigidly followed. We use a Rayleigh damping model and select Rayleigh damping factor α such that the first two vibration modes have a damping ratio of 5%, consistent with the ROMs.

IV. RESULTS

Across all models and wing stiffness values considered, we compared wing deformation, aerodynamic forces in the inertial and wing-fixed reference frames, and total moments in the wing reference frame. Wing deformation was compared on the trailing edge at the wing root and wing tip (Fig. 7). In general, the agreement between all models is acceptable. In the most flexible case, the wingtip deflected about 5–5.5 mm, or 25% of the chord length. Maximum deflections predicted by each model are similar, with the ULVM over-predicting the peak value by about 10% compared to the HiFi model. Since both DBET and UVLM ROMs rely on the same structural solver, the difference in response amplitude must stem from differences in fluid loading. The UVLM induces greater deflection, possibly due to an added mass force that is absent from the DBET model. ROM error decreases as the wing becomes stiffer and deformations are reduced. All models indicated that the wing root experienced lower deflections than wing tip (maximally 3.5–4 mm), likely because of increased aerodynamic loading near the wingtip. Aerodynamic loads generally increase along the span (unless in close proximity to the wingtip, where pressure losses occur) due to increasing velocity. The difference in deformation between wingroot and wingtip indicates at least two vibration modes (Fig. 6) are excited during flapping. If deformation was dominated by the first mode, wing deformation would vary only from leading edge to trailing edge and would be nearly uniform from root to tip. At both wingtip and root, deformation occurred at the primary flapping frequency with lower harmonics at three times the flapping frequency superimposed on the response. The primary response from the HiFi model leads that of UVLM, which in turn leads the DBET model. The deformation time lag observed in the ROMs stems from a lag in aerodynamic loading relative to the HiFi model.

To better compare full-field deformation, we generated a contour plot of wing deformation at 1/8 intervals of a single wingbeat. Figure 8

Physics of Fluids ARTICLE scitation.org/journal/phf

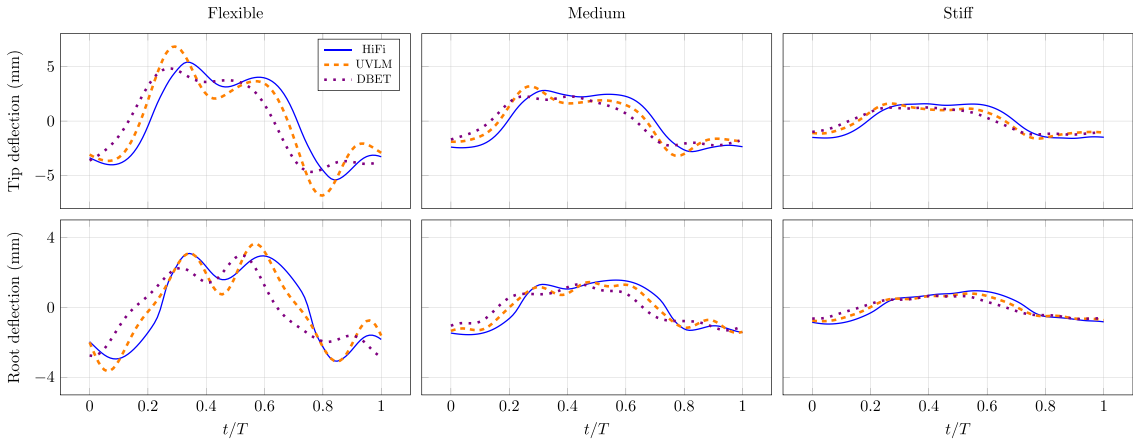

FIG. 7. Deflection of the wing's trailing edge at tip and root locations along the wing's span.

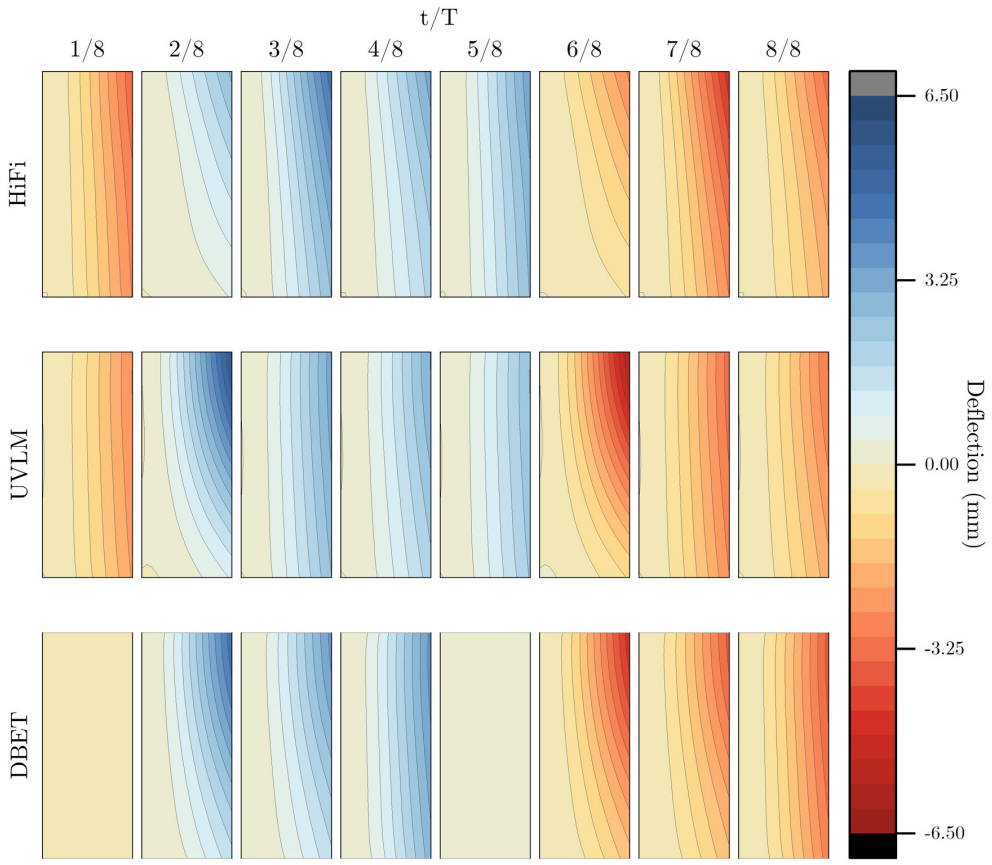

FIG. 8. Contour map showing out-of-plane deformation of the flexible wing as a function of wingbeat period *T*.

Physics of Fluids ARTICLE scitation.org/journal/phf

shows the out-of-plane deflection predicted by each model for the flexible wing, which is the worst-case scenario in terms of model agreement since the ROMs more closely agree with the HiFi model at smaller deflections (Fig. 7). At most intervals, the deflection contour matches fairly well. Noticeably, DBET indicates near zero deflection at $T/8$ and $5T/8$, whereas the UVLM and HiFI models show non-zero contour profiles. This discrepancy occurs due to the time-lag between DBET and HiFI deflections. Those instances aside, these results suggest that the structural model employed by the ROMs captures deformation profiles reasonably well with only two vibration modes retained, at least for this wing design. As discussed previously, the largest deformation occurs near the wing tip while the root experienced lower deformation by comparison.

Aerodynamic forces with respect to the wing fixed reference frame are shown in Fig. 9. For all wing stiffnesses, the predominate forces act in the wing z direction. For the most flexible case, the absolute peak forces predicted via the HiFi model are about 4, 1, and 0.2 mN in the wing z, x, and y directions, respectively. F_z agrees well across all models. UVLM and CFD produce nearly identical results, while DBET indicates a slight phase lag and lower amplitude in F_z. All models show that F_z increases with wing stiffness, likely because the wing's normal vectors remain more closely aligned with z at lower deflections. The agreement between ROMs and HiFi models is not as strong within the wing-fixed x direction, due in part to differences in how shear is accounted for. The UVLM entirely lacks shear loads, leading to it underestimate F_x compared to CFD and DBET for stiffer wings. The difference is primarily in force amplitude, as the general waveforms agree reasonably well. The agreement is better for more flexible wings, where a larger percentage of F_x stems from pressure loading. DBET produces similar F_x from mid-stroke to stroke reversal ($t/T = 0$ to $t/T = 0.25$) for all wing stiffnesses, but force profile then diverges until next mid-stroke at $t/T = 0.5$. All three models predict a reduction in F_x as the wing is made stiffer, which is opposite to the trend observed in F_z. This is because at larger deflections, the wing's normal vectors have a larger component in the wing's x direction. Due to the lack of spanwise flow, neither DBET nor UVLM are well-positioned to estimate F_y; they are therefore omitted from Fig. 9. Nonetheless, the HiFi model shows the forces in y are considerably lower than the other two force components, and thus we believe it is reasonable to neglect them in ROM efforts.

We next look at total moments at point of rotation O in the wing fixed frame, where the total moments are the inertial moments less the aerodynamic moments (Fig. 10). M_x generally agrees across all three models and at each level of flexibility, though there is a phase discrepancy which may introduce error when calculating quantities from moments such as mechanical power. Moments M_y and M_z also agree well in magnitude across the models, but the phase lag of UVLM and DBET predictions with respect to HiFI predictions is more pronounced. The largest error occurs in M_z of the stiffest wing, which is influenced by the wing's F_x and F_y forces. This error likely occurs because neither DBET and UVLM models are capable of resolving F_y, and the UVLM model does not account for shear, thus leading to poor predictions of F_x for stiff wings (Fig. 9). Nonetheless, because the total moments are in large part driven by inertia, minor discrepancies between aerodynamic moments are not manifested as large discrepancies in the total moments.

We now compare aerodynamic forces with respect to the inertial frame, which is of practical importance because a flapping wing insect must produce sufficient lift to stay aloft during hover. Aerodynamic forces in the inertial frame generally shows close agreement between models (Fig. 11). The HiFi model and ROMs estimate lift forces F_X (recall that gravity is aligned in the $+X$ direction, Fig. 1) that are

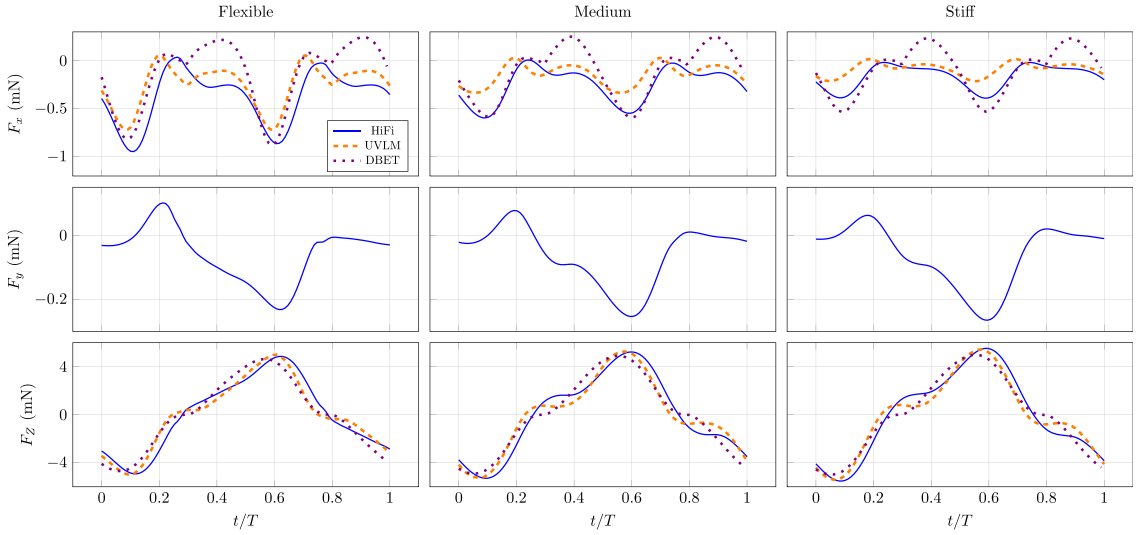

FIG. 9. Aerodynamic forces predicted by each model with respect to the wing-fixed reference frame. UVLM and DBET models do not resolve spanwise flow, so no F_y component is shown for these models.

Physics of Fluids ARTICLE scitation.org/journal/phf

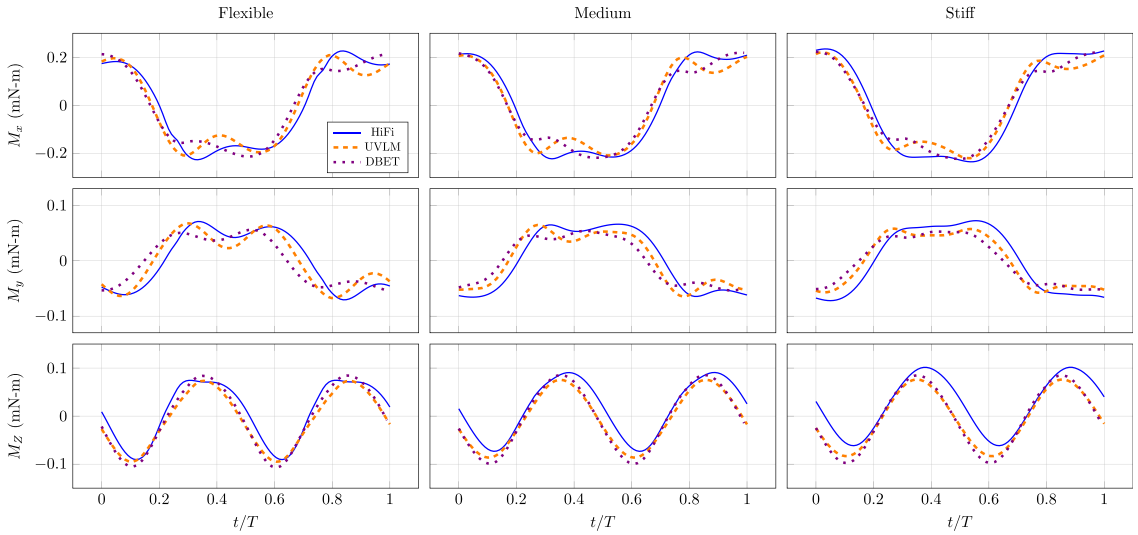

FIG. 10. Aerodynamic moments predicted by each model with respect to the wing-fixed reference frame.

similar in timing and magnitude for each wing stiffness considered. The largest difference in F_X between ROMs and the HiFi model occurs near $t/T = 0.3$, shortly after stroke reversal. This is during the portion of the wing beat when the highest acceleration and wing deflection occur, so this dissimilarity may relate to the differences in how the added mass force is calculated (or in the case of DBET, the lack of added mass). None of the models indicate an increase in lift with wing flexibility; in fact, the more flexible wing produces less lift relative to the stiff wing, though possibly with less input power (see Sec. IV A). The inertial-frame force F_Z is the largest force component in magnitude and agrees well across each model. Similar to wing fixed F_z, world frame F_Z increases with wing stiffness as well. Model agreement is somewhat worse for F_Y, again because neither of the ROMs can accommodate spanwise forces within the wing-fixed frame.

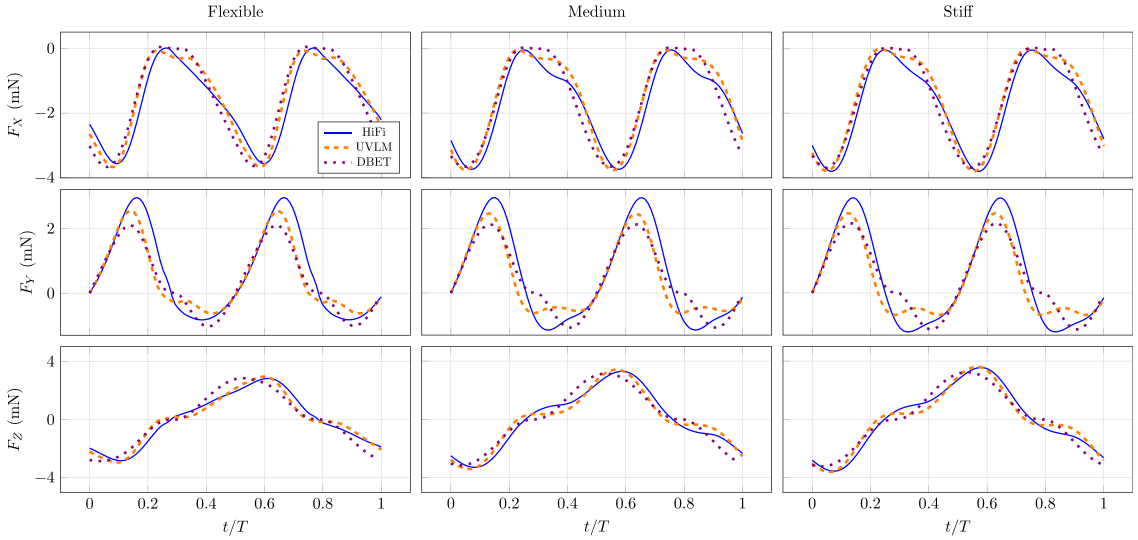

FIG. 11. Aerodynamic forces predicted by each model with respect to the inertial reference frame. Gravity acts in the $+X$ direction.

Physics of Fluids ARTICLE scitation.org/journal/phf

A. Parametric study

Finally, we perform a parametric study to demonstrate the computational efficiency of the ROMs in exploring wide parameter spaces. We aim to determine how wing stiffness (characterized by the wing's first natural frequency) and mass affect peak deflection, mean lift, and average power at steady state. The average power $\bar{P}$ is calculated via

$$\bar{P} = \frac{1}{T}\int_0^T \mathbf{M}_{total} \cdot \mathbf{\Omega}\, dt, \tag{28}$$

where the total moments are defined by $M_{total} = \mathbf{M}_0 - \mathbf{M}_{aero}$. This expression for power assumes that negative power offsets positive power, or that potential energy is stored in the system and is later recycled to do work. The first natural frequency of the wing was swept from 30 to 100 Hz in 0.1 Hz increments, and we considered discrete wing masses of 40, 60, and 80 mg. Due to the limiting computation time of the high-fidelity model, only the three wing stiffness discussed previously were used in this study. The results are shown in Fig. 12.

As the wing's natural frequency increases, the deflection tends toward zero at a similar rate for all models. The closest agreement was for the 80 mg wing, where the inertial forces dominate the deflection more so than in the lighter wings. In this case, the CFD and DBET line up well at all points, and the UVLM shows only slightly higher wing deformation. As the wing mass increases, the wing deflections predicted by DBET and UVLM diverge, indicating that the differences in the fluid models are responsible for variability in deflection.

The mean lift estimated by CFD is roughly 10% higher than that of the reduced-order models. However, all models show the same general trend, where the wing produces more lift as it becomes more rigid. The lower lift estimated by UVLM may result from the lack of LEV, a feature which is believed to contribute significantly to force production in flapping wings.[54] The lower lift estimated by DBET stems from the aerodynamic coefficient C_P, which may be inflated to increase the lift curve. Wing mass did not have a considerable effect on mean lift.

UVLM and DBET produce nearly the same mean lift ($-F_X$) from the stiffest case all the way down to moderate levels of flexibility. At higher wing masses, the similarity persists for lower natural frequencies. As the natural frequency is reduced toward 30 Hz (three times the flapping frequency), the DBET and UVLM begin to diverge. However, at this level of compliance, the wing deformation is about 75% of the chord length, and the linear structural framework is likely unsatisfactory. Aerodynamic forces in this range should be interpreted with caution.

The last quantity examined is power consumption. All three methods show that more flexible wings require less power than stiffer wings, and that more massive wings require more power than lighter wings. UVLM and HiFi models show that power steadily decreases with natural frequency. DBET predicts less of a dependence on wing stiffness, though it does still decrease with natural frequency. CFD shows a much steeper relation between stiffness and power than either of the ROMs, perhaps because of shear that is unmodeled by the UVLM model and underestimated by the DBET model. Errors in power are also sensitive to the relative phase between total moments and angular velocity, the latter which is identical across all models. Thus, small errors in total moment phase (Fig. 10) may cause larger

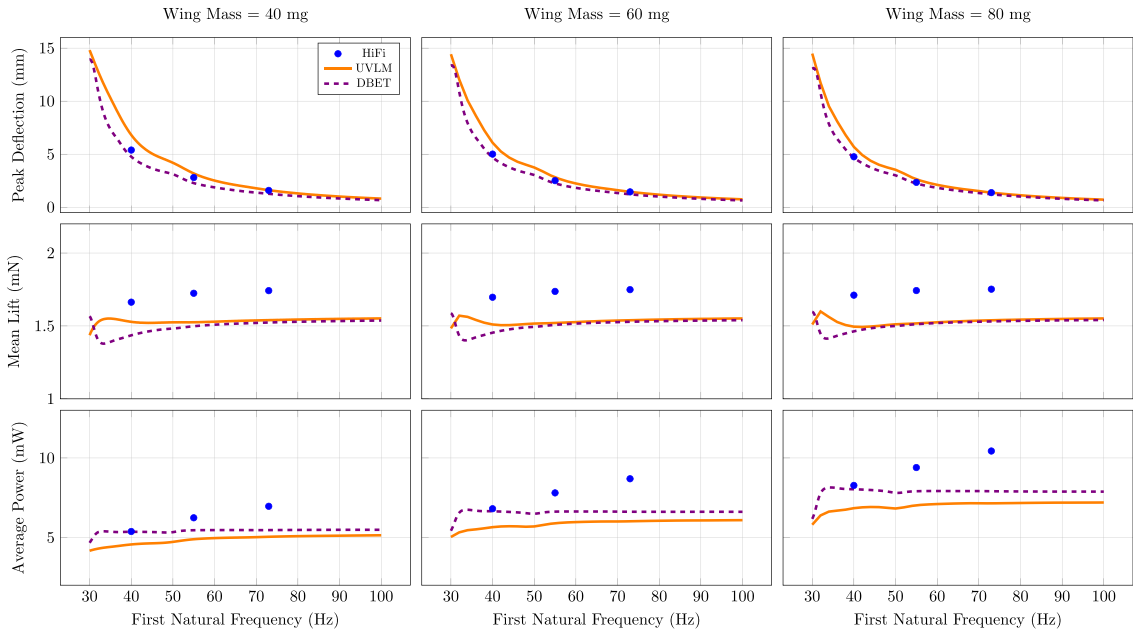

FIG. 12. Parameter study showing the effect of wing flexibility (parametrized by the wing's first natural frequency) and mass on peak deflection, mean lift, and average power. The corresponding time-series data for lift and deflection is shown for the 60 mg wing at natural frequencies of 40, 55, and 73 Hz in Figs. 7 and 11.

Physics of Fluids ARTICLE scitation.org/journal/phf

errors in power. Still, these studies support the idea that moderate wing flexibility can increase aerodynamic performance, and that the reduction in power consumption outweighs the reduction in lift.

V. DISCUSSION

Wing flexibility and deformation are essential to sensory function and aerodynamic performance in flapping wing insect flight. However, the high-order models used to evaluate flapping wing FSI usually require considerable computational resources, rendering them impractical for parameter studies that consider variable wing stiffness, morphology, or flapping kinematics. In this work, we present two quasi-3D ROMs capable of estimating wing deformation and the resulting aerodynamic forces and moments. Both ROMs rely on a modal truncation-based structural framework but differ in their fluid models. The first ROM uses an algebraic DBET fluid model, and the second ROM uses a UVLM approach. We applied the models to estimate the dynamics of a thin, flexible, rectangular plate with a rigid leading edge subject to rotational kinematics modeled after insect flapping. We compared wing deformation, aerodynamic forces, and total moments predicted by the ROMs to those determined by more conventional HiFi modeling. Both ROMs predicted wing deformation with good accuracy, even when deflections were as large as 25% of the chord length. The ROMs resolved predominate aerodynamic forcing in wing-fixed and inertial reference frames fairly well, but were less accurate in resolving the smaller forces acting in the wing's x–y plane. We then performed a parametric study to demonstrate the influence of wing mass and stiffness on wing deflection, average lift, and average power. The ROMs predicted peak deflection and mean lift fairly well, but had larger discrepancies in average power for stiffer wings. In the following, we discuss the relevance of these ROMs within the study of flapping wing FSI.

A. Computational efficiency

Overall, the computational savings conferred by the two ROMs render them useful tools for studies that require exploration of broad parameter spaces. Direct computational modeling is computationally intensive—within CFD, resolving only the conservation of mass, conservation of momentum, and closure model equations for 25 iterations on each element yields nearly 250×10^6 equations to solve at every time step. Within FEA, the wing is treated as geometrically nonlinear and consequently each time step of analysis must be broken into smaller increments such that a particular solution path may be followed. Considering each node of an S4R element has six degrees-of-freedom, and the plate model has 1071 nodes, about 6×10^3 equations must be solved at each increment within the FEA solver. Thus, computational expense is the biggest motivator for reduced order modeling.

The ROMs were determined to be much faster at modeling bulk propulsive forces and wing deformation relative to the high-fidelity modeling approach. All simulations were performed on a desktop computer custom built for this HiFi setup. We used 10 threads of an intel i9–9900K processor operating with a 4.7 GHz clockspeed, with 64 GB of available DDR4 RAM. When comparing solution times for the flexible wing, the HiFi model resolves the aerodynamic forces and wing deformation in about 5.4 h per wingbeat, the UVLM model about 2.5 s per wingbeat, and the DBET model about 0.093 s per wingbeat. This results in 4 and 6 orders of magnitude in time savings for UVLM and DBET, respectively, demonstrating that ROMs hold value anytime that computational efficiency in needed. We show a practical parameter study where 2100 mass/flexibility combinations were simulated by the ROMs (Fig. 12), taking 7.3 h of computation time for UVLM and 16.3 min for DBET. To gather the same data using the HiFi model would have taken approximately 6.5 years.

B. Applications of ROMs

ROMs play an important role in the study of insect flight. Across species, insect wings have distinct morphological features and flapping kinematics that influence wing strain profiles, sensing and aerodynamic performance. The effect of morphology and flapping kinematics is difficult to fully address using HiFi models. Though ROMs have lower accuracy relative to direct computational approaches, they allow parameter spaces to be explored more effectively. HiFi modeling can then be used for a subset of conditions to ensure ROM accuracy.

Both of the ROMs presented in this work are general in the sense that they can accommodate arbitrary wing geometry, morphology and flapping kinematics. As discussed in Sec. II B 1, the reduced-order structural model is versatile because it can interface with modal-based finite element solvers. The ability to pre-compute mode shapes in FEA allows the user significant freedom and creativity in the geometry and structural domain to investigate the effects of a wide range of biological or engineering-inspired wing designs. Further, physical experimentation like scanning laser vibrometry could be used to compute mode shapes of biological wings,[40] allowing for deeper study of real insect wings. Any number of mode shapes can be included in the models when deemed appropriate. Practically, the number of modes retained generally corresponds to the modes with natural frequencies that fall within ten times that of the predominant excitation frequency.

C. ROM limitations

Despite the advantage of the flapping wing FSI ROMs, each has limitations that constrain their accuracy in some contexts. First, both the quasi-3D DBET and UVLM ROMs neglect spanwise flow. Spanwise flow is a critical for modeling effects like shed vortices from the wingtip that result in downwash and induced drag.[55] Without spanwise flow, it is not possible for fluid to wrap around the wingtip in any way. Quasi-3D approaches will consequently overestimate the fluid loading near the wingtip of a structure, which may in turn amplify the deformation of modes with large displacements near the wingtip. If the rigid leading edge assumption employed in this work were relaxed, this modeling error may result in a larger discrepancy between deformations estimated via ROMs and HiFi methods.

Second, both ROMs have limited capacity to describe chordwise pressure distributions. The DBET model provides no force distribution information and instead assumes all aerodynamic forces simply act at the quarter chord. The UVLM model provides some information regarding chordwise pressure variation, but has limited accuracy near the leading edge because the LEV is not explicitly modeled. The LEV is considered a major factor in lift generation.[54] The UVLM method assumes that flow is always attached to the wing until wake vortices are shed from the trailing edge. This means that wing motions at angles of attack that would normally induce stall without the LEV are modeled such that flow remains attached over the leading edge, thereby requiring particularly strong V_{ind} used in pressure calculations.

Consequently, we believe the LEV must be considered to improve chordwise pressure estimates.

Third, both ROMs provide limited or no information regarding the flow field surrounding the wing. The DBET model provides only bulk propulsive forces and moments. UVLM cannot resolve the entire fluid domain and, instead, is only tracking some flow features that are shed from the wing. These features are monitored for a user specified amount of time, which could be a cause of error in instances where flow features have a delayed interaction with the wing. This is potentially problematic when fluid flow causes a more spatially varying distribution of aerodynamic force.

These modeling limitations help define the scope and appropriate use these quasi-3D ROMs. While studies sensitive to changes in spanwise flow or spatial distribution of forces should perhaps be left to other methods, studies involving bulk aerodynamics and high computational efficiency benefit significantly. The 4 and 6 orders of magnitude time savings is a clear demonstration of why these models can be advantageous over conventional high-fidelity approaches in parameter studies.

ACKNOWLEDGMENTS

This research was supported the National Science Foundation under Award No. CBET-1855383 to M.J. Any opinions, findings, and conclusions or recommendations expressed in this material are those of the author(s) and do not necessarily reflect the views of the National Science Foundation.

AUTHOR DECLARATIONS

Conflict of Interest

The authors have no conflicts to disclose.

Author Contributions

R. Schwab and J. Reade contributed equally to this work.

Ryan Schwab: Formal analysis (equal); Investigation (equal); Methodology (equal); Software (equal); Validation (equal); Writing – original draft (equal); Writing – review & editing (equal). **Joseph Reade:** Formal analysis (equal); Investigation (equal); Methodology (equal); Software (equal); Validation (equal); Visualization (equal); Writing – original draft (equal); Writing – review & editing (equal). **Mark Jankauski:** Conceptualization (lead); Formal analysis (supporting); Funding acquisition (equal); Methodology (equal); Project administration (equal); Software (equal); Validation (equal); Visualization (equal); Writing – original draft (equal); Writing – review & editing (equal).

DATA AVAILABILITY

The data that support the findings of this study are available from the corresponding author upon reasonable request.

REFERENCES

[1]S. J. Huston and V. Jayaraman, "Studying sensorimotor integration in insects," Curr. Opin. Neurobiol. **21**, 527–534 (2011).
[2]B. H. Dickerson, J. L. Fox, and S. Sponberg, "Functional diversity from generic encoding in insect campaniform sensilla," Curr. Opin. Physiol. **19**, 194–203 (2021).
[3]W. Gnatzy, U. Grunert, and M. Bender, "Campaniform sensilla of *Calliphora vicina* (Insecta, Diptera)," Zoomorphology **106**, 312–319 (1987).
[4]S. P. Sane, A. Dieudonné, M. A. Willis, and T. L. Daniel, "Antennal mechanosensors mediate flight control in moths," Science **315**, 863–866 (2007).
[5]B. R. Aiello, K. E. Stanchak, A. I. Weber, T. Deora, S. Sponberg, and B. W. Brunton, "Spatial distribution of campaniform sensilla mechanosensors on wings: Form, function, and phylogeny," Curr. Opin. Insect Sci. **48**, 8–17 (2021).
[6]B. Pratt, T. Deora, T. Mohren, and T. Daniel, "Neural evidence supports a dual sensory-motor role for insect wings," Proc. R. Soc. B **284**, 20170969 (2017).
[7]B. H. Dickerson, Z. N. Aldworth, and T. L. Daniel, "Control of moth flight posture is mediated by wing mechanosensory feedback," J. Exp. Biol. **217**, 2301–2308 (2014).
[8]A. Eberle, B. Dickerson, P. Reinhall, and T. Daniel, "A new twist on gyroscopic sensing: Body rotations lead to torsion in flapping, flexing insect wings," J. R. Soc. Interface **12**, 20141088 (2015).
[9]B. T. Hinson and K. A. Morgansen, "Gyroscopic sensing in the wings of the hawkmoth *Manduca sexta*: The role of sensor location and directional sensitivity," Bioinspiration Biomimetics **10**, 056013 (2015).
[10]R. J. Wootton, "Support and deformability in insect wings," J. Zool. **193**, 447–468 (1981).
[11]T. Nakata and H. Liu, "A fluid–structure interaction model of insect flight with flexible wings," J. Comput. Phys. **231**, 1822–1847 (2012).
[12]S. A. Combes and T. L. Daniel, "Into thin air: Contributions of aerodynamic and inertial-elastic forces to wing bending in the hawkmoth *Manduca sexta*," J. Exp. Biol. **206**, 2999–3006 (2003).
[13]H. E. Reid, R. K. Schwab, M. Maxcer, R. K. D. Peterson, E. L. Johnson, and M. Jankauski, "Wing flexibility reduces the energetic requirements of insect flight," Bioinspiration Biomimetics **14**, 056007 (2019).
[14]S. Heathcote, Z. Wang, and I. Gursul, "Effect of spanwise flexibility on flapping wing propulsion," J. Fluids Struct. **24**, 183–199 (2008).
[15]M. Moore, "Analytical results on the role of flexibility in flapping propulsion," J. Fluid Mech. **757**, 599–612 (2014).
[16]N. Lee, S. Lee, H. Cho, and S. Shin, "Effect of flexibility on flapping wing characteristics in hover and forward flight," Comput. Fluids **173**, 111–117 (2018).
[17]B. Yin and H. Luo, "Effect of wing inertia on hovering performance of flexible flapping wings," Phys. Fluids **22**, 111902 (2010).
[18]M. Percin, Y. Hu, B. W. van Oudheusden, B. Remes, and F. Scarano, "Wing flexibility effects in clap-and-fling," Int. J. Micro Air Vehicles **3**, 217–227 (2011).
[19]F.-B. Tian, H. Dai, H. Luo, J. F. Doyle, and B. Rousseau, "Fluid–structure interaction involving large deformations: 3D simulations and applications to biological systems," J. Comput. Phys. **258**, 451–469 (2014).
[20]D. Ishihara, T. Horie, and M. Denda, "A two-dimensional computational study on the fluid–structure interaction cause of wing pitch changes in dipteran flapping flight," J. Exp. Biol. **212**, 1–21 (2009).
[21]M. Hamamoto, Y. Ohta, K. Hara, and T. Hisada, "Application of fluid–structure interaction analysis to flapping flight of insects with deformable wings," Adv. Rob. **21**, 1–21 (2007).
[22]T. Fitzgerald, M. Valdez, M. Vanella, E. Balaras, and B. Balachandran, "Flexible flapping systems: Computational investigations into fluid-structure interactions," Aeronaut. J. **115**, 593–604 (2011).
[23]J. Tang, S. Chimakurthi, R. Palacios, C. Cesnik, and W. Shyy, "Computational fluid-structure interaction of a deformable flapping wing for micro air vehicle applications," in *46th AIAA Aerospace Sciences Meeting and Exhibit* (AIAA, 2008), p. 615.
[24]T. Yamada and S. Yoshimura, "Line search partitioned approach for fluid-structure interaction analysis of flapping wing," Comput. Model. Eng. Sci. **24**, 51 (2008).
[25]D. Willis, E. Israeli, P.-O. Persson, M. Drela, J. Peraire, S. Swartz, and K. Breuer, "A computational framework for fluid structure interaction in biologically inspired flapping flight," in *25th AIAA Applied Aerodynamics Conference* (AIAA, 2007), p. 3803.
[26]B. A. Roccia, S. Preidikman, and B. Balachandran, "Computational dynamics of flapping wings in hover flight: A co-simulation strategy," AIAA J. **55**, 1806–1822 (2017).

[27]J. A. John D., *Computational Fluid Dynamics: The Basics with Applications* (McGraw-Hill Education, 1995).
[28]H. Liu, C. P. Ellington, K. Kawachi, C. van den Berg, and A. P. Willmott, "A computational fluid dynamic study of hawkmoth hovering," J. Exp. Biol. **201**, 461–477 (1998).
[29]S. A. Combes and T. L. Daniel, "Flexural stiffness in insect wings I. Scaling and the influence of wing venation," J. Exp. Biol. **206**, 2979–2987 (2003).
[30]M. Smith, P. Wilkin, and M. Williams, "The advantages of an unsteady panel method in modelling the aerodynamic forces on rigid flapping wings," J. Exp. Biol. **199**(5), 1073–1083 (1996).
[31]M. S. Vest and J. Katz, "Unsteady aerodynamic model of flapping wings," AIAA J. **34**, 1435–1440 (1996).
[32]L. N. Long and T. E. Fritz, "Object-oriented unsteady vortex lattice method for flapping flight," J. Aircr. **41**, 1275–1290 (2004).
[33]M. F. Valdez, B. Balachandran, and S. Preidikman, "Comparative study on analytical and computational aerodynamic models for flapping wings MAVs," Aeronaut. J. **124**, 1636–1665 (2020).
[34]B. A. Roccia, S. Preidikman, J. C. Massa, and D. T. Mook, "Modified unsteady vortex-lattice method to study flapping wings in hover flight," AIAA J. **51**, 2628–2642 (2013).
[35]R. K. Schwab, H. E. Reid, and M. Jankauski, "Reduced-order modeling and experimental studies of bilaterally coupled fluid–structure interaction in single-degree-of-freedom flapping wings," J. Vib. Acoust. **142**, 021012 (2020).
[36]Q. Wang, J. Goosen, and F. van Keulen, "An efficient fluid–structure interaction model for optimizing twistable flapping wings," J. Fluids Struct. **73**, 82–99 (2017).
[37]S. Combes and T. Daniel, "Flexural stiffness in insect wings II. Spatial distribution and dynamic wing bending," J. Exp. Biol. **206**, 2989–2997 (2003).
[38]S. M. Walker and G. K. Taylor, "A semi-empirical model of the aerodynamics of manoeuvring insect flight," J. R. Soc. Interface **18**, 20210103 (2021).
[39]C. Fernandez-Escudero, M. Gagnon, E. Laurendeau, S. Prothin, G. Michon, and A. Ross, "Comparison of low, medium and high fidelity numerical methods for unsteady aerodynamics and nonlinear aeroelasticity," J. Fluids Struct. **91**, 102744 (2019).
[40]H. Reid, H. Zhou, M. Maxcer, R. K. Peterson, J. Deng, and M. Jankauski, "Toward the design of dynamically similar artificial insect wings," Int. J. Micro Air Veh. **13**, 1 (2021).
[41]A. G. Norris, A. N. Palazotto, and R. G. Cobb, "Experimental structural dynamic characterization of the hawkmoth (*Manduca sexta*) forewing," Int. J. Micro Air Veh. **5**, 39–54 (2013).
[42]M. Jankauski, T. L. Daniel, and I. Shen, "Asymmetries in wing inertial and aerodynamic torques contribute to steering in flying insects," Bioinspiration Biomimetics **12**, 046001 (2017).
[43]M. Jankauski and I. Shen, "Dynamic modeling of an insect wing subject to three-dimensional rotation," Int. J. Micro Air Veh. **6**, 231–251 (2014).
[44]R. Schwab, E. Johnson, and M. Jankauski, "A novel fluid–structure interaction framework for flapping, flexible wings," J. Vib. Acoust. **141**, 061002 (2019).
[45]G. J. Berman and Z. J. Wang, "Energy-minimizing kinematics in hovering insect flight," J. Fluid Mech. **582**, 153–168 (2007).
[46]S. P. Sane and M. H. Dickinson, "The aerodynamic effects of wing rotation and a revised quasi-steady model of flapping flight," J. Exp. Biol. **205**, 1087–1096 (2002).
[47]J. Katz and A. Plotkin, *Low-Speed Aerodynamics* (Cambridge university Press, 2001), Vol. 13.
[48]W. Geissler and B. G. van der Wall, "Dynamic stall control on flapping wing airfoils," Aerosp. Sci. Technol. **62**, 1–10 (2017).
[49]M. Jones and N. Yamaleev, "The effect of a gust on the flapping wing performance," in 50th AIAA Aerospace Sciences Meeting Including the New Horizons Forum and Aerospace Exposition, 2012.
[50]H. Hadzic, "Development and application of finite volume method for the computation of flows around moving bodies on unstructured, overlapping grids," Ph.D. thesis (Technische Universität Hamburg, Hamburg, 2006).
[51]A. T. Bode-Oke and H. Dong, "The reverse flight of a monarch butterfly (*Danaus plexippus*) is characterized by a weight-supporting upstroke and postural changes," J. R. Soc. Interface **17**, 20200268 (2020).
[52]J. Reade and M. Jankauski, "Investigation of chordwise functionally graded flexural rigidity in flapping wings using a two-dimensional pitch-plunge model," Bioinspiration Biomimetics **17**, 066007 (2022).
[53]R. Schwab, E. Johnson, and M. Jankauski, "Reduced-order modeling and the physics governing flapping wing fluid-structure interaction," bioRxiv (2021).
[54]W. Shyy, H. Aono, S. Chimakurthi, P. Trizila, C.-K. Kang, C. Cesnik, and H. Liu, "Recent progress in flapping wing aerodynamics and aeroelasticity," Prog. Aerosp. Sci. **46**, 284–327 (2010).
[55]J. D. Anderson, *Fundamentals of Aerodynamics*, 5th ed. (McGraw-Hill, 2011).

THE EFFECT OF GRADED WING STIFFNESS ON AEROELASTIC EFFICIENCY IN FLAPPING WING FLIGHT

Flexibility is an important aspect in flapping wing flight as it can increase lift to drag ratios and reduce the energetic requirement of driving flapping kinematics. Shyy investigated the effects of bulk stiffness on lift production and found that reducing overall stiffness can result in an improved ratios of produced lift to required power[Shyy et al., 2010]. While some computational studies have shown that there is a relationship between wing flexibility and lift produced by the leading edge vortex, few studies have investigated the effects of wing flexibility outside of homogeneous changes to overall stiffness. This is an area of particular need for research as many insects have heterogeneous distribution of wing stiffness and wing thickness[Combes and Daniel, 2003a; Reid et al., 2021a].

Many studies of the influence of wing flexibility involve changes to the uniform flexural rigidity across the wing surface. While these studies show some of the effects of changes in wing flexibility, there is room for further investigation into a heterogeneous distribution of wing stiffness. Combes and Daniel [Combes and Daniel, 2003a] combined physical experimentation of the response to a point load on a hawkmoth wing and computational finite element analysis modeling of the wing to discover that hawkmoth's wing membranes have an exponential decay in flexural rigidity from wing root to wing tip and from leading edge to trailing edge. Such findings entice further questions of the relationship between graded wing stiffness and aeroelastic efficiency of insect size flapping wings.

Many studies and FWMAV prototypes have used wing spars to mimic the strengthening behavior of wing veins that allow insects to maintain additional rigidity and preferred deformation profiles. While these spars often attain desired effects for individual wings, their complicated assembly adds time and repeatability problems to the manufacturing process [Gerdes et al., 2013]. Instead, the use of a single material with modern manufacturing

practices like 3D printing or microfabrication could achieve similar benefits through the use of thickness tapering to affect the localized wing stiffness distribution.

In this study the influence of distributed stiffness through linearly graded thickness on flapping wing performance is presented for a range of chordwise, spanwise, and bilinear tapering cases. To evaluate this performance, bulk aerodynamic forces such as peak lifting force and mean lifting force and power requirements were modeled for flapping wings with varying thickness parameters. These flapping wings were modeled using the bilaterally coupled CFD and FEA software approach presented in chapter 2. An investigation into the energetic requirements of these flapping wing cases and whether changes were influenced primarily by aerodynamic or inertial loads was performed.

Methods

To keep the study general, the modeled wing was rectangular, with aspect ratio, surface area, and flapping kinematics constant across all structural layout cases. The wing's span length, chord length, and material density were chosen to match those of a Hawkmoth (*Manduca Sexta*) which is often used as a model organism in flapping wing studies for its large wingspan. The elastic modulus and Raleigh damping factors were then tailored such that the first natural frequency of the modeled homogeneous wing case matched that of the hawkmoth's. These properties were then held constant across all tapered wing cases.

Localized stiffness of the wing was varied by adjusting the local thickness of the wing which has a roughly cubic relationship to stiffness ($k \propto t^3$) due to thickness's effect on the cross-sectional area moment of inertia of a plate. These thickness variations followed functional gradation of

$$t(x,y) = t_o \left(1 - \lambda_C \frac{x}{L_C}\right)\left(1 - \lambda_S \frac{y}{L_S}\right)$$

Here, $t(x, y)$ refers to localized thickness at spatial locations x and y along the wing. λ_C and λ_S refer to scaling parameters in chordwise and spanwise directions respectively that range from 0 to 1, where $\lambda_{[\cdot]} = 0$ refers to no tapering, and $\lambda_{[\cdot]} = 1$ would result in tapering down to zero thickness. L_C and L_S refer to the chord length and span length respectively, and $t_\circ$ is the thickness at the leading edge (for chordwise thickness variation), or at the wing root (for spanwise thickness variation), where thickness is respectively highest. For the homogeneous wing ($\lambda_C = \lambda_S = 0$), t_o was chosen at $45\mu m$ to match the average thickness of a Hawkmoth wing [Reid et al., 2019]

The wing's total mass was then held constant to ensure that results were reflective of stiffness distribution instead of a comparison that was primarily influenced by differences in wing mass. To achieve this, $t_\circ$, varied in order to maintain

$$m = \rho t_o \iint_{x,y} \left(1 - \lambda_C \frac{x}{L_C}\right)\left(1 - \lambda_S \frac{y}{L_S}\right)$$

where ρ is the wing's material density, and m is the total mass of the wing which was determined from the homogeneous wing ($\lambda_C = \lambda_S = 0$) and then held constant for all tapered wings. 3 spanwise and chordwise tapering cases were modeled in addition to 7 bilinear tapering cases which can be found in Table 7.1.

The wing underwent modeled rotations about it's root and and leading edge. This relates to roll (θ) and pitch (ϕ) respectively. Considering an inertia X$-$Y$-$Z reference frame oriented at the rotation point of the wing (see Figure 7.1a), roll is rotation about the X axis which is orient chordwise from leading edge to trailing edge. This rotation produces a roll-fixed reference frame $x'-y'-z'$, from which pitch applies a rotation about the spanwise oriented y' axis. After these roll and pitch rotations, a wing-fixed coordinate system $x-y-z$ (see Figure 7.1b), can be used as a reference for wing deformations and aerodynamic phenomena relative to the wing's rigid body motion. In this wing-fixed coordinate system,

Table 7.1: Tapering Ratios

Chordwise Tapering	Spanwise Tapering	Bilinear Tapering	
λ_C	λ_S	λ_C	λ_S
0	0	0.25	0.25
0.5	0.5	0.25	0.75
0.9	0.9	0.5	0.5
		0.5	0.9
		0.75	0.25
		0.75	0.75
		0.9	0.9

the angular velocity Ω is defined as

$$\Omega = \left(\dot{\theta}\cos\phi\right)\boldsymbol{e_x} + \left(\dot{\phi}\right)\boldsymbol{e_y} + \left(\dot{\theta}\sin\phi\right)\boldsymbol{e_z}$$

where e_x, e_y and e_z are unit vectors in the $x-y-z$ wing-fixed coordinate system.

Specific kinematic parameters were chosen to match those of the Hawkmoth which flaps at $25Hz$ with harmonic rotations of $60°$ of roll and $45°$ of pitch, shifted out of phase by $\frac{\pi}{2}$. Yaw, which would be a rotation about the wing-fixed z axis, was neglected in this study. The coupled CFD and FEA models were arranged as described in chapter 2, with functionally distributed thickness of the shell elements in FEA. Parameters chosen for this model are shown in Table 7.2.

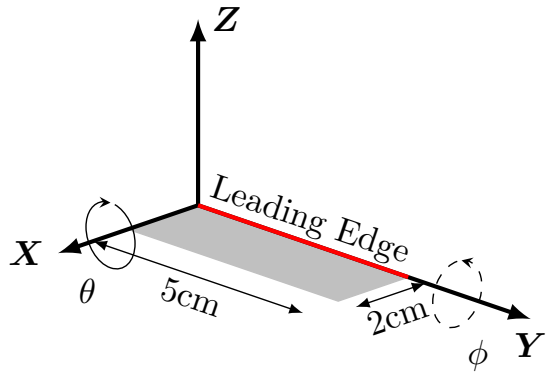

(a) Inertial reference frame with wing on X−Y plane

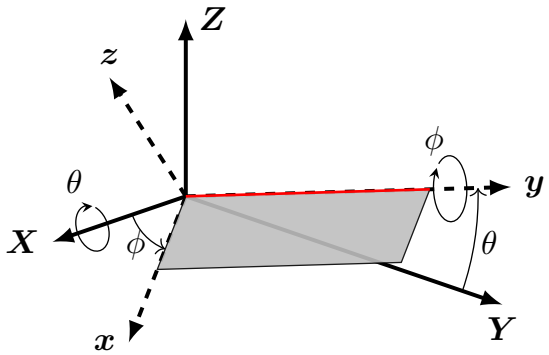

(b) Wing-fixed reference frame with wing on $x - y$ plane

Figure 7.1: Inertial (a) and wing-fixed (b) coordinate systems for the modeled rectangular wing with leading edge shown in red for reference. Kinematics include roll (θ) about the inertial X axis, and pitch (ϕ) about the rolled y axis.

Table 7.2: Modeling Parameters

Variable	Description	Value	Unit
	Wing & Kinematics		
L_S	Wing Spanlength	5	cm
L_C	Wing Chordlength	2	cm
θ_0	Roll Amplitude	60	∘
ϕ_0	Pitch Amplitude	45	∘
-	Pitch Phase	90	∘
f	Flap Frequency	25	Hz
	Computational Fluid Dynamics		
μ	Dynamic Viscosity of Air	1.86×10^{-5}	$Pa \cdot s$
ρ_f	Density of Air	1.18	$kg \cdot m^{-3}$
–	Domain Dimensions	0.19 x 0.21 x 0.2	m
–	Overset Dimensions	0.04 x 0.08 x 0.06	m
–	Mean Element Length (Domain)	1.2	mm
–	Mean Element Length (Overset)	0.6	mm
–	Total Number of Elements	3,319,937	–
–	Prism Layers	5	–
–	Prism Layer Growth Rate	1.5	–
Δt	Timestep	0.0003	s
–	Number of Iterations per Timestep	35	–
	Finite Element Analysis		
ρ	Wing Material Density	1200	$kg \cdot m^{-3}$
m	Total Wing Mass	5.4×10^{-5}	kg
E	Elastic Modulus	1.5×10^{12}	Pa
α	Raleigh Damping Factor	147.79	–
β	Raleigh Damping Factor	3.438×10^{-5}	–
–	Element Type	S4R	–
–	Number of Nodes	1071	–
–	Number of Shell Element Integration Points	5	–
Δt_{min}	Minimum Automatic Timestep	1×10^{-8}	s
Δt_{max}	Maximum Automatic Timestep	0.0003	s

Results

In all tapering cases considered, thrust, required power, and efficiency were compared. Here, thrust was considered as the sum of forces calculated via CFD acting in the inertial X direction on the wing. Power was calculated as $P = M \cdot \omega$, where ω is the wing's angular velocity and M was the reaction moment about the wing's origin gathered in FEA, including both inertial and aerodynamic load contributions. The energy requirement per wingbeat then is the time integral of P over one flapping cycle. The aerodynamic reaction moment was also used to calculate the contribution of power purely from aerodynamic forces and was calculated through $M_{aero} = \oiint_{x,y} F \times r$ where F is the incremental force acting on the wing in the wing-fixed x, y, or z direction and r is the position vector from the wing's origin to F. Efficiency then was calculated based on these thrusts and power requirements by considering the power required per flapping cycle, and dividing this quantity from the mean thrust produced.

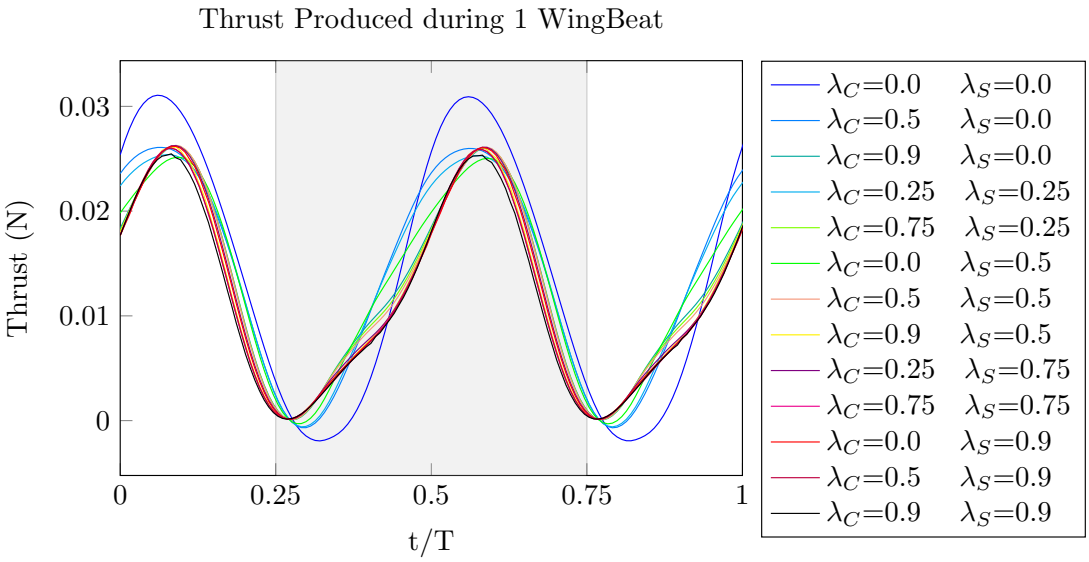

Figure 7.2: The thrust (force in inertial X directions) produced by the wing over 1 wingbeat across all modeled tapering ratios. Timing of stroke reversal is indicated by transitions between the gray and white background colors.

Comparing the thrust force gathered from CFD as shown in figure 7.2, it is clear that there is a correlation between tapering of the wing and peak thrust, but this effect quickly plateaus, and steeper tapering ratios are less impactful on peak thrust production. By comparing the mean thrust with respect to time, we can get a sense for how much weight each wing could support given its flapping kinematics and tapering ratio. In Figure 7.3, we find that the mean thrust is certainly lower for the highly tapered wing cases, constituting a 17.8% difference between the untapered wing, producing 14.1 mN of mean thrust, and the heavily tapered wing with λ_C=λ_S=0.9, producing 11.6 mN of mean thrust.

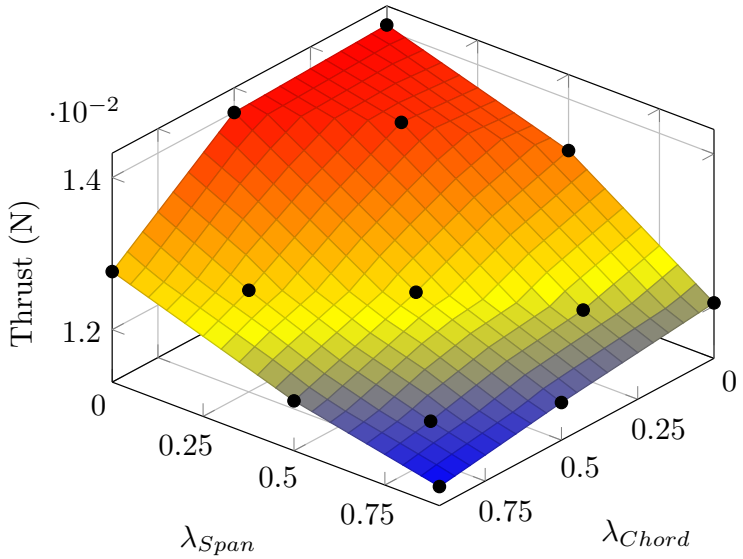

Figure 7.3: The mean thrust (force in inertial X direction) produced by the wing.The calculated efficiencies are plotted as black dots overlaid on an interpolated surface plot.

All tapered wing cases with spanwise tapering ratios greater than 0.5 dip into negative power requirements (Figure 7.4). This negative power (and therefore negative energy) requirement implies that some amount of potential energy is being stored in the system. This negative power in the time integral to calculate energy can be dealt with in one of three ways:

1. Negative power is treated negative, effectively recycling the stored potential energy to

reduce the energetic requirements of driving the wing.

2. Negative power requirements are treated as positive (this implies that the motor controller in a FWMAV actively braking to compensate for the stored energy).

3. Negative power is ignored, and only positive power contributes to the energetic requirements to drive the flapping kinematics while periods of time with negative power requirement are treated as simply requiring zero power to drive kinematics.

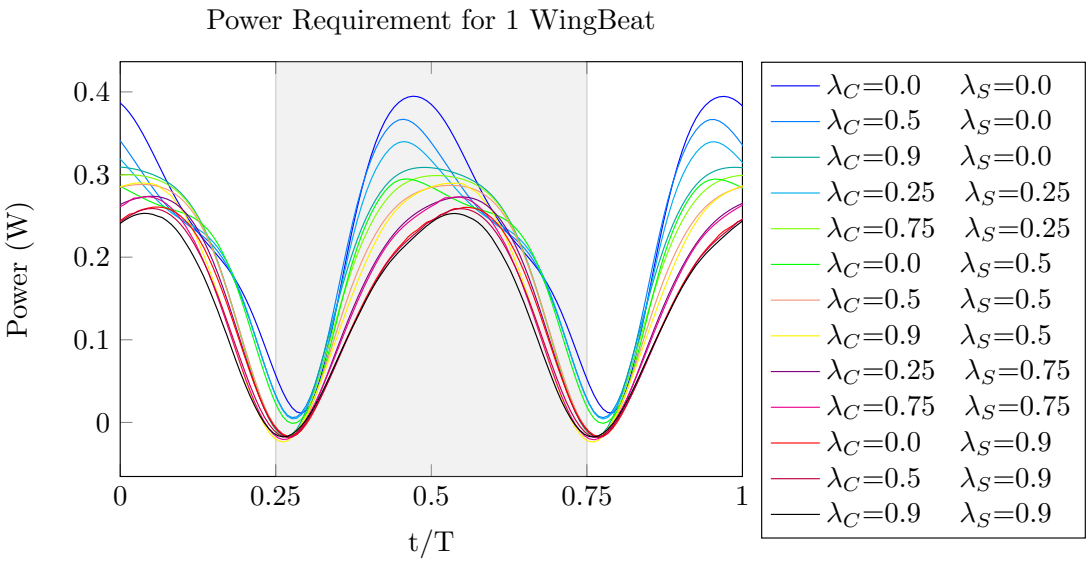

Figure 7.4: The required power to flap the wing over 1 wingbeat across all modeled tapering ratios. Timing of stroke reversal is indicated by transitions between the gray and white background colors.

With these options for dealing with negative power in mind, the time integral of power was taken, and divided by the average thrust from each wing case to produce a normalized interpretation of how energetically efficiently each wing produced thrust (Figure 7.5). It is clear that the trend toward increased energetic efficiency is at higher taper ratios is maintained regardless of how this negative power is handled with a maximum difference of 2.1% between the heavily tapered recycled energy vs braked energy cases. To consider

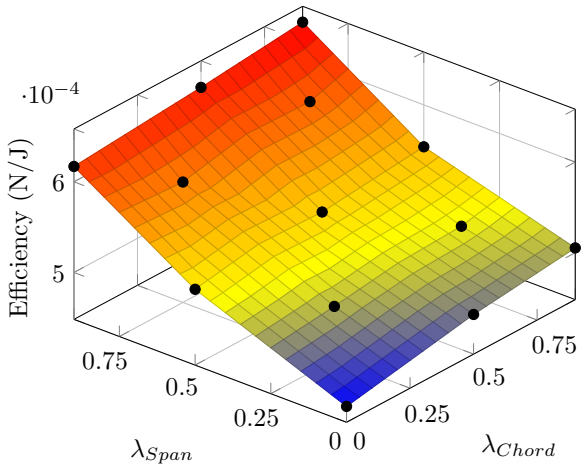

(a) Negative power recycled

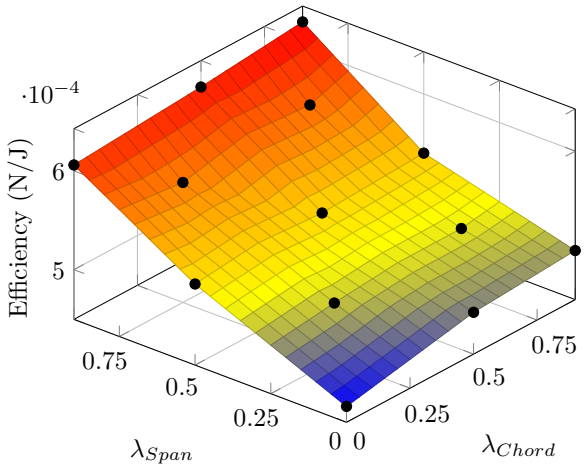

(b) Braking applied to negative power

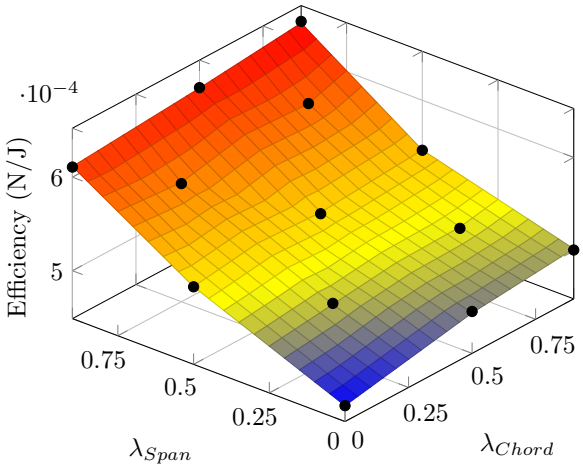

(c) Negative power ignored

Figure 7.5: Efficiency as a measure of the average thrust produced by the wing divided by the energetic requirement per flapping cycle. The calculated efficiencies are plotted as black dots overlaid on an interpolated surface plot. Negative power was handled by either (a) recycled energy back into the system, (b) actively braking to create a larger energetic requirement, or (c) ignoring negative power.

the benefits of wing tapering in a FWMAV conservatively, the braking energy case (Figure 7.5b) was used to compare flight performance with the highest energy cost. Heavily tapering the wing's thickness at $\lambda_C = \lambda_S = 0.9$ results in 1.35 times the lift force produced per joule of energetic requirement.

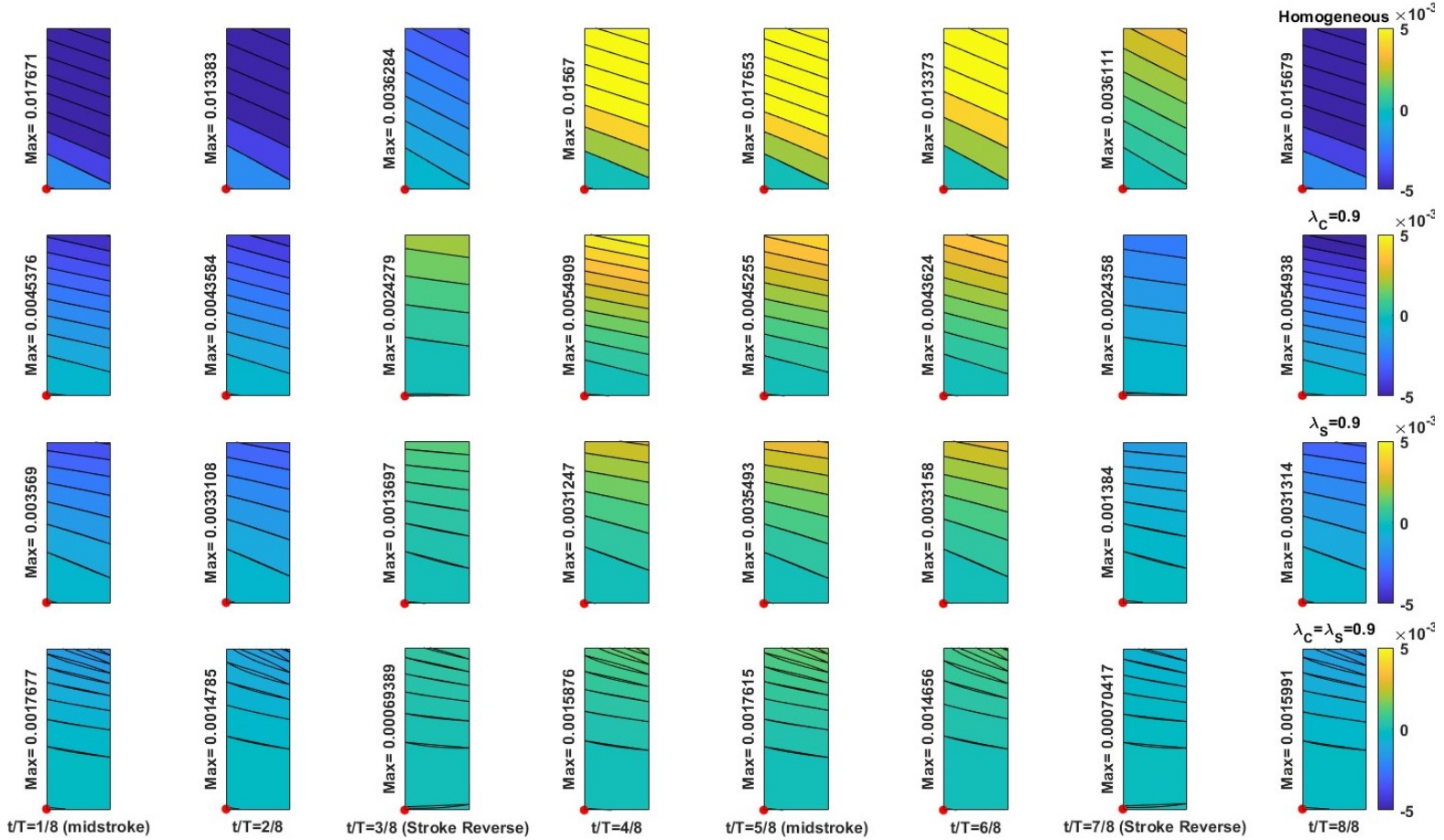

Figure 7.6: Distribution of wing deflection (in meters) for 8 points in time across one flapping cycle. The untapered or homogeneous (top), $\lambda_C = 0.9$ (second from top), $\lambda_S = 0.9$ (second from bottom), and $\lambda_C = \lambda_S = 0.9$ (bottom) tapering cases are shown along with the maximum deflection amplitude for each time step along the left side of the wing. The wing rotation point is shown as a red dot in the lower left corner of each wing.

Deflections of the wings from a wing-fixed reference frame show an interesting trend with regard to amplitude and distribution of deformation (see Figure 7.6). First, the amplitude of maximum deflection varies significantly from more than 17.5 mm in the homogeneous wing case, to just over 1.75 mm in the bilinearly tapered $\lambda_C = \lambda_S = 0.9$ case. This order of magnitude difference in deflection from the extreme tapering cases is also correlated to a significant change in natural frequencies. The first natural frequencies, which were associated with a primarily spanwise bending mode-shape, were $\omega_n = 60.8Hz$ for the homogeneous wing and $\omega_n = 288.7Hz$ for the bilinearly tapered $\lambda_C = \lambda_S = 0.9$ wing. The deformations of the homogeneous wing are significantly larger because the flapping frequency is so much closer to the wing's natural frequency than to that of the heavily tapered wing. Additionally, any superharmonic amplification excited by the homogeneous wing was likely not harnessed by the heavily tapered wing to increase deformation.

Consideration of the deflection's distribution is also important when comparing these tapering cases. Contour deflection lines for the homogeneous wing have a fairly even distribution along the spanwise direction, which shows that a majority of wing bending is located near the wing root, and the wing is otherwise undeformed. The contour lines of the heavily tapered wing however, have continually decreased spacing with distance from the wing root, indicating that deformation continues across more of the wing's surface. Additionally, the consistent angle of the contour lines shows that there is a significant amount of chordwise bending in the homogeneous wing, effectively changing the wing's angle of attack and chamber. The changing angle of the contour lines for the heavily tapered wing shows that spanwise bending and twisting are primarily localized near the wingtip, and have less influence on a majority of the wing surface. This difference in chordwise deformation could be expected from the proximity of flapping frequency to the wings' second natural frequencies associated with the chordwise bending mode shape of $\omega_n = 243Hz$ for the homogeneous wing, and $\omega_n = 842.5Hz$ for the tapered wing.

Discussion

The trends toward increased energetic efficiency with wing tapering in Figure 7.5 show a clear argument supporting the use of thickness tapering in the manufacturing process of FWMAV wings. While this tapering also slightly reduces the mean thrust produced by the wing (Figure 7.3), there is a greater reduction in power, so it can be assumed that with appropriate flapping frequency and wing size, the same thrust could be produced at a lower energetic costs. This increase in efficiency can be largely credited to a significant decrease in this wing's moment of inertia with tapering as the mass becomes concentrated near the rotation point.

Power, as mentioned in the methods section, is $P = M \cdot \omega$, and the total moment could be defined generally with contributions from both the inertial and the aerodynamic forces $M = \alpha \cdot I_\circ + r \times F_{aero}$. The aerodynamic load could be considered in a simplified manner from conventional aerodynamics theory, $F_{aero} = \frac{1}{2}\rho_f v^2 A C_{[\cdot]}$, with $C_{[\cdot]}$ being the aerodynamic lift or drag coefficient. The power required to drive the wing then scales cubicly with velocity, and is directly influenced by the moment of inertia primarily at stroke reversal where angular velocity is high. The aerodynamic force production, however, scales primarily with velocity squared. The large deformations of the homogeneous wing add to the effective roll and pitch amplitudes of the flapping kinematics, and therefore cause higher wing velocities contributing to the slight increase in produced thrust and a larger increase in required power. Additionally, this homogeneous wing has more mass distributed near the wing tip than any tapered case, and therefore has the largest moment of inertia contributing further to the increased power requirement.

A greater influence on aerodynamic force production was expected from tapering the structural thickness of the wing, however this was not the case. A closer examination of the distribution of wing deformation (Figure 7.6) reveals that as wing tapering is increased,

the wing becomes more rigid due to the reduction in bending moment. The distribution of the homogeneous wing's deflection however, reveals a largely linear distribution from wing root to wing tip, indicating that a majority of wing bending is located near the wing root. This implies that effectively the homogeneous wing undergoes an increased roll and pitch amplitude due to the deformations, where the bending near the wing root acts much like a torsional spring in the otherwise fairly rigid system.

While this study shows a clear energetic efficiency benefit toward tapering wings of constant mass, the reduction in energetic expense did come at the cost of a slight reduction in mean thrust. Application of these findings in the production of FWMAV wings would then be dependent upon manufacturing processes and actuator abilities of the MAV design. If wing area can be increased, or if the actuator design allows for higher flapping frequencies but with limited power output, a heavily tapered wing could be beneficial as the energetic costs to produce a proportional amount of thrust would be lower. If the wing's surface area or flapping frequency are limited however, it may be advantageous to keep the wing's thickness uniform, favoring thrust production over energetic efficiency to carry a payload.

The idea of manufacturing wings with one material drove the decision to maintain a constant elastic modulus and material density, however this ultimately resulted in comparing large wing deflections and an effective increase of rotation amplitudes in the homogeneous wing case to a much more rigid wing in the tapered wing cases. It is already established that wing flexibility can reduce the energetic costs associated with flight [Reid et al., 2019]. Additional work on the effect of wing stiffness could be performed by using this study's approach with similarly scaled maximum deflections by significantly lowering the elastic modulus of the tapered wing cases. This would likely result in a different deformation profile of the wings, which could hold a significant impact over the aerodynamic force production while maintaining a reduction in moment of inertia for tapered wings.

CONCLUSION

Flapping wings harness interesting fluid dynamics phenomena to achieve efficient flight at very low Reynolds numbers. This allows flying insects to achieve flight with incredibly small wing sizes, and could allow for the same in flapping wing micro air vehicles. Flapping wing micro air vehicles (FWMAVs) hold potential uses ranging from artificial pollinators to gas leak detectors in congested networks. Additionally, their efficiency at low Reynolds numbers prompts the use of flapping wings for more easily achievable flight in thin atmospheres like that of Mars. While the range of uses for flapping wings is quite broad, applying them remains difficult as a deeper understanding of how to improve flight efficiency is needed to increase payload capabilities in FWMAVs.

Through a combination of flapping stroke reversal and structural deformation, these wings are able to harness lift benefits from the leading edge vortex, without undergoing a dynamic stall. Some flapping kinematics involve a clap and fling phenomena between wing pairs that allows for additional lift production through wake capture. Even the Magnus effect aids in flapping winged flight when the pitch and roll rotations are appropriately timed out of phase. Flapping kinematics, wing geometry, and wing flexibility all impact these forms of force production, and with a such a large parameter space, finding optimal combinations of properties for flapping wings in FWMAVs is no simple undertaking.

While experimental studies of flapping wings are possible, they are often limited to in vivo insect experiments with set wing morphology and ungoverned kinematics, or require large motors whose inertia overpowers much of the measurable reaction forces from the wing. Additionally, experimental setups for force and moment measurements with robotic flappers are often limited in scope to study flapping at relatively low flapping frequencies. Testing of manufactured wings also requires course discretization of testable wings which are limited by current manufacturing process. While much can be gained from physical experimentation,

these limitations in practical experiments justify the use of validated computational tools to simulate flapping wing physics for a deeper understanding.

Conventional computational tools for the study of fluid dynamics and structural dynamics are well established and yield highly accurate results, however they come at a high computational cost. CFD analysis allows for a wide variety of studies in fluid flow and can be accurate when appropriately designed for the given problem, however the solution of the Navier Stokes partial differential equations often requires fine spatial and temporal discretization, resulting in lengthy solution times. Similarly, FEA can be applied to a wide variety of structural problems by choosing an appropriate element and analysis types, but often requires fine spatial discretization and temporal discretization that is dependent on strain rate. While these computation times often seem extreme, they are warranted by the accuracy they can achieve as models based in first principles.

The lift generating forces produced from subtle changes in the leading edge vortex, dynamic stalling behavior in the case of LEV bursting, and studies of complex and nonlinear structural dynamics all necessitate the use of these higher fidelity tools for flapping wing studies, however some studies into wing design or kinematics do not require such a robust simulation of the coupled fluid-structure interaction. In the case of studying bulk aerodynamic forces for a range of simple wing designs and kinematics, a deformable blade element method can model the aerodynamic behavior of a flapping wing in milliseconds as described in chapters 3, 4, 5, and 6. The computational efficiency of such a model allows for finely swept parameter studies across a large parameter space to investigate the effects of design parameters like flapping frequency, phase difference between rotational velocities, and wing stiffness.

While the increased computational efficiency of reduced order modeling techniques is advantageous in many cases, it comes at a cost of neglecting or simplifying aspects of the physics of the problem. In the case of the DBET model, the lift produced by the flapping

wing is expected to act very similarly to a conventional gliding wing, dependent primarily on the angle of attack and velocity of the wing. Also, the deformation of the wing is assumed to be a combination of a chosen number of mode shapes, resulting in a linear structural solver. While these simplifications were appropriate for the simple material properties, kinematics, and boundary conditions presented in chapters 3, 4, 5, and 6, studying the wing with more complex structural properties and less restrained boundary conditions as described in chapter 7, required the higher fidelity model which does not require many physics simplifications. It seems clear then that use of reduced-order modeling techniques has a more limited scope and will continue to require additional validation steps when compared to conventional high-fidelity modeling.

Reduced order modeling of flapping wing physics holds promise for quickly producing bulk aerelastic data, however they cannot fully replace higher fidelity solvers. High-fidelity solvers like coupled CFD and FEA often require untenable computation times to reach a quasi steady-state response (up to 45 hours in the case of the studies presented here). While the detail in fluid and structural physics being modeled certainly reduces the strengthens the credibility of the model compared to other techniques, the computation time limits the practicability of swept parameter or optimization studies. A tiered combination of modeling techniques, however, can hold tremendous power with the ability to narrow the parameter scope of a problem through quick reduced order modeling, then finding or confirming optimized cases in design through high-fidelity modeling. This combined approach to modeling would allow for a reduction in computation time in parameter sweep and optimization studies by several orders of magnitude, without losing the credibility in the end results gained from conventional high fidelity solvers.

High fidelity simulation data is also extremely informative for the development of reduced order models. Understanding of the complex fluid dynamics including the leading edge vortex, wingtip vortex, dynamic stall, and wake capture, allows for insights into

which driving forces are important to model in a reduced order framework, and which forces may have little impact and can be ignored in order to gain computational efficiency. Finding the natural frequencies associated with different structural mode shapes through FEA allows for an understanding of which mode shapes dominate deformation at varying flapping frequencies. Isolating either structural or fluid solvers also allows for validation and development of each part of the reduced order model, which is difficult to replicate experimentally. Additionally, the ability to intentionally neglect certain physics in a reduced order model and compare results against higher fidelity data which may hold more credibility also allows for an understanding of effect that many individual physics phenomena hold on the coupled problem.

Through this research, findings in the coupling between structural and fluid physics show the necessity to consider computational studies of flapping wings in a two-way coupled framework. Because this adds to the already untenable computational expense required for most CFD studies, further development of reduced order models could benefit flapping wing design and research significantly. It is also clear that many assumptions about flapping wing aerodynamics and structural physics can be made while maintaining reasonable levels of accuracy in some cases. The lack of chordwise discretization and fluid discretization in the DBET model presented in chapters 3 – 6, the exclusion of fluid modeling aside from shed wingtip vorticies in the UVLM based model presented in chapter 6, and the reduction of allowable deformations to only include combinations of the first two mode shapes in both models seem to be very significant assumptions, however much of the bulk aerodynamic and structural response data from these models aligned very well with the high fidelity solver.

By developing a strong modeling and simulation framework for wing design and kinematics, advancement in FWMAV design can be expedited by reducing iterations in the costly and often time-intensive prototyping phase of the design process. The study of wing tapering with a coupled high fidelity model presented here shows one avenue for increased

energetic efficiency through a relatively simple change to wing design. Further improvements to wing design for FWMAVs are possible and can reduce to the total power requirement from the actuator. This would allow for a higher payload capacity of the FWMAV that could be put toward additional sensors of power storage devices.

Employing a combination of modeling techniques, a deeper understanding of flapping wing aeroelastic physics is possible, with even more to be gained than any individual approach may allow. The ability to sweep through parameter spaces of wing structure properties with reduced order modeling techniques allowed for an insight into what trends could be expected, and modeling points of interest with the high fidelity model allowed for interpretations of the physics phenomena that were driving these correlations.

Computational simulation allows for studies of flapping wing designs outside of what may be possible or feasible with current manufacturing techniques as well. Chapter 7 presents a study on linear tapering the thickness of a rectangular wing, but similarly designed simulations could be employed to study more complicated structural designs such as tapered vein networks, distributed or localized damping elements within the wing, or a wide variety of bioinspired wing geometries. Through the coupled fluid and structural models, a deeper understanding of biological designs, such as the transport of hemolymph pressure throughout the wing veins during flapping flight, could be gained and used as bioinspiration for future FWMAV wing designs.

While the work presented in this dissertation focused primarily in studying the aeroelastic effects of changes to wing structure, changes to flapping kinematics and fluid properties could also be studied, and would gain similar advantage from a combined modeling approach. This allows for many complicated studies to become approachable including how air density affects flapping wing performance, how wing compliance passively impacts flight stability in gusty and turbulent wind, or how the ratio of inertial to aerodynamic forces may be impacted by a wing's design or flapping kinematics, to name a few. These studies may

drive FWMAVs to be employed in future Mars missions where such devices could be used in data collection, or this could inspire the use flapping wings as propulsion mechanisms for unmanned submersibles.

The use of computational modeling can allow for detailed visualization of the complex airflow and wing deformations involved in flapping flight. Many forces, moments, and energetic data that varies significantly in time and space can be gathered, which would be very difficult or impossible to measure experimentally. Additionally, flapping kinematics and wing designs can be modeled well outside the scope of current manufacturing and motor capabilities, allowing modeling techniques to inspire new manufacturing and design methods. These benefits of simulation as a means of study for flapping wings give it the potential to significantly improve our understanding of the underlying physics and trends. Ultimately, this work may allow for a deeper understanding of insect flight, further development of aerodynamic and aeroelastic modeling techniques, and the realization of a whole new class of aircraft.

REFERENCES CITED

Abdelkefi, A. (2016). Aeroelastic energy harvesting: A review. *International Journal of Engineering Science*, 100:112–135.

Addo-Akoto, R., Han, J.-S., and Han, J.-H. (2021). Roles of wing flexibility and kinematics in flapping wing aerodynamics. *Journal of Fluids and Structures*, 104:103317.

Aiello, B. R., Stanchak, K. E., Weber, A. I., Deora, T., Sponberg, S., and Brunton, B. W. (2021). Spatial distribution of campaniform sensilla mechanosensors on wings: form, function, and phylogeny. *Current Opinion in Insect Science*, 48:8–17. NeuroScience . Special Section on Insects as food and feed.

Anderson, J. D. (1995). *Computational Fluid Dynamics: The Basics with Applications*. McGraw-Hill Education.

Anderson, J. D. (2011). *Fundamentals of aerodynamics*. McGraw-Hill, 5th edition.

Arfaoui, B., Bouzaher, M. T., Guerira, B., and Bensaci, C. E. (2021). On the performance of swing arm flapping turbines. *Journal of Solar Energy Engineering, Transactions of the ASME*, 143.

Au, L. T. K., Phan, H. V., and Park, H. C. (2017). Comparison of aerodynamic forces and moments calculated by three-dimensional unsteady blade element theory and computational fluid dynamics. *Journal of Bionic Engineering*, 14:746–758.

Bayiz, Y. E. and Cheng, B. (2021). State-space aerodynamic model reveals high force control authority and predictability in flapping flight. *Journal of The Royal Society Interface*, 18(181):20210222.

Benini, G. R., Belo, E. M., and Marques, F. D. (2004). Numerical model for the simulation of fixed wings aeroelastic response. *Journal of the Brazilian Society of Mechanical Sciences and Engineering*, 26:129–136.

Berman, G. J. and Wang, Z. J. (2007). Energy-minimizing kinematics in hovering insect flight. *Journal of Fluid Mechanics*, 582:153–168.

Biancolini, M. E., Viola, I. M., and Riotte, M. (2014). Sails trim optimisation using cfd and rbf mesh morphing. *Computers and Fluids*, 93:46–60.

Bie, D., Li, D., Xiang, J., Li, H., Kan, Z., and Sun, Y. (2021). Design, aerodynamic analysis and test flight of a bat-inspired tailless flapping wing unmanned aerial vehicle. *Aerospace Science and Technology*, 112.

Bie, D., Zuo, S., Li, H., Shao, H., and Li, D. (2020). Aerodynamic analysis of a gull-inspired flapping wing glider. *IOP Conference Series: Materials Science and Engineering*, 887(1):012003.

Breuer, K. (2019). Flight of the robobee. *Nature*.

Brunton, S. L., Noack, B. R., and Koumoutsakos, P. (2020). Machine learning for fluid mechanics. *Annual Review of Fluid Mechanics*, 52(1):477–508.

Burgess, S. (2021). A review of linkage mechanisms in animal joints and related bioinspired designs. *Bioinspiration and Biomimetics*, 16.

Cai, X., Kolomenskiy, D., Nakata, T., and Liu, H. (2021). A cfd data-driven aerodynamic model for fast and precise prediction of flapping aerodynamics in various flight velocities. *Journal of Fluid Mechanics*, 915.

Campion, M., Ranganathan, P., and Faruque, S. (2019). Uav swarm communication and control architectures: A review. *Journal of Unmanned Vehicle Systems*, 7:93–106.

Chen, S., Wang, L., Guo, S., Zhao, C., and Tong, M. (2020). A bio-inspired flappingwing rotor of variant frequency driven by ultrasonic motor. *Applied Sciences (Switzerland)*, 10.

Christensen, B. and Owkes, M. (2023). Efficient extraction of atomization processes from high-fidelity simulations. *Computers & Fluids*, 254:105808.

Combes, S. and Daniel, T. (2003a). Flexural stiffness in insect wings ii. spatial distribution and dynamic wing bending. *Journal of Experimental Biology*, 206(17):2989–2997.

Combes, S. A. and Daniel, T. L. (2003b). Into thin air: Contributions of aerodynamic and inertial-elastic forces to wing bending in the hawkmoth manduca sexta. *Journal of Experimental Biology*, 206:2999–3006.

Das, R., Yadav, R. N., Sihota, P., Uniyal, P., Kumar, N., and Bhushan, B. (2018). Biomechanical evaluation of wasp and honeybee stingers. *Scientific Reports*, 8.

Dawson, S. T. M. and Brunton, S. L. (2021). Improved approximations to the wagner function using sparse identification of nonlinear dynamics.

Deora, T., Singh, A. K., and Sane, S. P. (2015). Biomechanical basis of wing and haltere coordination in flies. *Proceedings of the National Academy of Sciences of the United States of America*, 112:1481–1486.

Dickerson, B. H., Aldworth, Z. N., and Daniel, T. L. (2014). Control of moth flight posture is mediated by wing mechanosensory feedback. *Journal of Experimental Biology*, 217(13):2301–2308.

Dickerson, B. H., Fox, J. L., and Sponberg, S. (2021). Functional diversity from generic encoding in insect campaniform sensilla. *Current Opinion in Physiology*, 19:194–203.

Dickinson, M. H., Lehmann, F.-O., and Sane, S. P. (1999). Wing rotation and the aerodynamic basis of insect flight. *Science*, 284(5422):1954–1960.

Du, G. and Sun, M. (2010). Effects of wing deformation on aerodynamic forces in hovering hoverflies. *Journal of Experimental Biology*, 213(13):2273–2283.

Durbin, P. A. (2017). *Turbulence Closure Models for Computational Fluid Dynamics*, pages 1–22. John Wiley & Sons, Ltd.

Eberle, A., Dickerson, B., Reinhall, P., and Daniel, T. (2015). A new twist on gyroscopic sensing: body rotations lead to torsion in flapping, flexing insect wings. *Journal of the Royal Society Interface*, 12(104):20141088.

Engels, T., Kolomenskiy, D., and Lehmann, F. O. (2021). Flight efficiency is a key to diverse wing morphologies in small insects. *Journal of the Royal Society Interface*, 18.

Fairuz, Z. M., Abdullah, M. Z., Yusoff, H., and Abdullah, M. K. (2013). Fluid structure interaction of unsteady aerodynamics of flapping wing at low reynolds number. *Engineering Applications of Computational Fluid Mechanics*, 7:144–158.

Fan, X. and Breuer, K. (2021). *Reduced-order modeling of a bat flying with heavy and highly articulated flapping wing.*

Farisenkov, S. E., Kolomenskiy, D., Petrov, P. N., Engels, T., Lapina, N. A., Lehmann, F. O., Onishi, R., Liu, H., and Polilov, A. A. (2022). Novel flight style and light wings boost flight performance of tiny beetles. *Nature*, 602:96–100.

Faure, T. M., Roncin, K., Viaud, B., Simonet, T., and Daridon, L. (2022). Flapping wing propulsion: Comparison between discrete vortex method and other models. *Physics of Fluids*, 34.

Fernandez-Escudero, C., Gagnon, M., Laurendeau, E., Prothin, S., Michon, G., and Ross, A. (2019). Comparison of low, medium and high fidelity numerical methods for unsteady aerodynamics and nonlinear aeroelasticity. *Journal of Fluids and Structures*, 91:102744.

Fitzgerald, T., Valdez, M., Vanella, M., Balaras, E., and Balachandran, B. (2011). Flexible flapping systems: Computational investigations into fluid-structure interactions. *The Aeronautical Journal*, 115(1172):593–604.

Fuller, S. B., Karpelson, M., Censi, A., Ma, K. Y., and Wood, R. J. (2014). Controlling free flight of a robotic fly using an onboard vision sensor inspired by insect ocelli. *Journal of the Royal Society Interface*, 11.

Geissler, W. and van der Wall, B. G. (2017). Dynamic stall control on flapping wing airfoils. *Aerospace Science and Technology*, 62:1–10.

Gerdes, J., Cellon, K., Bruck, H., and Gupta, S. (2013). Characterization of the mechanics of compliant wing designs for flapping-wing miniature air vehicles. *Experimental Mechanics*, 53:1561–1571.

Ghanaatpishe, M., Bayiz, Y. E., Cheng, B., and Fathy, H. K. (2018). Rotary Versus Flapping Flight: An Application Study for Optimal Periodic Control Theory. *Dynamic Systems and Control Conference*, 1. V001T11A003.

Gnatzy, W., Grunert, U., and Bender, M. (1987). Campaniform sensilla of calliphora vicina (insecta, diptera). *Zoomorphology*, 106:312–319.

Hadzic, H. (2006). Development and application of finite volume method for the computation of flows around moving bodies on unstructured, overlapping grids. *Ph.D. thesis, Technische Universität Hamburg, Hamburg*.

Hamamoto, M., Ohta, Y., Hara, K., and Hisada, T. (2007). Application of fluid–structure interaction analysis to flapping flight of insects with deformable wings. *Advanced Robotics*, 21(1-2):1–21.

Heathcote, S., Wang, Z., and Gursul, I. (2008). Effect of spanwise flexibility on flapping wing propulsion. *Journal of Fluids and Structures*, 24(2):183–199.

Hedrick, T. L. (2008). Software techniques for two- and three-dimensional kinematic measurements of biological and biomimetic systems. *Bioinspiration and Biomimetics*, 3.

Hedrick, T. L. and Daniel, T. L. (2006). Flight control in the hawkmoth Manduca sexta: the inverse problem of hovering. *Journal of Experimental Biology*, 209(16):3114–3130.

Hengstenberg, R. (1991). Gaze control in the blowfly calliphora: a multisensory, two-stage integration process. *Seminars in Neuroscience*, 3(1):19–29. Sensori-Motor Integration.

Hinson, B. T. and Morgansen, K. A. (2015). Gyroscopic sensing in the wings of the hawkmoth manduca sexta: the role of sensor location and directional sensitivity. *Bioinspiration & biomimetics*, 10(5):056013.

Hope, D. K., DeLuca, A. M., and O'Hara, R. P. (2018). Investigation into reynolds number effects on a biomimetic flapping wing. *International Journal of Micro Air Vehicles*, 10:106–122.

Hu, Z., McCauley, R., Schaeffer, S., and Deng, X. (2009). Aerodynamics of dragonfly flight and robotic design. In *2009 IEEE International Conference on Robotics and Automation*, pages 3061–3066.

Huston, S. J. and Jayaraman, V. (2011). Studying sensorimotor integration in insects. *Current Opinion in Neurobiology*, 21(4):527–534. Sensory and motor systems.

Huston, S. J. and Krapp, H. G. (2008). Visuomotor transformation in the fly gaze stabilization system. *PLOS Biology*, 6(7):1–11.

Ishihara, D., Horie, T., and Denda, M. (2009). A two-dimensional computational study on the fluid–structure interaction cause of wing pitch changes in dipteran flapping flight. *Journal of Experimental Biology*, 212(1):1–10.

Jankauski, M., Daniel, T. L., and Shen, I. Y. (2017). Asymmetries in wing inertial and aerodynamic torques contribute to steering in flying insects. *Bioinspiration and Biomimetics*, 12.

Jankauski, M., Schwab, R., Casey, C., and Mountcastle, A. (2021). Insect wing buckling influences stress and stability during collisions. *Proceedings of the ASME Design Engineering Technical Conference*, 10.

Jankauski, M. and Shen, I. (2014). Dynamic modeling of an insect wing subject to three-dimensional rotation. *International Journal of Micro Air Vehicles*, 6(4):231–251.

Jeong, J. and Hussain, F. (1995). On the identification of a vortex. *Journal of Fluid Mechanics*, 285:69–94.

Ji, B., Zhu, Z., Guo, S., Chen, S., Zhu, Q., Li, Y., Yang, F., Song, R., and Li, Y. (2020). Aerodynamic analysis of a flapping wing aircraft for short landing. *Applied Sciences*, 10(10).

Jones, M. and Yamaleev, N. (2012). The effect of a gust on the flapping wing performance.

Katz, J. and Plotkin, A. (2001). *Low-speed aerodynamics*, volume 13. Cambridge university press.

Ke, X., Zhang, W., Shi, J., and Chen, W. (2021). The modeling and numerical solution for flapping wing hovering wingbeat dynamics. *Aerospace Science and Technology*, 110.

Keennon, M., Klingebiel, K., and Won, H. (2012). Development of the nano hummingbird: A tailless flapping wing micro air vehicle. In *50th AIAA aerospace sciences meeting including the new horizons forum and aerospace exposition*, page 588.

Kesel, A. B., Philippi, U., and Nachtigall, W. (1998). Biomechanical aspects of the insect wing: an analysis using the finite element method. *Computers in Biology and Medicine*, 28(4):423–437.

Khosravi, M. and Novinzadeh, A. B. (2021). A multi-body control approach for flapping wing micro aerial vehicles. *Aerospace Science and Technology*, 112.

Kodali, D. and Kang, C. K. (2017). An analytical model and scaling of chordwise flexible flapping wings in forward flight. *Bioinspiration and Biomimetics*, 12.

Lankford, J. L. and Chopra, I. (2022). Coupled aeroelastic study of a flexible micro air vehicle-scale flapping wing in hovering flight. *Journal of Aircraft*, 59:154–172.

Lee, N., Lee, S., Cho, H., and Shin, S. (2018). Effect of flexibility on flapping wing characteristics in hover and forward flight. *Computers & Fluids*, 173:111–117.

Lehmann, F.-O. (2008). When wings touch wakes: understanding locomotor force control by wake–wing interference in insect wings. *Journal of Experimental Biology*, 211(2):224–233.

Lighthill, M. J. (1973). On the weis-fogh mechanism of lift generation. *Journal of Fluid Mechanics*, 60(1):1–17.

Liu, H., Ellington, C. P., Kawachi, K., van den Berg, C., and Willmott, A. P. (1998). A computational fluid dynamic study of hawkmoth hovering. *Journal of Experimental Biology*, 201(4):461–477.

Logan, D. L. (2007). *A first course in the finite element method*. Thomson.

Long, L. N. and Fritz, T. E. (2004). Object-oriented unsteady vortex lattice method for flapping flight. *Journal of Aircraft*, 41(6):1275–1290.

Lynch, J., Gau, J., Sponberg, S., and Gravish, N. (2021). Dimensional analysis of spring-wing systems reveals performance metrics for resonant flapping-wing flight. *Journal of the Royal Society Interface*, 18(175):20200888.

Mai, H., Dietz, G., Geißler, W., Richter, K., Bosbach, J., Richard, H., and de Groot, K. (2008). Dynamic stall control by leading edge vortex generators. *Journal of the American Helicopter Society*, 53(1):26–36.

Mao, S. and Gang, N. D. (2003). Lift and power requirements of hovering insect flight. *The Chinese Society of Theoretical and Applied Mechanics Chinese Journal of Mechanics Press*, 19.

McLean, D. (2012). *Understanding Aerodynamics: Arguing from the Real Physics*. Aerospace Series. Wiley.

Miller, L. A. and Peskin, C. S. (2009). Flexible clap and fling in tiny insect flight. *Journal of Experimental Biology*, 212(19):3076–3090.

Moore, M. (2014). Analytical results on the role of flexibility in flapping propulsion. *Journal of fluid mechanics*, 757:599–612.

Nakata, T. and Liu, H. (2012a). Aerodynamic performance of a hovering hawkmoth with flexible wings: a computational approach. *Proceedings of the Royal Society B: Biological Sciences*, 279(1729):722–731.

Nakata, T. and Liu, H. (2012b). A fluid–structure interaction model of insect flight with flexible wings. *Journal of Computational Physics*, 231(4):1822–1847.

Nakata, T., Liu, H., and Bomphrey, R. J. (2015). A cfd-informed quasi-steady model of flapping-wing aerodynamics. *Journal of Fluid Mechanics*, 783:323–343.

Norberg, U. M. (1996). *Energetics of Flight*, pages 199–249. Springer US, Boston, MA.

Norris, A. G. (2013). *Experimental characterization of the structural dynamics and aero-structural sensitivity of a hawkmoth wing toward the development of design rules for flapping-wing micro air vehicles*. Air Force Institute of Technology.

Norris, A. G., Palazotto, A. N., and Cobb, R. G. (2013). Experimental structural dynamic characterization of the hawkmoth (manduca sexta) forewing. *International Journal of Micro Air Vehicles*, 5(1):39–54.

Pass, G. (2018). Beyond aerodynamics: The critical roles of the circulatory and tracheal systems in maintaining insect wing functionality. *Arthropod Structure and Development*, 47:391–407.

Percin, M., Hu, Y., van Oudheusden, B. W., Remes, B., and Scarano, F. (2011). Wing flexibility effects in clap-and-fling. *International Journal of Micro Air Vehicles*, 3(4):217–227.

Pesavento, U. and Wang, Z. J. (2004). Falling paper: Navier-stokes solutions, model of fluid forces, and center of mass elevation. *Physical Review Letters*, 93.

Phan, H. V., Nguyen, Q. V., Truong, Q. T., Truong, T. V., Park, H. C., Goo, N. S., Byun, D., and Kim, M. J. (2012). Stable vertical takeoff of an insect-mimicking flapping-wing system without guide implementing inherent pitching stability. *Journal of Bionic Engineering*, 9:391–401.

Phillips, N. and Knowles, K. (2011). Effect of flapping kinematics on the mean lift of an insect-like flapping wing. *Proceedings of the Institution of Mechanical Engineers, Part G: Journal of Aerospace Engineering*, 225:723–736.

Phillips, N. and Knowles, K. (2013). Formation of vortices and spanwise flow on an insect-like flapping wing throughout a flapping half cycle. *Aeronautical Journal -New Series-*, 177:471–490.

Pohly, J. A., kwon Kang, C., Landrum, D. B., Bluman, J. E., and Aono, H. (2021). Data-driven cfd scaling of bioinspired mars flight vehicles for hover. *Acta Astronautica*, 180:545–559.

Pons, A. and Beatus, T. (2022). Distinct forms of resonant optimality within insect indirect flight motors. *Journal of The Royal Society Interface*, 19(190):20220080.

Porter, J. H. and Harvey, P. S. (2019). Imposing a node at a desired location along a beam under harmonic base excitation: Theory and experiment. *Journal of Vibration and Acoustics, Transactions of the ASME*, 141.

Pratt, B., Deora, T., Mohren, T., and Daniel, T. (2017). Neural evidence supports a dual sensory-motor role for insect wings. *Proceedings of the Royal Society B: Biological Sciences*, 284(1862):20170969.

Ramesh, K., Gopalarathnam, A., Granlund, K., Ol, M. V., and Edwards, J. R. (2014). Discrete-vortex method with novel shedding criterion for unsteady aerofoil flows with intermittent leading-edge vortex shedding. *Journal of Fluid Mechanics*, 751:500–538.

Reade, J. and Jankauski, M. (2022). Investigation of chordwise functionally graded flexural rigidity in flapping wings using a two-dimensional pitch-plunge model. *Bioinspiration & Biomimetics*.

Reade, J. and Jankauski, M. A. (2020). Deformable blade element and unsteady vortex lattice fluid-structure interaction modeling of a 2d flapping wing. In *International Design Engineering Technical Conferences and Computers and Information in Engineering Conference*, volume 83969, page V007T07A032. American Society of Mechanical Engineers.

Reid, H., Zhou, H., Maxcer, M., Peterson, R. K., Deng, J., and Jankauski, M. (2021a). Toward the design of dynamically similar artificial insect wings. *International Journal of Micro Air Vehicles*, 13.

Reid, H., Zhou, H., Maxcer, M., Peterson, R. K., Deng, J., and Jankauski, M. (2021b). Toward the design of dynamically similar artificial insect wings. *International Journal of Micro Air Vehicles*, 13:1756829321992138.

Reid, H. E., Schwab, R. K., Maxcer, M., Peterson, R. K., Johnson, E. L., and Jankauski, M. (2019). Wing flexibility reduces the energetic requirements of insect flight. *Bioinspiration and Biomimetics*, 14.

Roccia, B. A., Preidikman, S., and Balachandran, B. (2017). Computational dynamics of flapping wings in hover flight: a co-simulation strategy. *AIAA Journal*, 55(6):1806–1822.

Roccia, B. A., Preidikman, S., Massa, J. C., and Mook, D. T. (2013). Modified unsteady vortex-lattice method to study flapping wings in hover flight. *AIAA journal*, 51(11):2628–2642.

Sane, S. P. and Dickinson, M. H. (2002). The aerodynamic effects of wing rotation and a revised quasi-steady model of flapping flight. *Journal of experimental biology*, 205(8):1087–1096.

Sane, S. P., Dieudonné, A., Willis, M. A., and Daniel, T. L. (2007). Antennal mechanosensors mediate flight control in moths. *Science*, 315(5813):863–866.

Sato, H., Berry, C., Peeri, Y., Baghoomian, E., Casey, B., Lavella, G., VandenBrooks, J., Harrison, J., and Maharbiz, M. (2009). Remote radio control of insect flight. *Frontiers in Integrative Neuroscience*, 3.

Schwab, R., Johnson, E., and Jankauski, M. (2019). A novel fluid-structure interaction framework for flapping, flexible wings. *Journal of Vibration and Acoustics, Transactions of the ASME*, 141.

Schwab, R., Johnson, E., and Jankauski, M. (2021). Reduced-order modeling and the physics governing flapping wing fluid-structure interaction. *bioRxiv*.

Schwab, R., Reade, J., and Jankauski, M. (2022). Quasi three-dimensional deformable blade element and unsteady vortex lattice reduced-order modeling of fluid–structure interaction in flapping wings. *Physics of Fluids*, 34(12):121903.

Schwab, R., Reid, H., and Jankauski, M. (2020). Reduced-order modeling and experimental studies of bilaterally coupled fluid- structure interaction in single- degree-of-freedom flapping wings. *Journal of Vibration and Acoustics, Transactions of the ASME*, 142.

Shyy, W., Aono, H., Chimakurthi, S., Trizila, P., Kang, C.-K., Cesnik, C., and Liu, H. (2010). Recent progress in flapping wing aerodynamics and aeroelasticity. *Progress in Aerospace Sciences*, 46(7):284–327.

Sreetharan, P. and Wood, R. J. (2011). Passive torque regulation in an underactuated flapping wing robotic insect. *Autonomous robots*, 31:225–234.

Sørensen, J. N., Dag, K. O., and Ramos-García, N. (2014). A new tip correction based on the decambering approach. *Journal of Physics: Conference Series*, 524(1):012097.

Taha, H. E., Hajj, M. R., and Beran, P. S. (2014). State-space representation of the unsteady aerodynamics of flapping flight. *Aerospace Science and Technology*, 34:1–11.

Talarico, D. J., Mazzeo, A., and Denda, M. (2020). The 2d lumped wake vortex method applied to unsteady flapping. *International Journal of Intelligent Unmanned Systems*, 8:225–238.

Tang, J., Chimakurthi, S., Palacios, R., Cesnik, C., and Shyy, W. (2008). Computational fluid-structure interaction of a deformable flapping wing for micro air vehicle applications. In *46th AIAA Aerospace Sciences Meeting and Exhibit*, page 615.

Tian, F.-B., Dai, H., Luo, H., Doyle, J. F., and Rousseau, B. (2014). Fluid–structure interaction involving large deformations: 3d simulations and applications to biological systems. *Journal of computational physics*, 258:451–469.

Timoshenko, S. (1983). *History of strength of materials: with a brief account of the history of theory of elasticity and theory of structures*. Courier Corporation.

Trimmer, W. S. N. (1989). Microrobots and micromechanical systems. *Sensors and Actuators*, 19:267–287.

Truong, Q. T., Nguyen, Q. V., Truong, V. T., Park, H. C., Byun, D. Y., and Goo, N. S. (2011). A modified blade element theory for estimation of forces generated by a beetle-mimicking flapping wing system. *Bioinspiration and Biomimetics*, 6.

Usherwood, J. R., Cheney, J. A., Song, J., Windsor, S. P., Stevenson, J. P., Dierksheide, U., Nila, A., and Bomphrey, R. J. (2020). High aerodynamic lift from the tail reduces drag in gliding raptors. *Journal of Experimental Biology*, 223.

Valdez, M. F., Balachandran, B., and Preidikman, S. (2020). Comparative study on analytical and computational aerodynamic models for flapping wings mavs. *The Aeronautical Journal*, 124(1280):1636–1665.

VanEngelsdorp, D. and Meixner, M. D. (2010). A historical review of managed honey bee populations in europe and the united states and the factors that may affect them. *Journal of Invertebrate Pathology*, 103:S80–S95.

Vest, M. S. and Katz, J. (1996). Unsteady aerodynamic model of flapping wings. *AIAA journal*, 34(7):1435–1440.

Videler, J. J., Stamhuis, E. J., and Povel, G. D. E. (2004). Leading-edge vortex lifts swifts. *Science*, 306(5703):1960–1962.

Viswanath, K., Sharma, A., Gabbita, S., Geder, J., Ramamurti, R., and Pruessner, M. (2019). Evaluation of surrogate models for multi-fin flapping propulsion systems. In *OCEANS 2019 MTS/IEEE SEATTLE*, pages 1–9. IEEE.

Walker, S. M. and Taylor, G. K. (2021). A semi-empirical model of the aerodynamics of manoeuvring insect flight. *Journal of the Royal Society Interface*, 18(177):20210103.

Wang, L., Liu, X., and Kolios, A. (2016). State of the art in the aeroelasticity of wind turbine blades: Aeroelastic modelling. *Renewable and Sustainable Energy Reviews*, 64:195–210.

Wang, Q., Goosen, J., and van Keulen, F. (2017). An efficient fluid–structure interaction model for optimizing twistable flapping wings. *Journal of Fluids and Structures*, 73:82–99.

Weisfeld, M., Moses, K., Prigg, D., Bachmann, R., Willis, M., and Quinn, R. (2019). Manufacturing artificial wings based on the manduca sexta hawkmoth. In *Biomimetic and Biohybrid Systems: 8th International Conference, Living Machines 2019, Nara, Japan, July 9–12, 2019, Proceedings 8*, pages 266–276. Springer.

Whitney, J. P. and Wood, R. J. (2010). Aeromechanics of passive rotation in flapping flight. *Journal of Fluid Mechanics*, 660:197–220.

Willis, D., Israeli, E., Persson, P.-O., Drela, M., Peraire, J., Swartz, S., and Breuer, K. (2007). A computational framework for fluid structure interaction in biologically inspired flapping flight. In *25th AIAA Applied Aerodynamics Conference*, page 3803.

Winslow, J., Otsuka, H., Govindarajan, B., and Chopra, I. (2018). Basic understanding of airfoil characteristics at low reynolds numbers (104–105). *Journal of Aircraft*, 55:1050–1061.

Wootton, R. J. (1981). Support and deformability in insect wings. *Journal of Zoology*, 193:447–468.

Wootton, R. J. (1992). Functional morphology of insect wings. *Annu. Rev. Entomol*, 37:113–153.

Wu, X., Zhang, X., Tian, X., Li, X., and Lu, W. (2020). A review on fluid dynamics of flapping foils. *Ocean Engineering*, 195:106712.

Xiao, S., Hu, K., Huang, B., Deng, H., and Ding, X. (2021). A review of research on the mechanical design of hoverable flapping wing micro-air vehicles. *Journal of Bionic Engineering*, 18:1235–1254.

Yamada, T. and Yoshimura, S. (2008). Line search partitioned approach for fluid-structure interaction analysis of flapping wing. *Computer Modeling in Engineering and Sciences*, 24(1):51.

Yao, Y., Yeo, K. S., and Nguyen, T. T. (2019). *A numerical study on free hovering fruit-fly with flexible wings*, volume 34. Springer.

Yarger, A. M. and Fox, J. L. (2016). Dipteran Halteres: Perspectives on Function and Integration for a Unique Sensory Organ. *Integrative and Comparative Biology*, 56(5):865–876.

Yin, B. and Luo, H. (2010). Effect of wing inertia on hovering performance of flexible flapping wings. *Physics of Fluids*, 22(11):111902.

Young, J., Walker, S. M., Bomphrey, R. J., Taylor, G. K., and Thomas, A. L. R. (2009). Details of insect wing design and deformation enhance aerodynamic function and flight efficiency. *Science*, 325(5947):1549–1552.

Zhao, L., Huang, Q., Deng, X., and Sane, S. P. (2010). Aerodynamic effects of flexibility in flapping wings. *Journal of the Royal Society Interface*, 7:485–497.

Zhong, Q., Liu, G., Ren, Y., and Dong, H. (2017). On the passive pitching mechanism in turning flapping flights using a torsional spring model. In *47th AIAA Fluid Dynamics Conference*, page 3817.